SCUOLA DI DOTTORATO
UNIVERSITÀ DEGLI STUDI DI MILANO-BICOCCA

Department of

Materials Science

PhD program in **Materials Science and Nanotechnology**
Cycle XXV

AR-XRF Techniques for the Analysis of Cultural Heritage layered samples

Jacopo Orsilli

859911

Tutor: Prof Marco Martini

Co-tutor: Prof Anna Galli

Coordinator: Prof Marco Bernasconi

ACADEMIC YEAR 2021/2022

Jacopo Orsilli: *AR-XRF techniques for the analysis of Cultural Heritage Layered Samples*, © 2021/2022

Physics is like sex:
sure, it may give some practical results,
but that's not why we do it.

— Richard P. Feynman

To my family and friends.

ABSTRACT

In the last decades scientific analysis has been deeply employed in the world of cultural heritage, thus, archaeologists and art historians are no more the sole front line workers of this field. Scientists, and science, have joined the team, giving new inputs and tools for the study of historical and archaeological samples, allowing to explore new paths and receive new answers, collecting information otherwise inaccessible on human history and culture. New discoveries have been made on the trade networks, migrations and on the technologies employed; besides, science also gave precious inputs on conservation and restoring procedures, allowing to better preserve fragile and sensitive artifacts.

In my three years as a PhD student, I worked on the application of X-Ray Fluorescence (XRF) analysis to analyze ceramic and metal samples. XRF is a non-invasive technique that retrieves the elemental composition of a sample. In particular the aim of my PhD project is to obtain information on the layered structure of an unknown sample, distinguishing and characterizing the different layers. Indeed, artifacts usually concerning the field of Cultural Heritage present a layered structure; sometimes it is due to the presence of alteration layers, other times, instead, the objects are made of different layers from the principle, for example in the case of a glazed ceramic or of a painting. The possibility to get this information in a non-invasive way will give the possibility to analyze objects that are nowadays unattainable, because they cannot be sampled.

My project has, thus, focused on the analysis of three kinds of samples employing angular dependent techniques (Angle Resolved - XRF, Grazing Emission - XRF, Grazing Incidence - XRF); indeed, the fluorescence signal of an analyte depends on its position inside the sample, on the sample composition and on the geometry of analysis. The chosen specimens allowed to verify the feasibility of this analytical method in an increasing complexity: a gilded laboratory-made sample, a ceramic Majolica sherd, and an Italian renaissance lustered fragment.

The first two samples have been analyzed through Angle Resolved - XRF, where the measure is performed while tilting the sample, one spectrum is collected for each tilting angle. In the case of the gilded sample the measured profiles have been compared directly with the calculated profiles employing the Fundamental Parameters methods. For the ceramic Majolica sample, instead, we studied the ratio of the profiles, as the sample surface is not flat. In the study of the metallic samples, made of gilded copper plate, we could infer the thickness of the top-layer. While in the case of the Majolica sample, we studied

the different decorations, evaluating the limits of the technique, in particular in the case that the top-layer composition is similar to the underling layer, or in the case of a long-range diffusion. Instead, in the case of two well-separate layers we could retrieve information on both the composition and the thickness of the layer.

Finally, the study of the lustered ceramic has been carried out at the XRF beamline of the Elettra Synchrotron of Trieste, employing grazing techniques. In this case we could only highlight and distinguish the presence of the silver nanoparticles in the luster nanolayer, which is the peculiar feature of this kind of artifacts. However, there are still many questions left, especially concerning the data analysis and the alignment of the sample, which requires more investigations.

RIASSUNTO

L'analisi scientifica è da un po' di tempo entrata nel mondo dei beni culturali, non sono più solo gli archeologi e gli storici dell'arte a occuparsi dello studio dei reperti archeologici e storici, ma anche gli scienziati sono entrati a gamba tesa portando le loro conoscenze al servizio di questa vasta gamma di materiali. Lo studio di reperti botanici e zoologici, le competenze chimiche e mineralogiche, lo studio di fenomeni fisici, ha permesso di porre e rispondere a nuove domande, colmando così lacune sulla storia dell'umanità. Reti commerciali, migrazioni, tecniche produttive, molte sono state le scoperte avvenute grazie anche all'intervento scientifico, oltre a fornire strumenti utili al restauro e alla conservazione dei reperti.

Nei miei tre anni di dottorato mi sono occupato dell'applicazione dell'analisi in Fluorescenza a Raggi X (XRF) per analizzare campioni metallici e ceramici. Questa tecnica ha il vantaggio di poter essere applicata in maniera non invasiva e non distruttiva su un reperto per ottenere informazioni sulla sua composizione elementare. In particolare, il nostro obiettivo è quello di ottenere informazioni sui diversi strati che compongono un campione. Spesso, infatti, i manufatti presentano una struttura stratificata causata dal passaggio degli anni o dalla natura stessa dell'oggetto, che presenza una serie di decorazioni superficiali. L'impiego di tecniche non invasive permetterebbe quindi di ottenere informazioni più dettagliate anche su campioni al momento inaccessibili, in quanto troppo fragili o troppo preziosi.

Lo studio si è quindi avvalso di tecniche a scansione angolare, per cui il segnale di fluorescenza caratteristica dipende sia dalla posizione dell'analita all'interno del campione, sia dalla struttura e composizione dello stesso, sia dalla geometria di analisi. Per valutare l'applicabilità delle tecniche sono stati analizzati tre casi diversi: campioni metallici preparati ad hoc in laboratorio, un campione ceramico, e un campione di lustro.

Per i primi due campioni è stata applicata l'XRF a Risoluzione Angolare (AR-XRF) per cui il campione è stato ruotato con uno step angolare inferiore a un grado, e misurato ad ogni step. Nel caso dei campioni metallici i profili misurati sono stati confrontati direttamente con i profili calcolati usando il metodo dei Parametri Fondamentali. Nel caso del campione ceramico invece, sono stati confrontati i rapporti dei profili, in quanto la geometria del campione era piuttosto complessa.

Nello studio sui campioni metallici, composti da una doratura depositata su una lamina di rame, è stato possibile calcolare lo spessore dello strato superficiale. Nel caso del campione di Majolica sono invece state studiate le varie decorazioni, valutando così anche diversi limiti della tecnica, in particolar modo nel caso in cui la composizione della decorazione sia simile alla composizione dello strato sottostante, o nel caso in cui avvengano processi di diffusione a lunghe distanze. In casi in cui invece lo spessore della decorazione era limitato e ben separato dallo strato sottostante, è stato possibile ottenere informazioni sua sulla composizione della decorazione che sul suo spessore.

Infine, lo studio delle ceramiche lustrate è stato effettuato presso la linea XRF del Sincrotrone di Elettra, impiegando tecniche di analisi in radenza. In questo caso stato possibile solo evidenziare come il nanostrato di nano-particelle di argento, caratteristico di questa tipologia di campioni, sia effettivamente distinguibile applicando queste tecniche, in quanto il profilo di fluorescenza di tale elemento è molto diverso dagli altri. Rimangono comunque dei problemi, legati soprattutto all'analisi dati e all'allineamento che vanno ancora risolti, rendendo necessari ulteriori studi a riguardo.

PUBLICATIONS

[1] N. Ludwig, J. Orsilli, L. Bonizzoni, and M. Gargano. "UV-IR Image Enhancement for Mapping Restorations Applied on an Egyptian Coffin of the XXI Dynasty." In: *Archaeol Anthropol Sci* 11.12 (Dec. 2019), pp. 6841–6850. ISSN: 1866-9557, 1866-9565. DOI: 10.1007/s12520-019-00943-z.

[2] J. Melada, N. Ludwig, F. Micheletti, J. Orsilli, M. Gargano, and L. Bonizzoni. "Flash Thermography Mapping of Degradation Patterns in Archaeological Glass." In: *Proceedings* 27.1 (Sept. 16, 2019), p. 5. ISSN: 2504-3900. DOI: 10.3390/proceedings2019027005.

[3] J. Melada, N. Ludwig, F. Micheletti, J. Orsilli, M. Gargano, E. Grifoni, and L. Bonizzoni. "Visualization of Defects in Glass through Pulsed Thermography." In: *Appl. Opt.* 59.17 (June 10, 2020), E57. ISSN: 1559-128X, 2155-3165. DOI: 10.1364/AO.388469.

[4] F. Micheletti, J. Orsilli, J. Melada, M. Gargano, N. Ludwig, and L. Bonizzoni. "The Role of IRT in the Archaeometric Study of Ancient Glass through XRF and FORS." In: *Microchemical Journal* 153 (Mar. 2020), p. 104388. ISSN: 0026265X. DOI: 10.1016/j.microc.2019.104388.

[5] J. Orsilli, A. Galli, L. Bonizzoni, and M. Caccia. "More than XRF Mapping: STEAM (Statistically Tailored Elemental Angle Mapper) a Pioneering Analysis Protocol for Pigment Studies." In: *Appl. Sci. Switz.* 11.4 (2021), pp. 1–23. ISSN: 2076-3417. DOI: 10.3390/app11041446.

[6] J. Orsilli, A. Migliori, R. Padilla-Alvarez, M. Martini, and A. Galli. "AR-XRF Measurements and Data Treatment for the Evaluation of Gilding Samples of Cultural Heritage." In: *J. Anal. At. Spectrom.* 38 (2023), pp. 174–185. ISSN: 0267-9477, 1364-5544. DOI: 10.1039/D2JA00227B.

[7] G. Ruschioni, Micheletti, Francesca, L. Bonizzoni, J. Orsilli, and A. Galli. "FUXYA2020: A Low-Cost Homemade Portable EDXRF Spectrometer for Cultural Heritage Applications." In: *Appl. Sci. Switz.* 12.3 (2022). ISSN: 2076-3417. DOI: 10.3390/app12031006.

[8] M. Saleh, L. Bonizzoni, J. Orsilli, S. Samela, M. Gargano, S. Gallo, and A. Galli. "Application of Statistical Analyses for Lapis Lazuli Stone Provenance Determination by XRL and XRF." In: *Microchemical Journal* 154 (May 2020), p. 104655. ISSN: 0026265X. DOI: 10.1016/j.microc.2020.104655.

We shall not cease from exploration
And the end of all our exploring
Will be to arrive where we started
And know the place for the first time.
Through the unknown, remembered gate
When the last of earth left to discover
Is that which was the beginning;
At the source of the longest river
The voice of the hidden waterfall

— T.S. Eliot

ACKNOWLEDGMENTS

I've chosen that quote from T.S. Eliot as it perfectly fits the writing process of a PhD thesis: it's the moment when you look back to what you have accomplished in your three years of research, and you look at it with new eyes, and a new (maybe) wisdom. From the top of the mountain (because I know that you all have felt that way when you reached this moment) you stare at the valley, the clouds are gone and all the scary moments have been overcame, and there you realize that many people have taken part to your project, giving you their infinite and amazing support. Without you all anything of this wouldn't be possible.

First of all I'd like to thank my co-tutor, prof. Anna Galli, which guided and supported me in these three years of work, bringing me back on the right track when I got (and mostly felt) lost. Then prof. Letizia Bonizzoni, that five years ago asked me to do my thesis work with her, introducing me in the marvellous world of XRF, and that since then has been the person I talked when the frustration of science and research (that as my fellow PhD students know, is a necessary monster we have to deal with) felt overwhelming. I would then like to thank dr. Alessandro Migliori and dr. Roman Padilla Alvarez (all the people of the IAEA), that welcomed me at the Nuclear Science Instrumentation Laboratories of Seibersdorf for six months, and taught me more than I could ever ask for, they all made me feel like home during that period.

Finally I would like to thank dr. Giuliana Aquilanti, dr. Ilaria Carlomagno and dr. Simone Pollastro, from Elettra synchrotron, that allowed me to perform the measurements at the XRF beamline and supported me in the data acquisition. And I cannot forget Andreas Karydas, that is still supporting me in the analysis of the grazing data, thank you very much.

CONTENTS

ACRONYMS

AR-XRF Angle Resolved - XRF
BSE Backscattered Electron
BMS Beam Monitoring System
CCD Charge-coupled Device
CH Cultural Heritage
CF-XRF Confocal - XRF
FP Fundamental Parameters
GE-XRF Grazing Emission - XRF
GI-XRF Grazing Incidence - XRF
HOS Higher Order Suppressor
IAEA International Atomic Energy Agency
NSIL Nuclear Science and Instrumentation Laboratories
SDD Silicon Drift Detector
SEM Scanning Electron Microscope
RBS Rutherford Backscattering Spectrometry
ROI Region of Interest
SWF Standing Wave Field
TXRF Total reflection - XRF
UHV Ultra High Vacuum
XRF X-Ray Fluorescence
XRR X-Ray Reflectometry

1 INTRODUCTION

When talking about Cultural Heritage (CH) artifacts, we refer to a plethora of objects of different materials, ages and places; objects that represent the human evolution and history, the life stile, the culture, the beliefs of a certain place and time. These artefacts have a great value not only because they are made of precious materials, or because they are rare or unique, but because their sole existence is a reminiscence of the past, of our past.

In the last decades the study of CH materials has evolved, and it is no more only a responsibility of archaeologist and art historians, on the opposite, all the fields of science have penetrated this world providing new precious tools to analyze, restore and preserve these artifacts. From chemistry, to geology, biology, and climatology, and least (but not last) physics, they all participate now: the study of atoms and molecules, plants, bones, minerals or fibers has enriched the amount of stories that an object can tell: Where does it came from? How was it made? When was it made? Where was placed the source of the raw materials? Does it give information on the trading? The technology was invented there or imported? And how it was imported, through learning or through migrations? As new question has arose, we got new answers, and new pieces of the puzzle of human history has been put into the right place.

My three years work ad the department of Material Science focused on the application of X-Ray Fluorescence (XRF) for the study of Cultural Heritage materials, evaluating the feasibility to study the layer composition of sample in a non-invasive and non-destructive way. XRF, indeed is a common technique applied in the field of CH, as it allows a fast and low cost qualitative (and in some cases quantitative) evaluation of the sample elemental composition. Quantitative XRF analyzes, however, can be performed only in certain conditions, the most important is the homogeneity of the sample. Many samples in this field are indeed far from homogeneous, and they present not only lateral inhomogeneities, but also an in-depth inhomogeneity. The latter, can be exemplified by a layered structure, which is mainly caused by two reasons:

1. the layered structure is a characteristic desired by the manufacturer, e.g., in painting, decorated ceramics or coated metals;

2. the layers are caused by the object degradation with the passing of time, e.g., glass and ceramic patina, corroded metals.

In these cases, it must be kept in mind that the fluorescence intensity of each analyte depends on its position inside the sample and on the composition of the covering layers. That's why, using different geometries, it is often employed in Material Science to analyze the layered structure of industrial samples. If the same set-ups (of course with the required adjustments) can be applied also for the study of CH artifacts, we can obtain new information for artifacts at the moment inaccessible, may be because too fragile or because they cannot be sampled.

Of course there are, other, different techniques that allows a layer characterization of a sample, for example Rutherford Backscattering Spectrometry (RBS). Nevertheless, these analytical techniques require a particle accelerator, that is not available to many laboratories or scientists. Thus, an improvement of a low-cost technique, will ease the data collection, allowing the study of more specimens.

After a brief introduction on XRF and the angle dependants techniques: Angle Resolved - XRF (AR-XRF), Grazing Incidence - XRF (GI-XRF) and Grazing Emission - XRF (GE-XRF) (chapter 2), and after talking about the instrumentation employed (chapter 3), we will discuss about the study of different layered samples employing only angle dependant XRF techniques.

The study has been carried out starting from the most simple case: bi-layer metallic samples prepared in laboratory (chapter 4), where even if the structure is well-known, many problems often found when analyzing CH materials are reported (lateral inhomogeneity and a not flat surface). Then, we increased the number of parameters involved in the description of the sample, and we studied Majolica ceramic sherd, that shows different kinds of decorations (chapter 5). The study has been performed at the Nuclear Science and Instrumentation Laboratories (NSIL) (Seibersdorf, Austria) of the International Atomic Energy Agency (IAEA), where I spent six month of my PhD program.

Finally, at the XRF line of the Elettra synchrotron, we analyzed a Renaissance luster ceramic sherd, coming from the center of Italy (chapter 6). In this case we applied grazing techniques for the analysis, but as the data analysis softwares for the study of the grazing profiles are still not adequate for the characterization of such complex samples, we here just describe the qualitative results of that measurement campaign; with the aim to improve in the future the data analysis tools.

2 ANGLE DEPENDANT - XRF

Angle Dependant - XRF, here, refers to the X-Ray Fluorescence (XRF) related techniques that employ a variation in the angles of irradiation or detection to retrieve information of the in-depth structure (i.e., density and composition) of an inhomogeneous sample. To analyze the in-depth inhomogeneity of a sample different approaches can be chosen. The most straightforward would be the sampling and the creation of a cross-section of the artifact, this would expose all the layers, allowing the analysis of each of them. The samples can be analyzed through micro-destructive or invasive techniques, so that a complete compositional, mineralogical and structural description of each layer can be given. The drawback of this method would be the sampling itself, due to the high value and rarity of the artifacts we usually deal with.

Thus, a multi-analytical approach is mandatory, different non-invasive techniques show a different penetration depth, allowing to collect multiple and complementary information. Nevertheless, this approach requires the availability of different instruments, and a lot of time to collect and analyze the data; moreover, the layers are not directly analyzed, but their composition is obtained thanks to inferences on the data.

Some XRF related techniques have already been proved to be useful for the analysis of Cultural Heritage samples, like the use the x-ray characteristic lines ratio [12, 17, 31, 69, 72], coupled with Monte Carlo simulations [11, 13, 26, 53, 68]; or the use of capillary lenses to select a small sample volumes in Confocal - XRF (CF-XRF) [2, 29, 30, 36, 41, 52, 54, 70, 71, 75, 78, 80, 83].

The techniques here considered are Angle Resolved - XRF (AR-XRF), Grazing Incidence - XRF (GI-XRF) and Grazing Emission - XRF (GE-XRF); the first one is employed for the analysis of nanometres-micrometres thick layers, while the other two are usually employed for the analysis of nanometres thick layers.

The principal aim of the angle dependant-XRF techniques is to characterize the layers composing a sample and to quantify the analytes concentration in each layer. After introducing the main theory of XRF, we will relate the concentration of an analyte with its fluorescence intensity through the Sherman's equation, that, being based on the fundamental physics that describes the radiation-matter interactions, can be written for different cases, like for the analysis of homogeneous, inhomogeneous and layered samples. As different layers compose the sample, their attenuation and its relation with the geometry of analysis

can be described using the Lambert-Beer's law, through which we can calculate the probed, and analyzed volume related with the different fundamental parameters.

Finally, all the corrections related to refraction, reflection and interference phenomena, will be considered. These phenomena highly affects the fluorescence intensity when the angles of analysis are in the order of the critical angles of total-refraction, i.e. when GI-XRF and GE-XRF are preformed.

2.1 X-RAY FLUORESCENCE (XRF)

XRF is a well-known analytical technique that gives information on the elemental composition of a sample. It is very useful for the investigation of CH artifacts as it allows a non-invasive analysis of a specimen, also giving the chance to perform in-situ measurements. These two features are helpful when we have to analyze samples that are unique, valuable, or rare (from which any sampling can be performed); or if the artifact is so fragile or big that cannot be moved from the place in which is stored (like a museum or an archaeological site). Commonly XRF can detect elements from sodium to uranium with a fast and easy-to-perform acquisition, moreover, if the sample satisfies certain requirements: (I) homogeneous composition, (II) smooth surface for the employed radiation, (III) the source beam is parallel; it is possible to perform quantitative analysis, obtaining the concentration of the elements composing the specimen.

2.1.1 Photons and matter: X-Rays interactions with atoms

The physics behind XRF is based on the interaction of x-rays with the matter, above all two phenomena are particularly important: photoelectric absorption and scattering. The photoelectric absorption can take place if the interacting photon has an energy higher than the binding energy of a core electron of the atom. In this case the photon absorption causes the photoionization of the atom, with the emission of a photoelectron and the formation of a core-hole of energy E_0. The ionization is followed by a relaxation process, in which an electron from an upper shell with energy E_i fills the core-hole, releasing an energy $\Delta E = E_i - E_0$, characteristic of the electronic transition. This energy excess can be emitted in a radiative process with the emission of a photon, or it can be absorbed again causing the emission of a second electron (Auger electron) in a non-radiative process, Fig 2.1. The radiative and non-radiative processes are competitive, and their probability for each of them to take place is called respectively fluorescence and Auger yield, Fig. 2.2. Finally, the scattering processes can be elastic, if there is no energy transfer, or anelastic, is there is

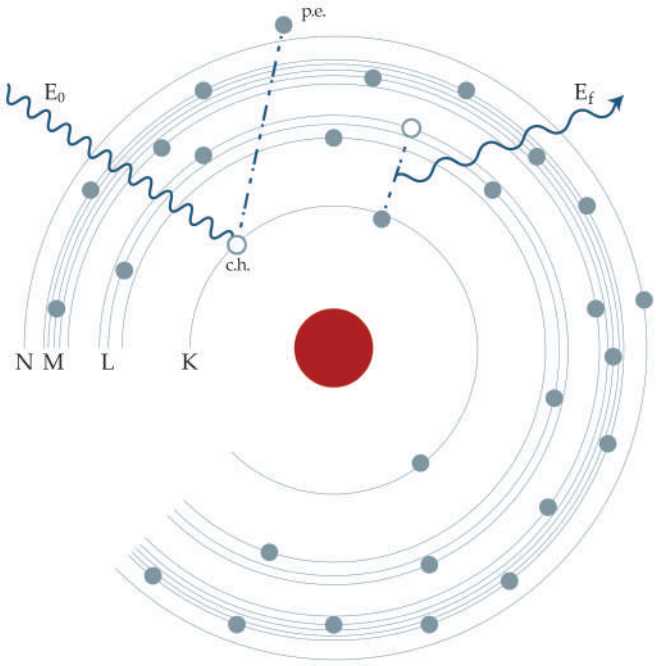

Figure 2.1: Scheme of the fluorescence process on a copper atom: the photon with energy E_0 hit a core electron on the shell K which is emitted as a photo-electron (p.e), leaving a core-hole (c.h.); an electron from the shell L_3 fill the vacancy 'falling' in the K shell. The energy difference is emitted as a photon, with characteristic energy E_f.

energy transfer; these two phenomena are also known are Rayleigh and Compton scattering.

XRF spectrometers detects both fluorescence and scattered photons, the first are the most important as they are characteristic of the atomic species composing the sample, while the scattered photons contain information of the mean matrix atomic number [9, 10, 37]. The probability to have scattering or photoelectric absorption is called cross-section, and it depends on the energy of the photon and on the atomic number of the atom involved [14, 38].

The probability of having any kind interaction with a photon and an absorber that contains one atom for cm^2 of area is then:

$$\sigma_T(E, Z) = \tau(E, Z) + \sigma_C(E, Z) + \sigma_R(E, Z) \tag{2.1}$$

where σ_T, measured in cm^2/atom, is the total atomic cross-section, τ is the atomic photoelectric absorption cross-section, σ_C is the atomic anelastic (Compton) scattering total cross-section and σ_R is the atomic elastic (Rayleigh) scattering total cross-section (Fig. 2.3).

From this probabilities we can deduce two important values that are: the mass attenuation coefficient, μ, which represents the interaction

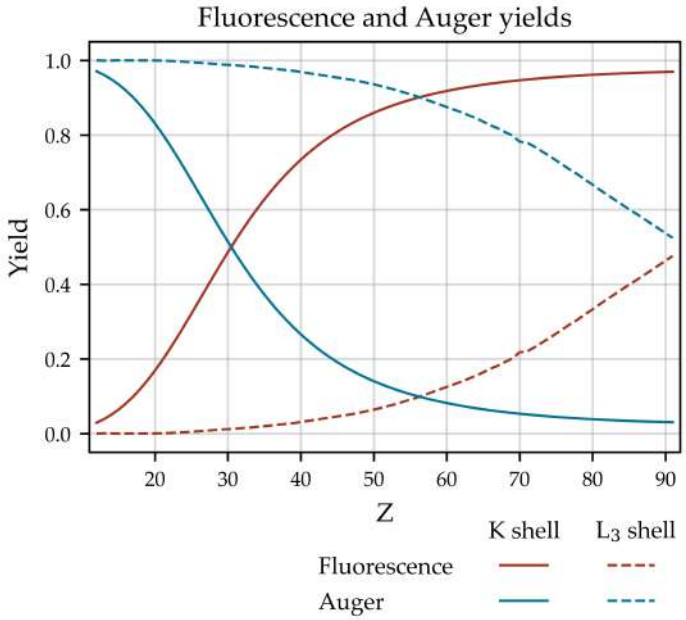

Figure 2.2: Fluorescence and auger yields for K and L_3 shells, as a function of the atomic number Z

probability for unit of mass, and the linear attenuation coefficient, μ^*, which represents the interaction probability for unit of length:

$$\mu \left[\frac{cm^2}{g}\right] = \sigma_T \left[\frac{cm^2}{atoms}\right] \frac{N}{A} \left[\frac{atoms}{g}\right] \tag{2.2}$$

$$\mu^* \left[\frac{1}{cm}\right] = \mu \left[\frac{cm^2}{g}\right] \rho \left[\frac{g}{cm^3}\right] \tag{2.3}$$

in which N is the Avogadro number, A is the atomic mass and ρ is the density. For a mixture of known composition, we can calculate the attenuation coefficient as:

$$\mu_s = \sum_{q=1}^{n} w_q \mu_q \qquad \text{where: } \sum_{q=1}^{n} w_i = 1 \tag{2.4}$$

where w_q is the concentration of the atomic species q.

2.1.2 The Sherman's equation

As we said before, XRF can be used to perform qualitative and quantitative analysis, and the Sherman's equation, Eq. 2.5 (here shown considering a polychromatic radiation and a sample of medium thickness),

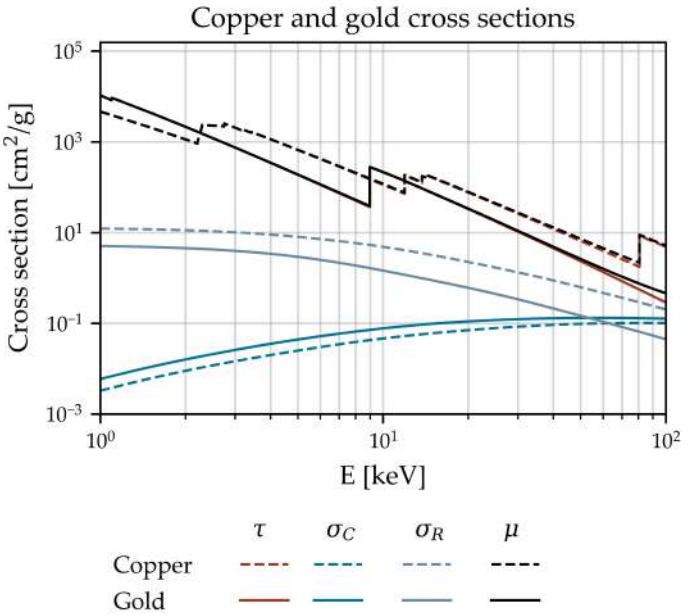

Figure 2.3: Photoelectric, Compton, Rayleigh and Total attenuation cross-sections for copper and gold in the energy range 1 keV to 100 keV

relates the fluorescence intensity of the analyte to the experimental conditions [3, 62, 67]:

$$I_{q,l} = G_q P_{q,l} w_q \int_{S_q}^{E_M} \frac{I_0(E)\tau_q(E)}{M_s(E,E_q)} \left(1 - \exp\left[-\rho h M_s(E,E_q)\right]\right) s(q) dE \quad (2.5)$$

Here, w_q is the concentration of the analyte, S_q is the energy of the photoelectric absorption edge for the given group of lines of the analyte, E_M is the maximum energy of the source, $I_0(E)$ is the source intensity distribution, $\tau_q(E)$ is the photoelectric absorption cross-section, ρ is the sample density, h is the sample thickness and $s(q)$ is the factor of second enhancement. $P_{(q,l)}$ is the probability of X-ray production for a given fluorescence line of the analyte:

$$P_{q,l} = \frac{j_S - 1}{j_S} \omega_{q,S} f_{q,l} \quad (2.6)$$

is proportional to the jump factor j of a shell S, the fluorescence yield ω, and the radiative rate f of the line. The jump factor represents the probability of the shell to be excited respect to the others, the fluorescence yield represents the photo-emission probability (instead of an Auger electron emission) and the radiative-rate describes the emission probability of a particular fluorescence line.

G is the geometrical factor:

$$G_q = \frac{\Delta\Omega}{4\pi} \frac{\eta(E_q)}{\sin\phi} \quad (2.7)$$

with $\Delta\Omega$ solid angle of the detector, ϕ angle of excitation and η detector efficiency.

$M_s(E, E_q)$ is the total effective attenuation of the sample at the source and fluorescence energy:

$$M_s(E, E_q) = \frac{\mu_s(E)}{\sin\phi} + \frac{\mu_s(E_q)}{\sin\theta} \tag{2.8}$$

where θ angle of detection. The sine functions at the denominator in Eq. 2.8 accounts for the path-length of the source/fluorescence radiation inside the sample.

On many occasions, especially in the Cultural Heritage field, we deal with samples with heterogeneous distribution of the elements within the effectively probed volume; they can be layered or have a variable concentration of some elements. In that case, a more general equation describes the fluorescence intensity [38, 67]:

$$I_q = G_q P_q \int_{S_q}^{E_M} \int_0^h I_0(E)\tau_q(E)\rho(z)w_q(z) \exp\left[-\rho(z)zM_s(E, E_q)\right] s(q, z)dzdE \tag{2.9}$$

in this case z is the analyzed depth; $\rho(z)$ and $w_q(z)$ are respectively the sample density and the element concentration at the depth z. If the sample is made of N different homogeneous layers of thickness h_i $(i = 1, \ldots, N)$, and if the element of interest is present only in the m^{th} layer, from Eq. 2.9 we have that:

$$I_{m,q} = G_q P_q w_{m,q} \int_{S_q}^{E_M} I_0(E)\tau_q(E) \frac{(1 - \exp\left[-\rho_m h_m M_m(E, E_q)\right])}{M_m(E, E_q)} \exp\left[-\sum_{j=1}^{m-1} \rho_j h_j M_j(E, E_q)\right] dE \tag{2.10}$$

for simplicity, we have assumed here that no secondary enhancement occurs, as it highly increases the complexity of the calculations. If the same element is present in k layers, we simply get:

$$I_q = \sum_{m=1}^{k} I_{m,q} \tag{2.11}$$

When we perform XRF analysis we would like to use the Sherman's equation to solve the inverse problem; in other words, we want to calculate the sample composition from the intensity measured with our spectrometer. From equations 2.9 and 2.10 we can observe that the information collected from XRF come from the whole volume analyzed and that is not possible to discriminate the fluorescence signal coming from different layers of the samples.

Indeed, if we imagine a sample composed of two layers, for example a bronze statue covered of a thin patina layer, we collect the copper signal emitted both from the patina and the bulk alloy, and we cannot infer the copper concentration in the two layers. Thus, if the sample is not homogeneous, even if all the geometrical and instrumental conditions are known (e.g., the source distribution, the angle of analysis, the detector response function and efficiency...) the calculation of the analyte concentration is an ill-posed problem. Indeed, to calculate the copper concentration in the bulk we should also consider the presence and composition of patina layer. That's why XRF is usually referred as a bulk technique.

To select the layer of analysis we should find a way to select the volume of interaction of X-rays, for example CF-XRF, in which two lenses are placed in front of the source and the detector to select a small volume of the sample to analyze.

2.2 ANGLE RESOLVED XRF (AR-XRF)

Different parameters of the Sherman's equation affects the volume of the analysis: the total effective attenuation coefficient, Eq. 2.8, and the geometrical factor, Eq. 2.7, are weighted for the sines of the angle of incidence of the source radiation, and the angle of detection of the fluorescence radiation.

These two angles indeed highly influence the volume probed by the source and the fluorescence radiation, as described by the Lambert-Beer's equation.

2.2.1 Geometry of analysis and probed volume: the Lambert-Beer equation

When we consider the interaction of X-rays with matter, we must take into account the total attenuation coefficient, or the cross-sections of the single phenomena. As explained before, the probability of interaction can be calculated in function of the mass of interaction, Eq. 2.2, or in function of the path-length crossed by the photons, Eq. 2.3. The higher is the mass of interaction or the length crossed by the photons, the higher is the probability of interaction, thus the higher is the attenuation.

More precisely the photon attenuation is described by the Lambert-Beer's law, for which the attenuation process decreases exponentially in function on the linear attenuation coefficient and on the path-length crossed by the electromagnetic radiation inside the sample:

$$I = I_0 \exp\left[-\mu_s \rho x\right] \tag{2.12}$$

here, I_0 is the electromagnetic beam intensity before the interaction, I is the beam intensity after the interaction and x is the path-length crossed by the radiation.

If X-rays impinge on a sample of thickness t with an angle α, we can rewrite Eq. 2.12 as:

$$I = I_0 \exp\left[-\mu_s \rho_s \frac{t}{\sin\alpha}\right] \tag{2.13}$$

The attenuation of x-rays for a fixed specimen then depends on its composition, thickness and on the angle of incidence (or detection, if the considered x-rays are those emitted from a certain infinitesimal volume of the sample). Sometimes we are interested in the inverse problem: calculating the path-length that attenuates our beam of a certain factor, giving an idea of the volume investigated by an XRF measurement. We can calculate this value as:

$$t = \frac{\ln R}{\mu_s \rho_s} \sin\alpha \tag{2.14}$$

where $R = I_0/I$.

More precisely, we call penetration depth, Λ_p, the depth from which the source radiation is damped by a factor $1/e \approx 36\%$, and escape depth, Λ_e the depth from which the fluorescence radiation is damped by the same factor:

$$\Lambda_{[p/e]} = \frac{\sin\alpha}{\mu_s(E_{[0/q]})\rho_s} \tag{2.15}$$

where $\mu_s(E_{[0/q]}$ is either the source energy or the fluorescence energy, and α is either the angle of irradiation or detection. Table 2.1 shows different penetration and escape depths for different source energies/elements in different matrices.

The volume investigated thus depends on the energies and on the geometry of measurements, and the depth from which a fluorescence signal of the element q, Λ_q, is collected is the minimum value between the penetration and the escape depth:

$$\max(\Lambda_q(\phi,\theta)) = \min(\Lambda_p(E_0,\phi),(\Lambda_e(E_q,\theta)) \tag{2.16}$$

2.2.2 Working principle of AR-XRF

In AR-XRF we collect different XRF spectra changing the angle of incidence or detection (or both, tilting the specimen); hence, each spectrum represents the sample fluorescence emission in a different geometry. To collect AR-XRF profiles it is possible to use any kind of source, like an x-ray tube or synchrotron radiation; at the same time the fluorescence signal can be collected with any kind of detector. The only requirement is that the angular divergence of the source, and the angle

Table 2.1: Escape and penetration depths for different elements and fluorescence lines in different matrix, for a irradiation/detection angle of 90°. The source radiation is the Mo K_α line, $E_0 = 17.45\,keV$

Matrix	Density $[g\,cm^{-3}]$	Λ_p [µm]	Line	E_q [keV]	Λ_e [µm]
PMMA	1.19	10968.22			
SiO_2	2.32	1147.57	Si K_α	1.74	6.03
Bronze[1]	8.85	22.18	Cu K_α	8.04	14.12
			Sn L_α	3.44	2.00
			Sn K_α	25.19	60.49
			Pb L_α	10.54	6.31
			Pb M_α	2.35	0.83
Lemon gold[2]	15.96	6.94	Ag K_α	22.10	12.78
			Ag L_α	2.98	0.37
			Au L_α	9.70	4.90
			Au M_α	2.12	0.60

[1] Considered here with a composition of Cu 85 %, Sn 10 %, Pb 5 %;
[2] Alloy made of Au 75 %, Ag 20 %

of acceptance of the detector are low enough to ensure that the signal collected comes only from a selected volume of the sample at a given angle.

Indeed, from the Lambert-Beer law (Eq. 2.14) the depth investigated is directly proportional to the sine of the angles of incidence/detection: for small angles of irradiation the source beam crosses a thin volume before being attenuated, thus most of the photons are absorbed or scattered only from the sample surface; as the angle of irradiation increases the depth investigated by the source radiation increases, and deeper volumes are excited. In the same way, for low angles of detection, the fluorescence radiation crosses a long path before reaching the detector, thus signals coming from deep inside the sample are attenuated by the covering layers, and only the signal coming from the surface reaches the detector. In general, then, for lower angles of irradiation the excitation of the sample surface is enhanced, and for lower angles of detection the attenuation of the bulk signal by the sample surface is increased.

Through the fitting of the spectra we obtain the fluorescence profiles of the analytes, i.e., the plots of the fluorescence intensity versus the angle of detection (or irradiation, or tilting); that can be compared with profiles calculated using the Sherman's equations to find and adjust the parameters concerning the sample structure.

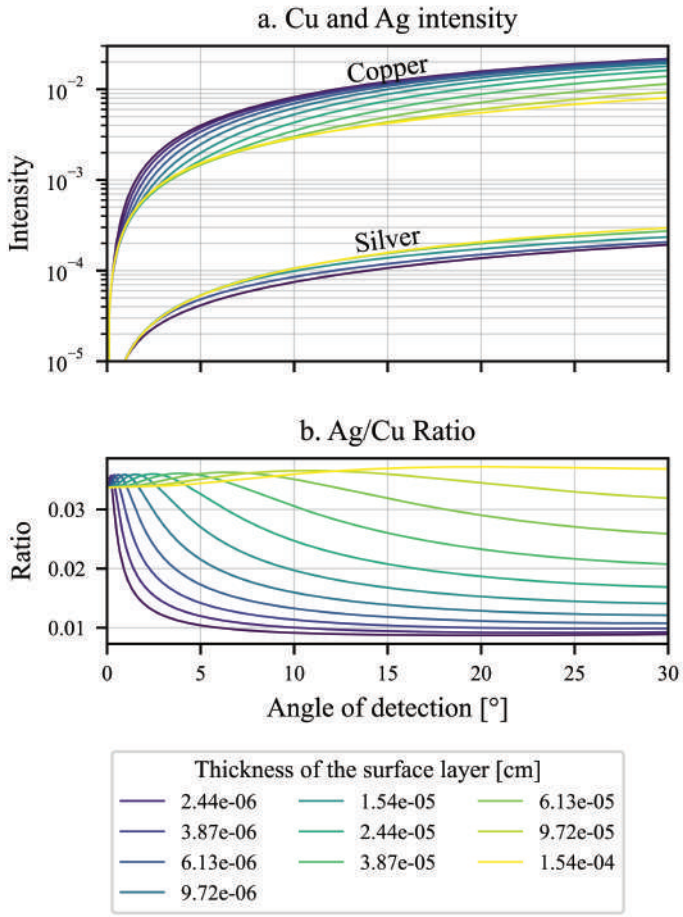

Figure 2.4: a. Silver and copper intensities calculated for a coin sample with a bulk composition of 60 % silver and a surface layer of 80 % silver, the plots represent different profiles calculated for different thicknesses of the surface layer. b. Ratio of the silver and copper intensity

An example of the variation of the fluorescence profiles can be observed, for example, if we consider a silver coin with composition of 60 % silver and 40 % copper, covered with a surface layer composed by 80 % of silver and 20 % of copper. By changing the thickness of the surface layer, we get different intensity profiles for the two elements (Fig 2.4a), that can also be evaluated by plotting the Ag/Cu ratio (Fig. 2.4b).

2.3 GRAZING INCIDENCE XRF (GI-XRF)

GI-XRF is born as a variant of Total reflection - XRF (TXRF), as they both employ the same instrumentation and geometry; the difference between the two techniques is that in TXRF no angular scanning is performed. Instead, in GI-XRF the angle of irradiation is changed,

scanning the sample at grazing angles, i.e., at angles around the critical angle of total reflection. In this angular range reflection and refraction, related to the material refractive index, and interference, due to the superimposition of direct and reflected radiation, concur with attenuation to influence the fluorescence signal of the sample.

2.3.1 Refractive index, refraction, and reflection

Before talking about the refractive index, it is important to stress that when an electromagnetic radiation impinges on the sample, it crosses at least one interface: the one between the sample surface and the atmosphere (for example vacuum or air). When an electromagnetic field, $\vec{\mathcal{E}}(\vec{r},t)$ interacts with atoms, an oscillatory motion is induced to the bound electrons, and it can be described in classical mechanics as:

$$\vec{x}(\vec{r},t) = \frac{e}{m}\frac{h}{(E^2 - E_s^2) + i\gamma E}\vec{\mathcal{E}}(\vec{r},t) \tag{2.17}$$

where, $\vec{x}(\vec{r},t)$ is the electron position, e and m are the electron charge and mass, h is the Plank constant, E_s is the electron's natural energy of oscillation and γ is a dissipative factor. The electron oscillation induces then a current density inside the material, changing the wave propagation, i.e., the wave phase speed v_ϕ. The wave phase speed variation inside the material respect to the vacuum, is called refraction index [4, 34]:

$$n(E) = \frac{c}{v_\phi} = 1 - \frac{e^2 n_a h}{2\varepsilon_0 m}\sum_s \frac{g_s}{(E^2 - E_s^2) + i\gamma E} \tag{2.18}$$

where c is the speed in vacuum, n_a is the atomic density, ε_0 is the permittivity of free space. The sum is calculated over all the electrons s of the atom, and g_s represents the oscillation strength of each bound electron.

For visible light the phase speed in any medium is lower than the speed in vacuum, and the refractive index is always higher than one, for x-rays, instead, the real part is lower than one, Fig. 2.5; this variation changes the behaviour of x-rays when crossing an interface.

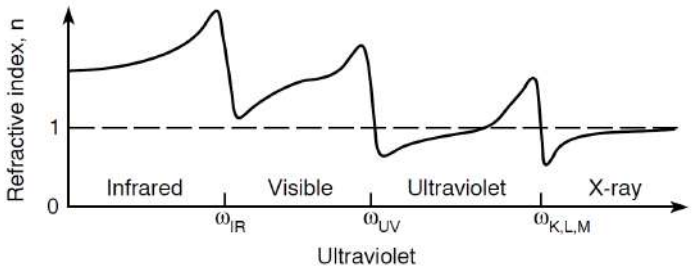

Figure 2.5: Refractive index for different electromagnetic radiations, from [4]

Equation 2.18 can be rewritten using the complex scattering factor $f^0(E) = f_1^0(E) - if_2^0(E)$:

$$f^0(E) = \sum_s \frac{g_s}{(E^2 - E_s^2) + i\gamma E} \tag{2.19}$$

obtaining:

$$n(E) = 1 - \frac{e^2 n_a h}{2\varepsilon_0 m} \left[f_1^0(E) - i f_2^0(E)\right] \tag{2.20}$$

from which we can separate the real and complex part of the index, calling δ the decrement from unity and β the imaginary module:

$$\delta = \frac{e^2 n_a h}{2\varepsilon_0 m} f_1^0(E) \tag{2.21}$$

$$\beta = \frac{e^2 n_a h}{2\varepsilon_0 m} f_2^0(E) \tag{2.22}$$

obtaining the common representation of the complex refractive index:

$$n(E) = 1 - \delta + i\beta \tag{2.23}$$

The value of β represent the attenuation due to absorption, and is strictly related to the attenuation coefficient as, at the atomic level, both depend on $f_2^0(E)$, indeed we can rewrite the attenuation coefficient in function of β as:

$$\mu = \frac{4\pi E}{\rho h c} \beta \tag{2.24}$$

The value of the decrement generally has the order of magnitude of 10^{-6}, while β has an order of magnitude of 10^{-8}; in table 2.2 are reported the values of the decrement and of the β term for different materials, and in Fig. 2.6 you can see the behaviour of the refractive index for copper and silicon in function of the photon energy.

At the interface between vacuum and the sample three waves propagates: the incident wave, the refracted wave and the reflected wave; and to satisfy Maxwell's equations they must satisfy the two conditions of continuity of the electromagnetic field and the inducted fields. The two continuity conditions give rise to the two equations of reflection and refraction (Snell's law), if we call φ, φ_1, φ_2 the glancing angles of incidence, reflection and refraction, and if n and n_2 are the refractive indices of the two media, see figure 2.7, the two laws are:

$$\varphi = \varphi_1 \tag{2.25}$$

$$n \cos\varphi = n_2 \cos\varphi_2 \tag{2.26}$$

From equation 2.26 we can calculate the new angle of propagation of the electromagnetic radiation inside the medium as:

$$\cos\varphi_2 = \frac{n}{n_2} \cos\varphi \tag{2.27}$$

Table 2.2: Density, decrement and β term for different materials at the Mo K_α energy.

Material	ρ [g cm^{-3}]	$\delta(10^{-6})$	$\beta(10^{-8})$
Plexiglas	1.16	0.9	0.055
Boron nitride	2.29	1.5	0.090
Quartz glass	2.20	1.5	0.46
Aluminum	2.70	1.8	0.79
Silicon	2.33	1.6	0.84
Cobalt	8.92	5.6	19.8
Nickel	8.91	5.8	21.9
Copper	8.94	5.6	24.1
Germanium	5.32	3.2	18.7
Tantalum	16.6	9.1	87.5
Platinum	21.45	11.7	138.2
Gold	19.3	10.5	129.5

If the radiation moves from a medium with a lower refraction index, toward a medium with a higher refraction index, it is bent toward the perpendicular of the sample, this happens for example when crossing the interface of the sample and the vacuum; on the contrary, when the x-ray beam moves from a more optically dense medium (higher refraction index) toward a less optically dense medium, it is bent toward the surface.

As the angle of refraction is, in the latter case, lower than the angle of incidence, there is a lower limit for this phenomenon, which is called critical angle, φ_c. If we suppose an electromagnetic radiation crossing the interface between vacuum ($n = 1$) and the sample, in the limit case the angle of refraction propagates along the sample surface, thus $\varphi_2 = 0$; and Eq. 2.27 becomes:

$$\cos\varphi = n_2 = 1 - \delta_2 + i\beta_2 \tag{2.28}$$

remembering that we can neglect β as it is two orders of magnitude lower than δ, and applying the Taylor expansion for the cosine function, the relation becomes:

$$\frac{\varphi^2}{2} \approx \delta_2 \tag{2.29}$$

The lower angle for which is possible to have refraction, is then:

$$\varphi_c \approx \sqrt{2\delta_2} \tag{2.30}$$

For Mo K_α impinging on a silicon reflector, for example, the critical angle is approximately 1.7 mrad.

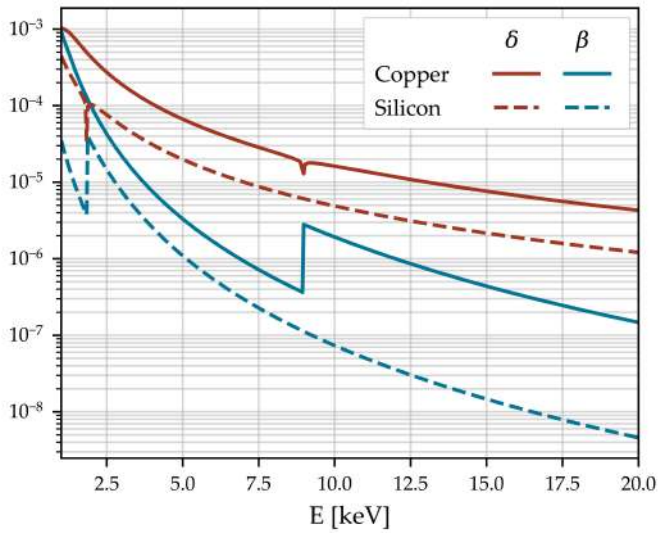

Figure 2.6: Values of δ and β for copper and silicon in the energy range 1 keV to 10 keV

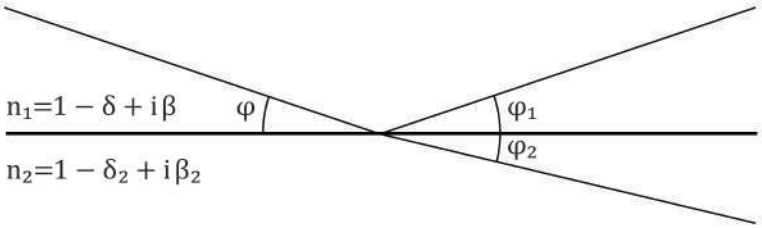

Figure 2.7: Angles formed at the interface between two media due to reflection and refraction phenomena. φ is the angle of incidence radiation, φ_1 is the angle of reflected radiation, and φ_2 is the angle of the refracted radiation

For angles lower than the critical angle, the impinging beam is then totally reflected inside the first medium. As the medium in which the reflection occurs is usually air, or vacuum, for x-rays we have the so called total external reflection; instead for visible light, for which the reflected beam is inside the sample, we have total internal reflection.

2.3.2 Geometry of analysis and probed volume: the Fresnel's laws

When an interface is crossed, part of the incident radiation is refracted and part is reflected, thus not only the direction of the beam is changed, but also its intensity is split. The proprieties that describe the amount

of reflected and transmitted radiation are called reflectivity, R, and transmissivity, T, and are described by the Fresnel's laws:

$$R = \left| \frac{\varphi - \varphi_2}{\varphi + \varphi_2} \right|^2 \tag{2.31}$$

$$T = \left| \frac{2\varphi}{\varphi + \varphi_2} \right|^2 \tag{2.32}$$

remembering that φ_2 is a complex number, calculated from Eq. 2.27, and that it can be approximated, considering the external medium as vacuum, as:

$$\varphi_2^2 \approx \varphi^2 - 2\delta_2 + 2i\beta_2 \approx \varphi^2 - \varphi_c^2 + 2i\beta_2 \tag{2.33}$$

The intensity of the penetrating (transmitted) beam is damped following the Fresnel's laws, propagating as an evanescent wave only on the surface (first nanometres) of the sample.

We can correct then the penetration depth of the incident beam considering the reflectivity, obtaining [3]:

$$\Lambda_F = \frac{hc}{4\pi E \, \mathrm{Im}\left(\sqrt{\varphi^2 - \varphi_c^2 + 2i\beta_2}\right)} \tag{2.34}$$

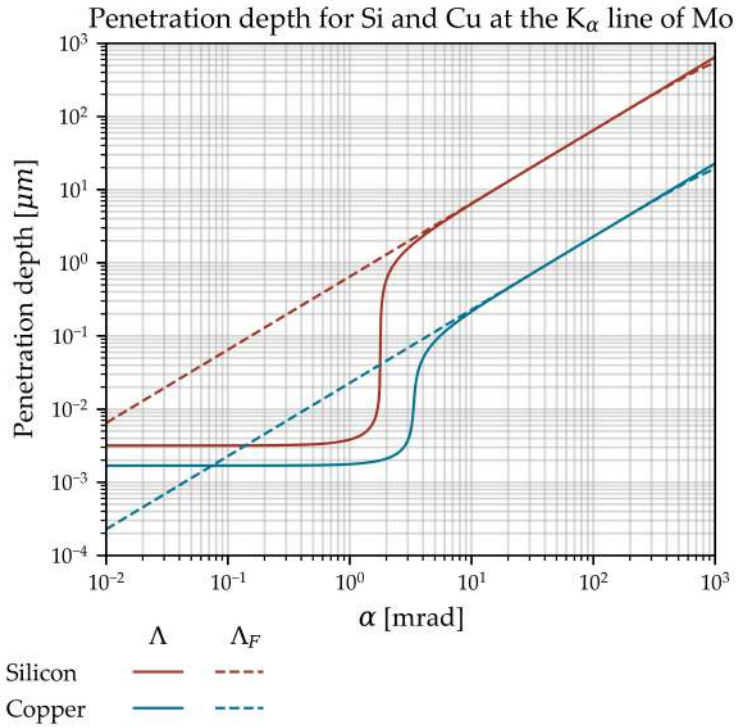

Figure 2.8: Penetration depth in Silicon and Copper, for an x-ray radiation of 17.45 keV, calculated using the attenuation (Lambert-Beer law, Eq. 2.15) and considering the reflectivity, Eq. 2.34.

It can be seen in figure 2.8 that the penetration depth calculated using both the Lambert-Beer law, Eq. 2.15, and the reflectivity, Eq. 2.34, have the same values for shallow angles that are greater than the critical angle. It must be kept in mind however, that the reflectivity approximation makes sense only for small angular values, and only if the surface is smooth; for a rough surface, in the region below the critical angle the penetration depth increases, reaching the same value calculated using the Lambert-Beer equation.

2.3.3 Interference: the Standing Wave Field (SWF)

As we have seen, if the electromagnetic radiation impinges on a polished surface (reflector) with a sufficient shallow incident angles $\varphi \leqslant \varphi_c$, a high amount of the x-ray intensity is reflected with an angle $\varphi_1 = \varphi$. As the critical angle is energy dependent, we suppose here that the direct radiation is monochromatic, in this way the source radiation is reflected toward a singular angle and is not dispersed along different directions for each energy, or transmitted deep inside the reflector, and it propagates only on the surface as an evanescent wave.

As the two beams superimpose, an interference among them arises; this interference wave field shows maxima and minima depending on the phase difference between the two fields. If the two phases have a difference of an odd multiple of π the intensities are subtracted to a minimum (node), if the difference is equal to an even multiple of π the intensities are summed up to a maximum (anti-node). Nodes and anti-nodes can be extended along the interface plane forming nodal and anti-nodal planes. As the wave field due to the interference does not propagates, its intensity oscillates around stationary minima and maxima, for this reason the interference field is called Standing Wave Field, and its intensity can be mathematically calculated through an iterative approach [51].

As the interference pattern depends on the two beams (which have the same frequency) superimposition, the distance d_z of the nodal and anti-nodal planes depends on the beam frequency (so on its energy) and on the impinging angles:

$$d_z = \frac{hc}{2E \sin \varphi} \tag{2.35}$$

Depending on the conductivity of the material, the surface is the first nodal (for metals) or anti-nodal (for nonconductive materials) plane.

In TXRF, and also in GI-XRF, an important factor to consider is the intensity of this Standing Wave Field (SWF) at different distances from the reflector. The SWF indeed affects the excitation of the analyte present over the reflective layer: atoms that are excited from the anti-nodal plane are excited by an higher intensity field respect to atoms

that lays on the nodal plane, which are not excited. The intensity can be calculated as [34]:

$$I_{SW}(\varphi, z) = I_0 \left[1 + R(\varphi) + 2\sqrt{R(\varphi)} \cos\left(2\pi \frac{z}{z_d} - \mathcal{F}(\varphi)\right)\right] \quad (2.36)$$

where $\mathcal{F}(\varphi)$ is the phase-shift:

$$\mathcal{F}(\varphi) = \arccos\left[2\left(\frac{\varphi}{\varphi_c}\right)^2 - 1\right] \quad (2.37)$$

From these equations we can easily verify that $0 \leqslant I_{SW} \leqslant 4I_0$. Inside the sample instead, the field intensity (the evanescent wave) is damped exponentially as:

$$I_{EW}(\varphi, z) = I_0 \left[1 + R(\varphi) + 2\sqrt{R(\varphi)} \cos\left(\mathcal{F}(\varphi)\right)\right] \exp\left(-\frac{z}{\Lambda_F}\right) \quad (2.38)$$

for continuity reason the intensity of the evanescent wave on the reflector surface is equal to the intensity of the SWF.

From the definition of the Standing Wave Field and the Evanescent wave, we can describe three common cases: the analysis of a bulk sample, the analysis of a sample deposition and the analysis of a buried layer in a substrate.

In the first case we collect the fluorescence signal coming from the sample I_B, which is proportional to I_{EW}. As the depth investigated depend on φ, as shown in equation 2.34, it changes with the angle:

$$I_B(\varphi) = I_n w_q \left[1 + R(\varphi) + 2\sqrt{R(\varphi)} \cos\left(\mathcal{F}(\varphi)\right)\right] \Lambda_F(\varphi) \quad (2.39)$$

where I_n takes into account all the proportionality factors influencing the intensity (emission probability, source intensity, detector efficiency...) and w_q is the areal concentration of the analyte. In this case as volume is excited only by an evanescent wave and we can neglect the signal attenuation.

The second case is usually analyzed through TXRF, as the sample is usually deposited on a quartz reflector. In that case we have to assume, and ensure, that the massive thickness of the analyte is low enough to neglect attenuation phenomena on the incident and reflected radiation, moreover, we have to assume that the analyte deposition is rough enough to avoid reflections from the analyte-vacuum surface. In that case the intensity involving the analyte excitation depends on the SWF outside the reflector, on the analyte thickness and distribution (e.g. its granular size). For angles steeper than the angle of total reflection, the analyte is excited only once, thanks to the incident beam; at angles shallower than the critical angle we have to consider that the intensity depends on the incident angle, as the number of nodes and anti-nodes

inside the sample is also angle dependant. The fluorescence intensity can then be also four times higher (as we have said it is the maximum limit of Eq. 2.36) respect to the intensity obtained at steeper angles. As the sample thickness increases the number of nodes and anti-nodes inside the analytes starts to balance itself, thus the intensity starts to oscillate in function of the angle, increasing and decreasing depending on the number of nodes and anti-nodes. As a limit the intensity is doubled with respect to that measured at angles higher than the critical angles, as it is excited only from the source and reflected beams.

The last case arises if inside the reflector there is a buried layer, of thickness d, that is placed below the surface at a distance $z + d$ (the layer extends in a thickness $(z, z + d)$). In this case we assume that this layer contains a different analyte in low concentration, so that it does not affect the refractive index or the attenuation coefficient (for example implanted atoms in a substrate). Thus, the intensity is calculated integrating equation 2.39 over the buried layer thickness, obtaining:

$$I_{BL,q}(\varphi) = I_n w_q \frac{\varphi}{d} \left[1 + R(\varphi) + 2\sqrt{R(\varphi)} \cos\left(\mathcal{F}(\varphi)\right)\right] \exp\left(-\frac{z}{z_d}\right) \left[1 - \exp\left(-\frac{d}{\Lambda_F}\right)\right] \quad (2.40)$$

Multiple layers SWF

If the sample is consists of more than one layer, for example if a thin optically smooth layer deposited on top of the reflector, the direct beam crosses at least two interfaces, the one between the top-layer and vacuum, and the one between the reflector and the top-layer (figure 2.9). We can distinguish here two cases depending on the refraction index of the reflector with respect to the one of the top-layer:

A. if the refractive index of the reflector is lower than the refractive index of the top-layer, $n_r < n_t$, is possible to have total reflection on both the interfaces;

B. if the refractive index of the reflector is greater than the refractive index of the top-layer, $n_r > n_t$, total reflection is feasible only on the top-layer-vacuum interface.

In any case we have multiple interferences: (I) when the SWFs generated by the two layers superimpose; (II) when the evanescent wave inside the top-layer superimposes with the SWF generated in front of the reflector interface; and (III) when two reflected waves superimpose.

Outside the sample there is the superimposition of the direct and reflected beam that gives rise to the same SWF we have described before; if the beam is reflected from the top-layer the SWF only arises

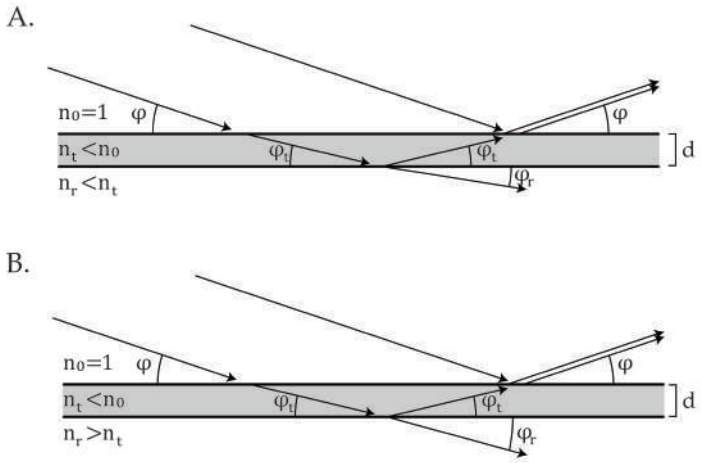

Figure 2.9: Path of the x-ray beam in a bi-layer sample in two cases: A. the reflector has a lower refractive index than the top-layer, $n_r < n_t$; B. the reflector has a higher refractive index than the top-layer, $n_r > n_t$

outside the sample, if the beam is reflected from the bulk, than the SWF also interest the top-layer excitation.

In this region we have to consider that there are also two reflected waves that interfere: the one reflected on the interface between the top-layer and vacuum, and the one reflected on the interface between the two layers; and this interference is not stationary, on the contrary, it is measured in X-Ray Reflectometry (XRR) experiments. The intensity of this propagating interference depends on the phase difference between the two reflected waves, thus it depends on the path-length crossed inside the top-layer, which is:

$$\Delta = 2d\sqrt{\varphi^2 - 2\delta_t} \tag{2.41}$$

Also here the same notes we have made for the SWF are valid, so there is a constructive interference if the phase difference is equal to an even multiple of π, and destructive if equal to an odd multiple. Thus the angles giving a constructive interference are:

$$\varphi_k^2 \approx \varphi_c^2 + \left(k\frac{\lambda}{2d}\right)^2 \tag{2.42}$$

while those that give a destructive interference are

$$\varphi_k^2 \approx \varphi_c^2 + \left(\frac{2k+1}{2}\frac{\lambda}{2d}\right)^2 \tag{2.43}$$

Minima and maxima are exchanged in the two cases (A and B) presented here, as if the beam penetrates inside the second layer there is a phase jump of π.

As we have said before, a SWF may interest the top-layer, due to the direct beam and the reflected beam from the bulk-top-layer interface. Its influence is similar to that described for a rough sample deposited on a reflector; anyway, in this case, the SWF senses also the interference of the evanescent wave propagating inside the top-layer. The intensity of the evanescent wave is inversely proportional to the intensity of the reflected beam, thus, for certain angles there will be a much higher excitation of the top-layer (anti-nodes of the SWF inside the top-layer and evanescent wave).

As the angle of irradiation increases, we will see an increasing signal of the top-layer intensity, then the signal will decrease as it penetrates more in the sample. The signal decrease is characterised by the presence of interference fringes, caused by the interference of the evanescent wave and the SWF. The fringes have maxima and minima exchanged with the maxima and minima observed in XRR measurements, as a maxima in the reflected waves correspond to a lower intensity evanescent waves, and they are more prominent in the case A, described above, as the intensity of the wave reflected on the interface between the two layers is much higher. Their frequency depends on the energy of the direct beam and on the top-layer thickness, while they amplitude depends on the difference on the density of the two layers (which means difference on the refractive index).

2.3.4 Instrumentation

A spectrometer to perform Grazing Incidence - XRF is very similar to those employed in TXRF and XRR. The first requirement is a high-power well-collimated source: in laboratory spectrometers usually diffraction sources are employed; another possibility is to employ synchrotron radiation, which is by nature intense and collimated. Like for AR-XRF the collimation is needed to reduce the angular divergence of the source, and to ensure that for each measure we can retrieve a small angle of irradiation (the divergence should be in the order of 1–0.1 mrad). Besides, the source needs to be monochromatic, as all the reflective and refractive properties of the materials are energy dependant. The detector, like for TXRF instrumentation, is usually placed in front of the sample, and has to offer the greatest solid angle of detection, to enhance the signal acquisition, which is damped by the high source collimation (figure 2.10A). For this reason, in detectors with large crystals placed closed to the sample surface are employed. Finally, the source needs to be rotated around the sample to excite it at different angle as the scanning affects only a small angular range. Another configuration can be obtained instead by tilting the sample.

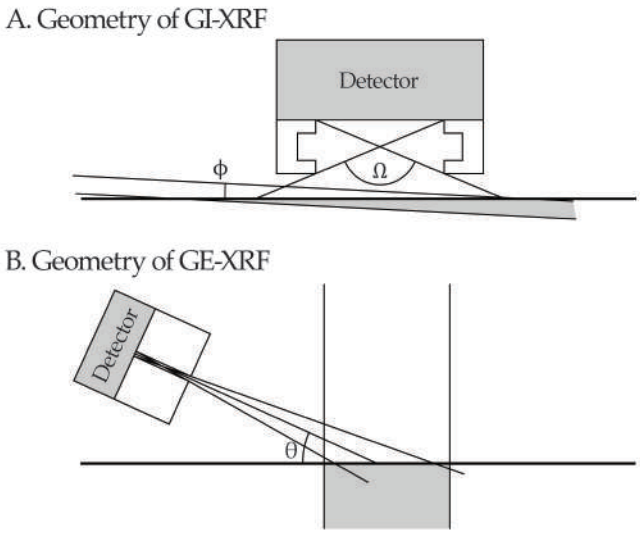

Figure 2.10: Geometry employed to perform Grazing Incidence (A.) and Grazing Emission (B.) XRF measurements. In the first case the sample is irradiated at grazing angle with a high flux, monochromatic source, with low divergence; and the signal is collected perpendicularly with a detector with a high solid angle of detection. In GE-XRF the sample is irradiated perpendicularly, and the fluorescence signal is collected at grazing angles with a highly collimated detector.

2.4 GRAZING EMISSION XRF (GE-XRF)

Grazing Emission - XRF is the sister technique of GI-XRF, as they employ the same principles, even if the set-up is inverted [7, 21]. Indeed, the geometry of analysis is the opposite we have seen for the Grazing Incidence technique, as here the irradiation is perpendicular to the sample surface (as is the detection in GI condition) and the fluorescence characteristic signal is collected at grazing angles (figure 2.10B). In this case the critical angles are not calculated in function of the source energy but in function of the emission energies, that are by definition monochromatic. In this case the considered radiation that is affected by refraction and reflection, indeed, is not the direct radiation, but the fluorescence radiation; the signals coming from deep inside the sample impinge the surface and are bent toward the perpendicular, thus they are detected at angles that are steeper than the angle of total external reflection calculated for each fluorescence energy. The only signals that can be detected at angles that are lower than the total reflection angles, are those produced on the surface of the sample; that is an important analogy with GI-XRF, where at angles below the critical angle only the signal emitted thanks to the propagating evanescent wave could be detected. Also in GE-XRF thus, the analyzed depth depends on the angle of analysis.

As, the fluorescence radiation from inside the sample is detected only for angles steeper than the critical angles of total-reflection calculated for the fluorescence energies, each signal begins to rise at different angles: the fluorescence lines with a higher energy will then be collected at lower angles, while the less energetic lines will be collected at steeper angles.

2.4.1 The principle of microscopic reversibility

The relationship between GE-XRF and GI-XRF can be derived from the principle of microscopic reversibility and reciprocity [8, 20, 55]: two sufficiently small radiating dipoles at two distinct position $\vec{r}_1$ and $\vec{r}_2$, with moments $\vec{p}_1$ and $\vec{p}_2$, satisfy the reciprocity law if:

$$\vec{\mathcal{E}}_1(\vec{r}_2) \cdot \vec{p}_2 = \vec{\mathcal{E}}_2(\vec{r}_1) \cdot \vec{p}_1 \tag{2.44}$$

where $\vec{\mathcal{E}}_j(\vec{r}_k)$ are the field generated in position k from the radiating source at position $\vec{r}_j$. This principle assesses that a switch in the detector and source position will not change the result of the experiment.

From this principle we could infer that if the energy involved in the experiment and the sample investigated is the same, the results obtained from the two techniques will also be the same. Actually, the energy involved are different, as the source energy in GI-XRF is always higher than the fluorescence energy in GE-XRF, thus the critical angles and the attenuation values are different, and the angular distribution is changed. Nevertheless, thanks to the principle of microscopic reversibility, the same calculations made for GI-XRF can be adapted also for GE-XRF, changing the energy values (from the source to the fluorescence energy) and the angles (from the impinging angle to the detection angle).

2.4.2 Comparison with GI-XRF

As the geometry is switched, and the sample is irradiated perpendicularly, no evanescent wave is produced on the sample, and no total-external reflection is ever produced. An important implication of the lacking of total-external reflection is the lack of SWF in front of the reflector. Instead, if we consider a multi-layered sample, at each interface there is a finite chance of having the reflection of the beam, thus the fluorescence beam can be reflected multiple times. In this case, if we consider quantum-physic the wave function of the fluorescence beam can interfere with itself, modifying the possibility to be detected by the detector.

A comparison of the two techniques, and thus also of the principle of the microscopic reversibility, can be observed by considering at the

equations employed to calculate the primary radiation intensity [43, 76, 77]:

$$I_q^{GI}(\phi) = G_q(\phi) P_q I(E) \int_0^\infty \rho(z) w_q(z) \left|\mathcal{E}(\phi, z, E)\right|^2 A(E_q, z, \theta) dz \tag{2.45}$$

$$I_q^{GE}(\theta) = G_q(\theta) P_q I(E) \int_0^\infty \rho(z) w_q(z) \left|\mathcal{E}(\theta, z, E_q)\right|^2 A(E, z, \phi) dz \tag{2.46}$$

where G_q is the geometrical factor containing also the detector efficiency, P_q is the emission probability, $I(E)$ is the excitation intensity; $\rho(z)$ and $w_q(z)$ are respectively the sample density and the analyte concentration; $\mathcal{E}$ is the electric field generated in the sample, and A is an attenuation factor of the fluorescence or direct radiation.

With respect to these equations it must be remarked that for GI-XRF the excitation intensity is given by the SWF, while for GE-XRF is given by the source intensity, weighted by the attenuation factor. Instead, GI-XRF must be corrected for the attenuation of the fluorescence radiation, which is already taken into account for the calculation of the SWF in GE-XRF. If, for thin layers, the attenuation factors A can be neglected, then the difference resides in the SWF calculations.

Another important difference on the signal intensity is due to the attenuation path, in GE-XRF the main attenuation is in the detection side, as the fluorescence signal must cross a longer path-length inside the sample before reaching the detector, instead for GI-XRF the main attenuation is in the irradiation side of the experiment. This causes a decrease of efficiency in GE-XRF, as here a major depth, which is not detected, is excited; while in GI-XRF only the layer of interest is excited. Anyway, we must also take into account that in Grazing Incidence analysis the irradiated area is much bigger, and it usually exceed the area detected, thus a big part of the fluorescence emitted is outside the active volume of the detector. This efficiency difference may be reduced using Charge-coupled Device (CCD) detectors in GE experiments, that collects at the same time the fluorescence emitted from different depths, optimising the measurement, and increasing the total solid angle of the experiment.

2.4.3 Instrumentation

As the sample is irradiated at high angle, and no reflection or refraction are required in this side of the experiment, any kind of source can be employed, like polychromatic x-ray tubes, synchrotron radiation, accelerated particles or radioactive materials [33, 35, 39, 64, 73, 74, 77]. Moreover, no requirements are posed on the size or distribution of the source, so that lenses or collimators can be used to perform micro-analysis or mapping [22]. This is a great advantage as this wide

choice of sources can be afforded more easily by a laboratory and can be adapted to the laboratory necessity [60]. Besides, in this way the source size or nature can be optimized for the experiment and the sample composition or structure.

Instead, a small divergence is required for the detection of the fluorescence signal: to collimate the detector window is possible to employ a pin-hole collimator or a slit, aligned with the rotation axis. As the low divergence is required only in the direction of rotation, employing a slit allows to collect more signal without any loss in resolution.

Another alternative is to use a pixelated detector, like a CCD, placed perpendicularly to the sample surface; in this case the angular resolution depends on the distance and on the pixel size. The use of a CCD detector better exploits the signal coming from the sample, as the whole profile is collected at the same time, besides, as no rotation is necessary, the system is more stable as no element moves during the acquisition [5, 6, 65, 66].

2.4.4 Fluorescence intensity

To calculate the angular dependence of the fluorescence, one must firstly consider the fraction of intensity of the direct beam that is absorbed by the analyte at depth z. This value, calculated also in the Sherman's equation 2.9 is:

$$I_a(z) = P_q \int_{S_q}^{E_M} I_0(E)\tau_q(E)\rho(z)\exp\{[-\rho(z)\mu(E,z)z]\}dE \tag{2.47}$$

where I_a is the absorbed intensity. It can also be discretized considering a sample made of n layers, and considering the excitation of a volume dz of thickness $z_{m-1} - z$ inside the layer m:

$$I_a(z) = P_q \int_{S_q}^{E_M} I_0(E)\tau_q(E)\rho_m \exp\left[-\sum_{j=1}^{m-1} \rho_j \mu_j(E,z)d_j - \rho_m\mu_m(E,z)(z_{m-1} - z)\right]dE \tag{2.48}$$

The calculation of the intensity emitted follows then the calculation of the SWF in the layer m, due to the multiple reflection inside the layer, the transmission and reflection probabilities, and the attenuation

of the fluorescence radiation. The full derivation is reported in [20], here is reported the result:

$$I_q(\theta) = A_m \left(\prod_{j=0}^{m-1} \left| t_j^{\downarrow} \right|^2 \right) \int_{z_m}^{z_{m-1}} \left[\frac{I_a(z_j)}{4\pi} \exp\left(-2 \sum_{j=1}^{m-1} \mathrm{Im}(k_z^j) d_j - 2\mathrm{Im}(k_z^m)(z_{m-1} - z_m) \right) |\chi_{even} + \chi_{odd}|^2 \right] dz \quad (2.49)$$

where $k_z^j = k\sqrt{n_j^2 - \cos^2\theta}$ is the fluorescence wave number parallel to the z axis, inside the layer j, A_m is a multiplicative factor considering the amplitude of the downward propagating wave, and χ_{odd}, χ_{even} represent the interferences due to even and odd reflections:

$$\chi_{odd} = \frac{R_m^{\uparrow} \exp\left(2ik_z^m(z - z_m)\right)}{\prod_{j=1}^{m} \left[1 - r_{j-1}^{\downarrow} R_j^{\uparrow} \exp\left(2ik_z^j d_j\right)\right]} \quad (2.50)$$

$$\chi_{even} = \frac{1}{\prod_{j=1}^{m} \left[1 - r_{j-1}^{\downarrow} R_j^{\uparrow} \exp\left(2ik_z^j d_j\right)\right]} \quad (2.51)$$

$R_j^{\uparrow}$ takes into account all the reflections on all the interfaces below the z_j interface, that can be calculated recursively as:

$$R_j^{\uparrow} = \frac{r_j^{\uparrow} + R_{j+1}^{\uparrow} \exp\left(2ik_z^{j+1} d_{j+1}\right)}{1 + r_j^{\uparrow} R_{j+1}^{\uparrow} \exp\left(2ik_z^{j+1} d_{j+1}\right)} \quad \text{for } 0 \leqslant j < N-1 \quad (2.52)$$

$$R_{N-1}^{\uparrow} = r_{N-1}^{\uparrow} \quad \text{for } j = N-1 \quad (2.53)$$

Finally, the coefficients $t_j^{\downarrow}$, $r_j^{\downarrow}$ and $r_j^{\uparrow}$ represent the downward and upward transmission and reflection coefficients defined as:

$$r_j^{\downarrow} = \frac{k_z^j - k_z^{j+1}}{k_z^j + k_z^{j+1}} = -r_j^{\uparrow} \quad (2.54)$$

$$t_j^{\downarrow} = 1 - r_j^{\downarrow} = \frac{k_z^j}{k_z^{j+1} + k_z^j} \quad (2.55)$$

3 INSTRUMENTATION

3.1 IAEA'S MULTIPURPOSE XRF SPECTROMETER OF THE NSIL

AR-XRF analyzes have been carried out using a multipurpose microbeam scanning XRF spectrometer developed by the Nuclear Science and Instrumentation Laboratories (NSIL) of the International Atomic Energy Agency (IAEA), Seibersdorf, Austria [81]. The spectrometer can perform different kinds of measurements, as it is equipped with two Silicon Drift Detectors (SDDs) and a movable sample-holder, so it can be employed to perform both 2D mapping and Confocal - XRF experiments (3D mapping). The experiments have been carried out using a diffraction X-Ray tube with a Mo anode (3 kW), set with a voltage of 45 kV and an intensity of 40 mA.

The source is equipped with a monolithic glass polycapillary lens (X-Ray Optical System, Inc.), mounted on a holder that allows to focus the beam through translation and tilting. The size of the irradiated spot at the focus distance is approximately 25 µm for Mo K_α X-Rays.

The SDD employed has an active area of 10 mm^2, a crystal of 450 µm thickness and an 8 µm Be window; its energy resolution is 135 eV at 5.9 keV. The detector is positioned at 45° over the xz-plane (figure 3.1).

For AR-XRF analysis this detector was collimated with a vertical slit, which has an opening of 60 µm and is 5 mm height, with a thickness of 600 µm. It is placed vertically in front of the detector, and its distance with the sample is of 17 mm. Thus, the mean angular resolution is 5 mrad (a minimum of 4.5 mrad at the top and a maximum of 5.6 mrad at the bottom of the slit). The slit has been created in laboratory using two iron slits of 300 µm thickness and openings of 200 µm, one of the two slits has been cut and glued over the other to reduce the opening width. All the procedure has been done with a microscope to ensure the alignment of the slit and the width size. The choice to use a slit instead of a cylindrical collimator was made to realize an increase of the signal from the sample, indeed the vertical slit, aligned with the axis of rotation allows to collect the signal spread along this axis without losing angular resolution. The effective probed volume of the sample, considering the source diameter and the slit is of $490 \times 85 \mu m^3$ [54].

The samples are mounted on a stage that provides a 3D movement (x, y, z) and a rotation α around the vertical axis (y-axis). To ensure a better alignment of the sample in the AR-XRF analyzes, we devel-

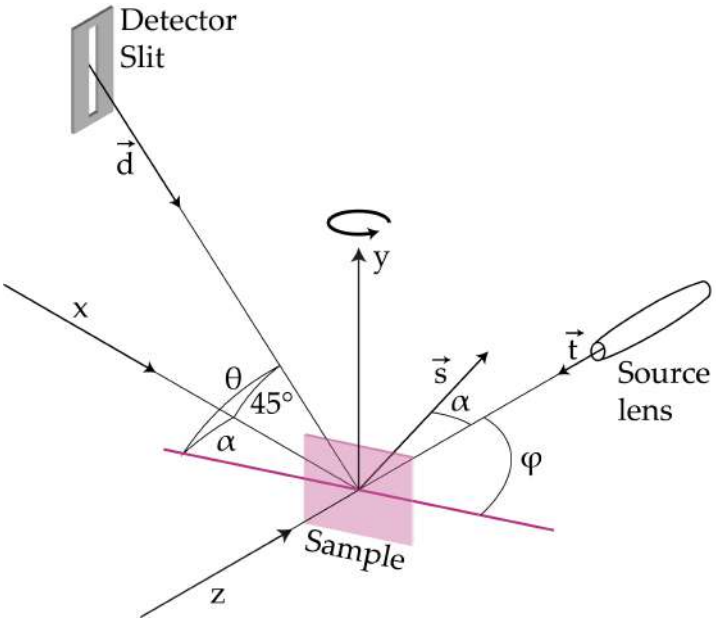

Figure 3.1: Scheme of the multipurpose XRF spectrometer of the NSIL, the source collimated with a polycapillary lens is aligned with the z-axis, while the sample rotates around the y-axis, and the detector lays on the xy-plane, impinging at 45° on the xz-plane. The slit is placed vertically in front of the detector.

oped a sample holder that allows us to move manually the sample independently to the stage and to align its surface to the rotation axis.

The spectrometer is also equipped with a microscope directed to the focus point; the depth of the microscope lens is very narrow so that if the object is visually in focus, it is also in the focus volume of the spectrometer.

3.2 ELETTRA XRF BEAMLINE

Grazing Incidence and Grazing Emission XRF measurements have been performed at the XRF beamline (whose scheme is represented in figure 3.3 of the Elettra Synchrotron, (Basovizza, Trieste, Italy). Elettra is a third-generation synchrotron that employs an operating energy of 2 GeV and 2.4 GeV. The beamline is run under the supervision of both Elettra and IAEA.

The choice to perform these kinds of measurements at the beamline is due to the high brilliance and tunability of the synchrotron light, a characteristics of the utmost importance if we want to analyze trace elements and nanolayers in complex samples. The tunability indeed allows to optimize the excitation of an analyte, thanks to the possibility of irradiating the sample with an energy slightly higher than the analyte absorption edge.

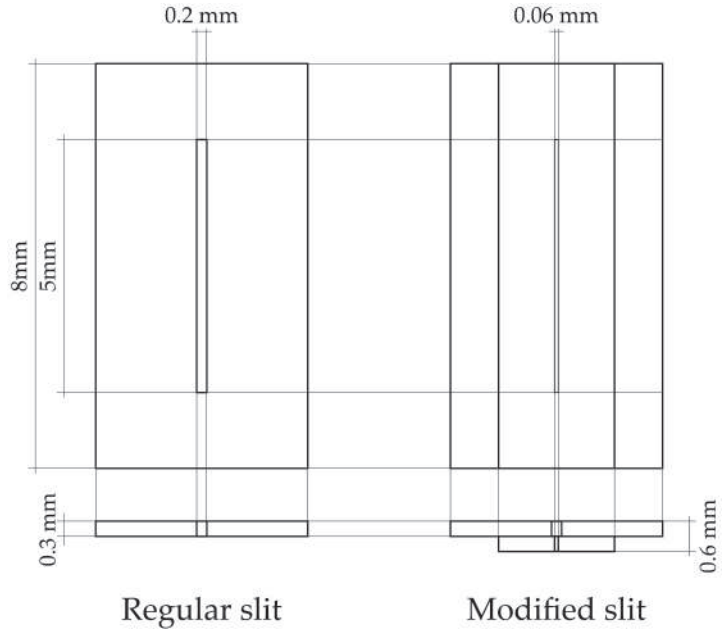

Figure 3.2: Technical scheme of the slit employed for AR-XRF: on left the original slit, on right the modified slit that allows a better angular resolution of about 5 mrad.

The synchrotron light enters the beamline through a bending magnet, that ensures an energy range wide enough (2 keV to 14 keV) to excite the K and L lines of many element of interest to the CH field. The source is monochromatized with double crystals or multilayer monochromators (see table 3.1), the monochromator choice depend on the employed energy, on the needed intensity and required resolving power. That is why for GI-XRF we employed the Si(111) crystals, that allows a high resolving power in spite of the source intensity; while for GE-XRF we chose to use the RuB_4C coated multilayer, ensuring a higher flux with a lower energy resolution (not needed for this kind of experiments).

Table 3.1: Monochromators employed at the XRF beamline of Elettra Synchrotron of Trieste

Monochromator	Energy range	Resolving Power
Si (111)	3700 eV–14 000 eV	~ 1 eV at 7000 eV
InSb	2000 eV–3700 eV	~ 1 eV at 2200 eV
RuB_4C	4000 eV–14 000 eV	~ 55 eV at 1000 eV ~ 180 eV at 14 000 eV
NiC	1500 eV–8000 eV	
RuB_4C	700 eV–1800 eV	

After the monochromator, the beam is focused with a toroidal refocusing mirror coated with rhodium, and enters the Higher Order

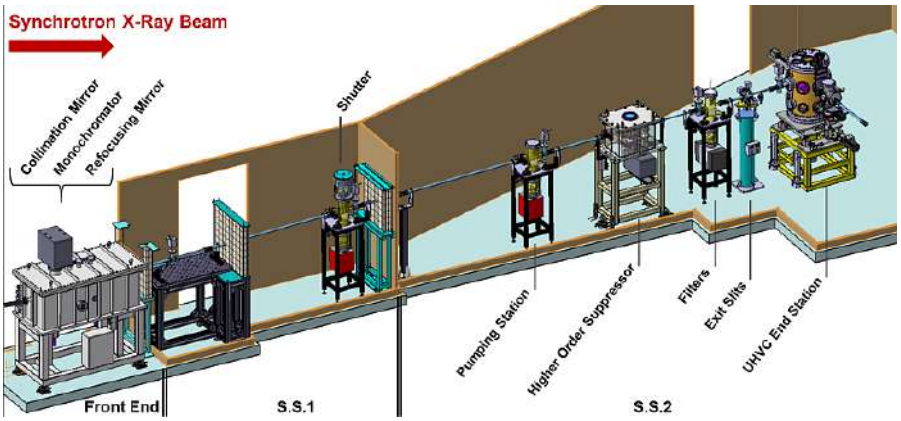

Figure 3.3: Scheme of the XRF beamline of Elettra, from left the photons are emitted by the storage ring, to right where the chamber of analysis is placed.

Suppressor (HOS). The HOS absorbs the energies of higher order transmitted by the monochromator, ensuring the monochromaticity of the source; it is made of a pair of parallel plane mirror coated with rhodium and carbon. Finally the beam enters the end-station with a divergence of 0.15 mrad and a maximum size of $450 \times 300\mu m$.

The end-station is an Ultra High Vacuum (UHV) chamber containing a seven-axis manipulator (Huber, Germany), [32]. The manipulator ensures a full movement and rotation of the sample, allowing the movement in the space along the x, y, z axes and rotation around the θ and ϕ axes. Moreover, the movements of the X-ray monitoring detectors are achieved through an additional rotational axis, 2θ, and a linear stage (Diode), allowing to perform XRR measurements.

In the UHV chamber non-vacuum compatible samples can also be analyzed, as a Be window can be placed between UHV chamber and the beamline. Besides, the chamber communicate with the outside through a pre-vacuum load lock, divided by a gate valve. This system reduces the time required to obtain the optimal pressure, as the chamber never reach the atmospheric pressure. Indeed, the sample is inserted into the load lock, where the pressures reaches a value of 1×10^{-6} mbar, then the gate valve can be opened and the sample enters the UHV chamber where it is positioned on the seven-axis manipulator.

The sample is then monitored through two video cameras: a large macro-camera to observe the sample position and a micro-camera to display the measured sample point.

3.2.1 Detectors

The UHV chamber allows to collect the fluorescence signal with two SDDs, an XFlash 5030 (Bruker Nano GmbH, Germany) and a Miniaturized SDDs (Amptek, USA).

The XFlash 5030 position is fixed at 90° respect to the direction of the source beam, while the distance with the sample can be changed, increasing or reducing the solid angle of detection. Instead, the Amptek detector is placed on the manipulator, thus, even if its distance respect to the sample is fixed, the angle respect to the beam can be chosen.

The silicon crystal of the XFlash 5030 is nominally 450 µm thick; the detector has a nominal active area of 30 mm^2 and an energy resolution of 131 eV at the Mn Kα fluorescence line (5.9 keV). The crystal is protected by a Super Light Element Window of the type AP 3.3, and a Zr collimator prevents the detection of photons at the edge of the crystal, improving also the energy resolution and the peak to background ratio. Also, an electron tap, a permanent magnet, prevents the detection of photo- and Auger electrons emitted from the sample surface, allowing an optimum detection of element with $Z < 14$. The electron trap can be replaced by a 8.5 µm Be window.

The Amptek detector has an active area of 25 μm^2, the silicon crystal is 500 µm thick and is covered with a Be window 8.5 µm thick. The energetic resolution is of 131 eV at the Mn Kα fluorescence line. To ensure a good angular resolution for XRR and GE-XRF measurements, a multilayered collimator is placed in front of the detector, it is made of a slit 300 µm thick, with a width of 200 µm and an height of 5 mm.

Finally the Beam flux is monitored through the Beam Monitoring System (BMS), based on a 4-channel solid state sensor composed of a free standing polycrystalline Chemical Vapour Deposit diamond plate with a thickness of 12 µm.

4 ANALYSIS OF GILDED COPPER

To firstly evaluate the suitability of AR-XRF for the analysis of Cultural Heritage samples, the technique has been tested on laboratory-made metallic layered samples. These samples have the advantage of having a known composition and structure, allowing to reduce the number of variables that must be taken into account, as the density and thickness of each layer is known.

4.1 THE SAMPLES

The gilded samples are made of a pure copper plate of a thickness of 100 µm, that can be considered of infinite thickness for the employed energies, covered with a layer composed of a stacking of lemon-gold foils (an alloy made of 75 % Au and 25 % Ag), from now on referred to as 'golden foils'. The golden foils, which have been bought from an art store, have a nominal thickness of 0.15 µm. To test the technique, we have prepared three different samples with a top layer composed of an increasing number of golden foils, respectively 3, 5 and 7 foils. The samples are summarized in table 4.1. The deposition of the golden foil is not expected to give flat and parallel layers, we expect a certain lateral inhomogeneity given by the folding of the foils and their fracturing. In this sense thus, these samples, even if they are made in laboratory, present characteristics that adequately represent situations observed in the field of CH, where imperfections, fractures, and signs of aging modify the sample surface.

To better observe the presence of fractures and folds, we have also prepared polished cross-sections that have been analyzed with a Scanning Electron Microscope (SEM). Thanks to this analysis we could get information on the layer's deposition and shape. The images have been acquired in Backscattered Electron (BSE) mode with a Tescan

Table 4.1: Laboratory made samples description

Sample	Description
Au-3	100 µm of copper and 3 golden foils
Au-5	100 µm of copper and 5 golden foils
Au-7	100 µm of copper and 7 golden foils

VEGA TS5136XM scanning electron microscope (HV = 20 kV, I_e = 54 µA).

Thus with this first experiment we want to evaluate if AR-XRF can be used to calculate the total thickness of the top layer.

4.1.1 Preparation of the samples

The top layers have been created by gluing the gold foils over the copper plate using an alcoholic gilding glue (Charbonnel© Mixtion Gold Size - 3 hours). As the glue is made of light elements and is very thin, its attenuation of the copper and silver K_α, and gold L_α emission (namely 8.09 keV and 9.71 keV) is negligible, and no further corrections will be considered. To prepare the samples the glue has been spread over the copper plate and left drying for 2 h to 3 h, depending on the room temperature and the air humidity. Then the golden foil has been placed over the glue and left for other 2 h to dry. The process has been performed multiple times to obtain the desired golden layer thickness.

4.2 DATA ACQUISITION AND TREATMENT

All the data treatment and analysis of the metal samples AR-XRF profiles have been performed using several Python (version 3.7.11)[23] homemade scripts created for this very purpose. The process can be divided into four steps:

1. Processing the XRF spectra and using the elemental intensities to create the AR-XRF profiles;
2. Creation of the fitting functions for the AR-XRF profiles;
3. Fitting of the profiles;
4. Calculation of the mass thickness of the chosen layer.

Note that the scripts for the steps 3 and 4 use different equations for considering self-attenuation in the bulk layer and/or the attenuation in upper layers that will be discussed in the related sections.

4.2.1 Measurement protocol

For each sample we performed three AR-XRF measurements; each one is composed of 126 XRF spectra. The dwell time for the collection of a spectrum is of 2 s, and the angular step is of 0.4°, for a total of 50° of tilting for each measurement. The tilting of the samples ranged nominally from −5° to 50°.

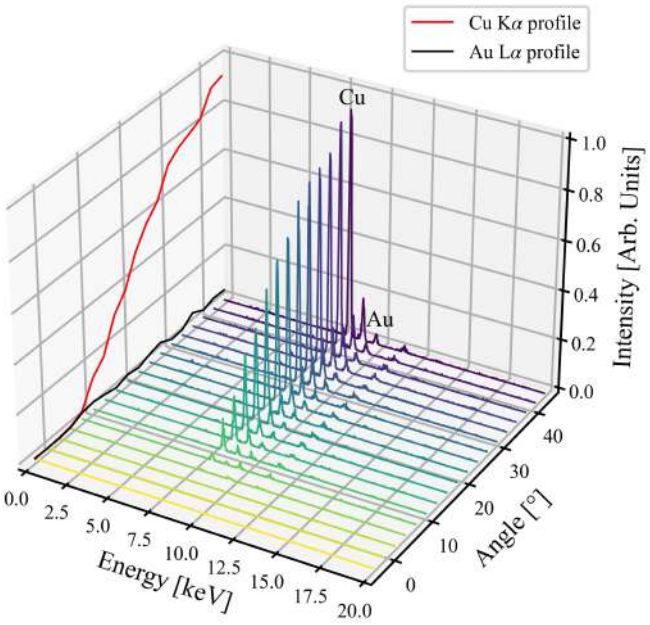

Figure 4.1: Example of AR-XRF profile, the pictures shows each XRF spectra and the profiles of Cu and Au, here for simplicity showed as peaks intensities and not as peaks areas.

4.2.2 Creation of the AR-XRF profiles

AR-XRF profiles were creating starting from the peak areas of the measured XRF spectra, indeed the intensity of each element depends both on the structure of the sample and on the angle of measurement, see Eq. 2.10. During the collection of all the XRF spectra at the different angles, we obtain as many profiles as the identified fluorescence lines, so the number of points of each profile equal to the number of spectra (Figure 4.1).

The intensity can be obtained either by summing the intensity of the channels of the selected Region of Interests (ROIs) or fitting the peaks with appropriate peak shape models (or an appropriate software like Pymca or Q-AXIL). Fitting is the better choice when there is superimposition of fluorescence lines, as it is not possible to distinguish the intensity of the different elements; however, for low counting statistics, which is the case of the spectra collected at short measurement time or near grazing angles, the program may return inaccurate or non-physical values (like negative values) or may not be able to fit the spectrum at all (warning: this case depends on the accuracy of the selected model for the spectrum background, and its intensity). In this case, especially if the background is flat and has a low intensity, the selection of ROIs may be a better choice.

As the samples are not perfectly flat and there is no optical/mechanical system to obtain an alignment of the surface parallel to the

detector, we had to take into account a possible misalignment of the sample-holder system. In this case a correction of the zero of the angular scanning is needed. As the signal coming from the surface of the sample starts rising at the critical angle $\theta = \alpha_c$, it can be used as the zero of the scanning; indeed, below this value no signal of the top layer can be detected. The AR-profile of an element present in the top-surface layer can then be used to correct the zero of each angular scanning.

4.2.3 Creation of the fitting functions

The fitting function of the intensity of an element q present in the bulk or in a layer of non-infinite thickness has been obtained starting from the Sherman's equation for a monochromatic source, similar to Eq. 2.10. In this case we consider both the self-attenuation within the considered layer and the attenuation caused by the covering layers:

$$I_{m,q} = \frac{\Pi_{q,E_0}}{\sin\phi} \frac{1 - \exp\left[-\rho_m h_m \left(\frac{\mu_m(E_0)}{\sin\phi} + \frac{\mu_m(E_q)}{\sin\theta}\right)\right]}{\frac{\mu_m(E_0)}{\sin\phi} + \frac{\mu_m(E_q)}{\sin\theta}} \exp\left[-\sum_{j=0}^{n-1} h_j \rho_j \left(\frac{\mu_m(E_0)}{\sin\phi} + \frac{\mu_m(E_q)}{\sin\theta}\right)\right] \quad (4.1)$$

where:

$$\Pi_{q,E_0} = \frac{\Delta\Omega}{4\pi} \eta(E_q) G_q P_q w_q I_0(E_0) \tau_q(E_0) \quad (4.2)$$

As these equations shows both the angle of irradiation and of detection, and as these angles are unequivocally related with the angle of tilting, it is better to rewrite them in function of the tilting angle, reducing the number of variables. To perform this change of variable it is useful to convert the spectrometer geometry in vectorial form. From figure 3.1 the vector of the source, $\vec{t}$, lays on the z-axis, thus $\vec{t} = (0, 0, -1)$; the vector of the detector can be written as $\vec{d} = (1/\sqrt{2}, -1/\sqrt{2}, 0)$, and the vector perpendicular to the sample surface, which represents its tilting, is $\vec{s} = (\sin\alpha, 0, \cos\alpha)$, were α is the tilting angle. We can then calculate the angle of irradiation as the angle between the plane of the sample surface and the source vector; similarly, we can calculate the angle of detection.

Remembering that, $\vec{\pi}$ represents the vector perpendicular at a plane π, and $\vec{l}$ is the vector representing the direction of a line l, the angle β between the plane and the line can be calculated as:

$$\beta = \arcsin \frac{\left|\vec{\pi} \cdot \vec{l}\right|}{\|\vec{\pi}\| \left\|\vec{l}\right\|} \quad (4.3)$$

obtaining for our geometry:

$$\sin\phi = \sin\left(\frac{\pi}{2} - \alpha\right) = \cos\alpha \tag{4.4}$$

$$\sin\theta = \vec{d}\cdot\vec{s} = \frac{\sin\alpha}{\sqrt{2}} \tag{4.5}$$

Thus, we can substitute these values in Eq. 4.1 obtaining:

$$I_{m,q} = \frac{\Pi_{q,E_0}}{\cos\alpha}\frac{1-\exp\left[-\rho_m h_m\left(\frac{\mu_m(E_0)}{\cos\alpha}+\frac{\sqrt{2}\mu_m(E_q)}{\sin\alpha}\right)\right]}{\frac{\mu_m(E_0)}{\cos\alpha}+\frac{\sqrt{2}\mu_m(E_q)}{\sin\alpha}} \exp\left[-\sum_{j=0}^{n-1} h_j\rho_j\left(\frac{\mu_m(E_0)}{\cos\alpha}+\frac{\sqrt{2}\mu_m(E_q)}{\sin\alpha}\right)\right] \tag{4.6}$$

For a bi-layer sample, we can rewrite this equation as:

$$I_{m,q} = \frac{\Pi_{q,E_0}}{\cos\alpha}\frac{1-\exp\left[-\rho_m h_m\left(\frac{\mu_m(E_0)}{\cos\alpha}+\frac{\sqrt{2}\mu_m(E_q)}{\sin\alpha}\right)\right]}{\frac{\mu_m(E_0)}{\cos\alpha}+\frac{\sqrt{2}\mu_m(E_q)}{\sin\alpha}} \exp\left[-h_i\rho_i\left(\frac{\mu_i(E_0)}{\cos\alpha}+\frac{\sqrt{2}\mu_i(E_q)}{\sin\alpha}\right)\right] \tag{4.7}$$

For the analysis of our samples, we can then distinguish the two different cases: (I) the considered element is gold (or silver), present only in the golden top layer, whose intensity is affected only by self-attenuation, (II) the considered element is copper, contained only in the bulk of infinite thickness, affected by the attenuation of the golden top layer.

In the first case then we can rewrite Eq. 4.7 as:

$$I_{Au,TL} = \frac{\Pi_{Au,E}}{\cos\alpha}\frac{1-\exp\left[-t_{TL}\left(\frac{\mu_{TL}(E)}{\cos\alpha}+\frac{\sqrt{2}\mu_{TL}(E_{Au})}{\sin\alpha}\right)\right]}{\frac{\mu_{TL}(E)}{\cos\alpha}+\frac{\sqrt{2}\mu_{TL}(E_{Au})}{\sin\alpha}} \tag{4.8}$$

In the second case we rewrite equation Eq. 4.7 as:

$$I_{Cu,BL} = \frac{\Pi_{Cu,E}}{\cos\alpha}\frac{\exp\left[-t_{TL}\left(\frac{\mu_{TL}(E)}{\cos\alpha}+\frac{\sqrt{2}\mu_{TL}(E_{Cu})}{\sin\alpha}\right)\right]}{\frac{\mu_{BL}(E)}{\cos\alpha}+\frac{\sqrt{2}\mu_{BL}(E_{Cu})}{\sin\alpha}} \tag{4.9}$$

where the subscripts TL and BL refer respectively to the top layer and the bulk. Knowing the composition of the bulk and the top layer, we can substitute the attenuation coefficients starting values with their corresponding values for Mo K_α excitation, reported in table 4.2. Thus, in Eqs. 4.8 and 4.9 we have only three unknown parameters: $\Pi_{Au,E}$, $\Pi_{Cu,E}$ and t_{TL}.

4.2.4 Fitting process

The fitting process consists in the application of Eqs. 4.8 and 4.9 to evaluate the three unknown parameters, and has been performed using the package *lmfit* (version 1.0.2) [42]. As the profiles characterizing the golden top layer and the bulk present different shapes and characteristics, their fitting has been carried out differently. For the bulk element, i.e., copper, we have divided the fitting process in two steps: (I) fitting of the background in a region with no copper signal, (II) fitting of the AR-profile as the sum of two functions:

$$f(\alpha) = p(\alpha) + b(\alpha) \tag{4.10}$$

where $b(\alpha)$ is the background calculated in the first step and $p(\alpha)$ is the AR-XRF profile, Eq. 4.9.

For the top layer element, gold, we just fitted the profile with a unique function:

$$f(\alpha) = I_{Au,TL} + b \tag{4.11}$$

where $I_{Au,TL}$ is calculated from Eq. 4.8 and b is the background.

The choice to employ with two slightly different methods is motivated by the fact that for the copper signal we could evaluate the background of the profile with a higher precision choosing a region without the copper fluorescence signal.

To proceed with the fitting, we have weighted each intensity with its uncertainty. By applying the package *lmfit* we could also easily evaluate the uncertainty of the fit with different values of sigma, for all the processes we considered the uncertainty with a 3σ confidence interval [42, 82].

4.2.5 Calculation of the mass-thickness of the golden layer

AR-XRF profiles depend on the concentration of the elements in the different layers of the sample, and on the layers thickness; as in this case the concentration is known we can compare the intensity of the analytes with their expected intensity calculated with the Fundamental Parameters method (FP method) [67]. In this case, we used the Sherman's equation for polychromatic radiation leaving out enhancement effects (Eqn. 2.9). The source radiation $I_0(E)$ has been deconvoluted following the work of Padilla et al. [49]. After the normalization, to compensate for geometric factor, measurement time and source intensity, the profiles obtained from the FP calculations have been compared with the fitted profiles through the reduced χ^2-method [18]. The massive thickness that minimized the reduced χ^2 has been chosen as top layer thickness.

4.3 RESULTS

4.3.1 The top layer structure

To observe the morphology of the golden layers, sections of the samples have been analyzed by means of SEM. Even though the glue employed to stack the golden foils and the copper bulk is made of light elements, and does not attenuate the fluorescence signal, it does contribute to the total volume of the top layer. In this sense, concerning the whole top layer, we can only retrieve its mass thickness, as we do not know the density nor the amount of glue between the layers. Nevertheless, we can retrieve the total thickness of the golden foils inside the top layer, using the density of the alloy. This problem related with the thickness and the density of a gilding has already been discussed by Ager et al. [1].

In the SEM images (Fig. 4.2) it is possible to see the structure of the gold top layer; the golden foils are clearly visible in the BSE images thanks to their high atomic number; it is also visible the glue layer between them, filled with polyhedric crystal. The crystals are due to the polishing procedure made with sanding paper. It's important to highlight that the foils are not perfectly flat and in many points are folded and broken, increasing the lateral variability of the structure; this variability is very important as it well represent real cases that can occur in the field of Cultural Heritage where the artifacts have been altered.

4.3.2 Fitting of the profiles

As the energy of Au L_α fluorescence line is centered at 9.71 keV and the Cu K_α at 8.04 keV, any interference occurs between these two lines, thus the intensity profiles have been obtained using only the ROIs method. In figure 4.3 you can see the profiles collected for the different samples, each colour represents one sample, for each sample we measured three spots, to correct for possible variability in the gold deposition.

It is evident from this figure that the copper profiles distinguish better the number of layers than the gold profiles, while the copper profiles show a general higher variability in function of the number of layers. The gold profiles of the samples Au-5 and Au-7 are very similar. All the profiles of each element have been fitted with the same parameters, reported in Table 4.2; moreover, with the package *lmfit*, is possible to select the boundaries of a parameter to avoid non-physical values, also these values have reported in the table. For each fit is has been given particular attention that the final value of a variable was not the same of the boundary, to allows the algorithm to converge to the minimum. To find the best fit the profiles intensities have been

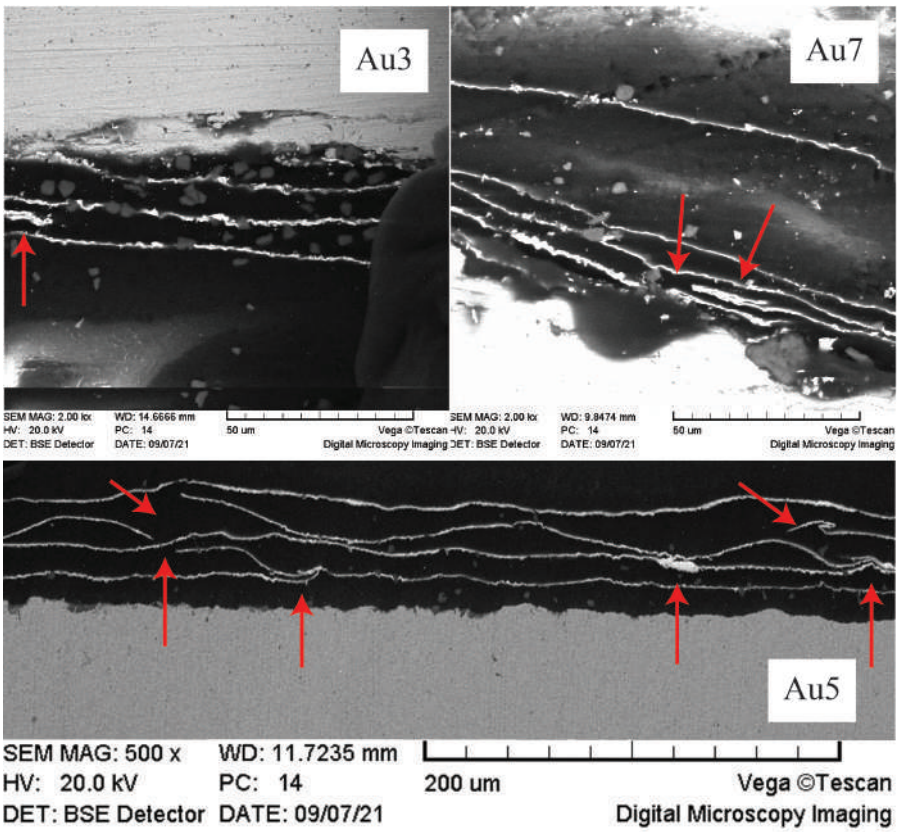

Figure 4.2: SEM-BSE images of the metal samples. Gold leaves are light thanks to their high atomic number; between the foils is possible to see the space filled by the organic glue, dark in the image. The polyhedric grains are due to the sanding paper used to create the polished section. In red arrows are highlighted fractures and folding of the golden leaves. For these images we would like to thanks prof. Maurizio Acciarri of Univerisity of Milano Bicocca.

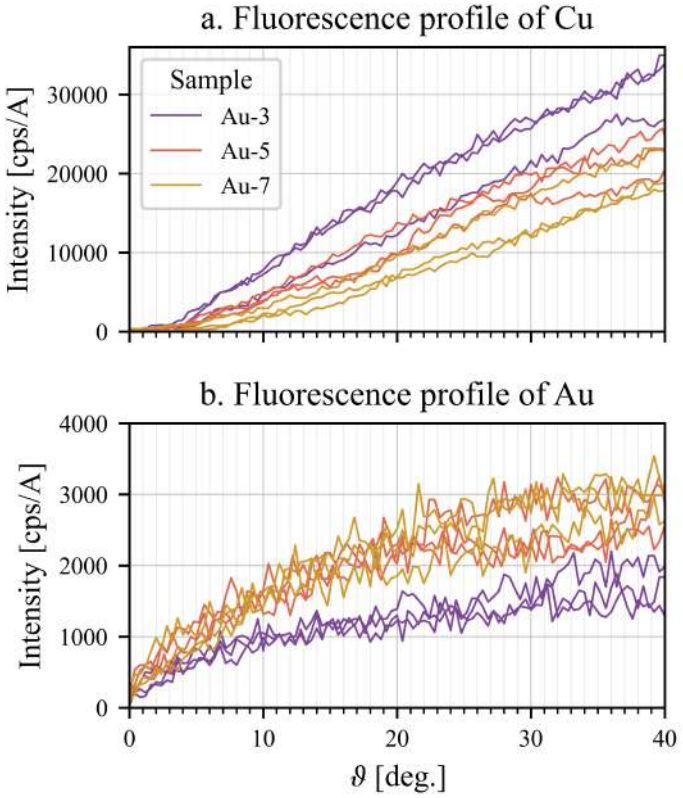

Figure 4.3: AR-XRF profiles of Copper K_α fluorescence line (a) and of Gold L_α fluorescence line (b) of the metallic samples Au-3, Au-5 and Au7. Each colour represents a sample, for each sample three spots have been measured. The count intensity has been normalized for the dwell time and the source intensity.

Table 4.2: Values employed for the fitting of the AR-XRF profiles of copper and gold. For each parameter a starting value and two boundaries' values has been chosen, the boundaries are needed to avoid the convergence in non-physical values.

Parameter	Starting value	Min. Value	Max. Value
Π_{Cu}	10^6	100	10^7
Π_{Au}	10^5	100	3×10^6
t_{TL}	5×10^{-6} cm	1×10^{-6} cm	2×10^{-2} cm
b	0	0	$100 + y_0$
$\mu_{BL}(E_0)$	49.052 cm^2/g	Fixed value	
$\mu_{BL}(E_{Cu})$	51.661 cm^2/g	Fixed value	
$\mu_{TL}(E_0)$	90.192 cm^2/g	Fixed value	
$\mu_{TL}(E_{Cu})$	206.172 cm^2/g	Fixed value	
$\mu_{TL}(E_{Au})$	127.846 cm^2/g	Fixed value	

weighted for their uncertainty, thus the residuals have been calculated as:

$$r(\alpha) = \frac{y_F(\alpha) - y(\alpha)}{\sigma_y(\alpha)} = \frac{y_F(\alpha) - y(\alpha)}{\sqrt{y(\alpha)}} \tag{4.12}$$

where $\sigma_y(\alpha)$ is the uncertainty of the fluorescence profiles, $y(\alpha)$ is the measured value, and $y_F(\alpha)$ is the value calculated with the Fundamental Parameters (FP)-method.

In appendix A it is possible to see the fit of the copper and gold profiles, in blue the original data, in black the fit profile and in red the 3σ confidence interval of the fitted data. In figures 4.4 and 4.5 two examples are plotted. On overall, the fit of the gold data give better results, with most of the times residuals between ± 0.5, and always lower than ± 1.0; copper fits instead have higher residuals, always lower that ± 5 thus we still consider the fits as good. It must be highlighted that most of the difference between the fit and the raw data is situated in the low angle region, between $0°$and$10°$, where the intensity is lower and higher data oscillation is expected.

In principle, the value of t_{TL} could be directly obtained from the fit; however, this variable presents a high correlation with Π (e.g., 0.908 ± 0.038 for the top layer) thus is not possible to rely on this value alone.

4.3.3 Comparing the fitted data with FP-calculated profiles

To perform the comparison the FP-calculated profiles have been directly calculated at the same angles of the fitted data; to avoid differences in the source intensity or in the geometrical factors (that do not

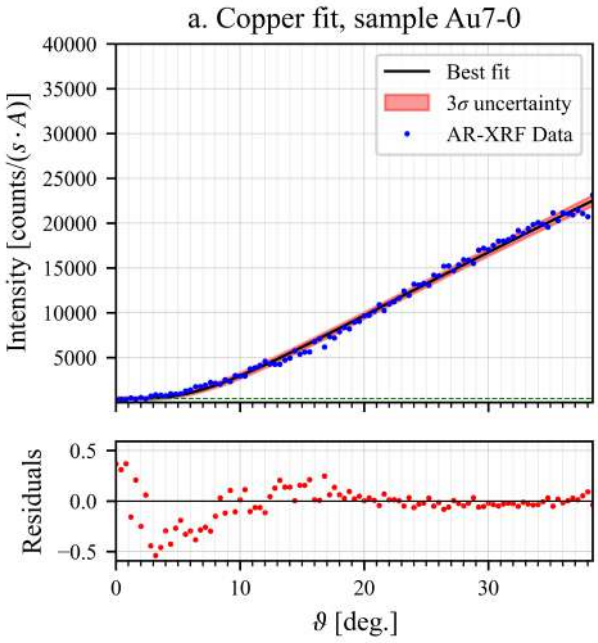

Figure 4.4: Fit of the copper profile of the gilded sample made of 7 golden foils. The dotted blue values are the raw data, the black line is the best fit, the red area is the 3σ region.

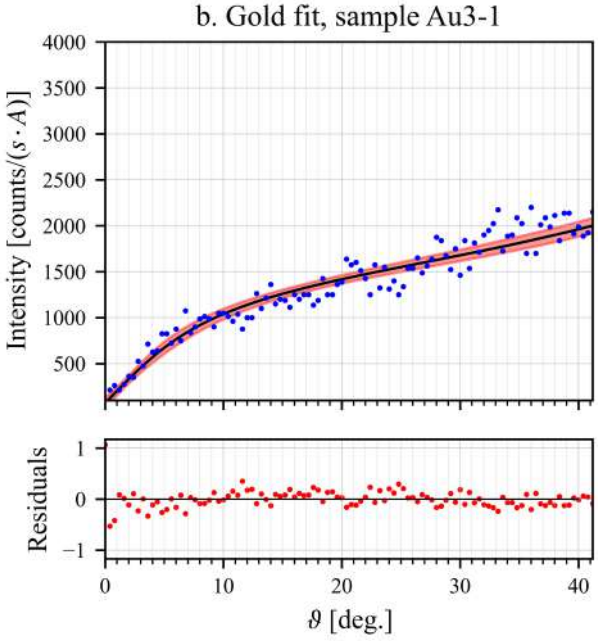

Figure 4.5: Fit of the gold profiles of the gilded sample made of 7 golden foils. The dotted blue values are the raw data, the black line is the best fit, the red area is the 3σ region.

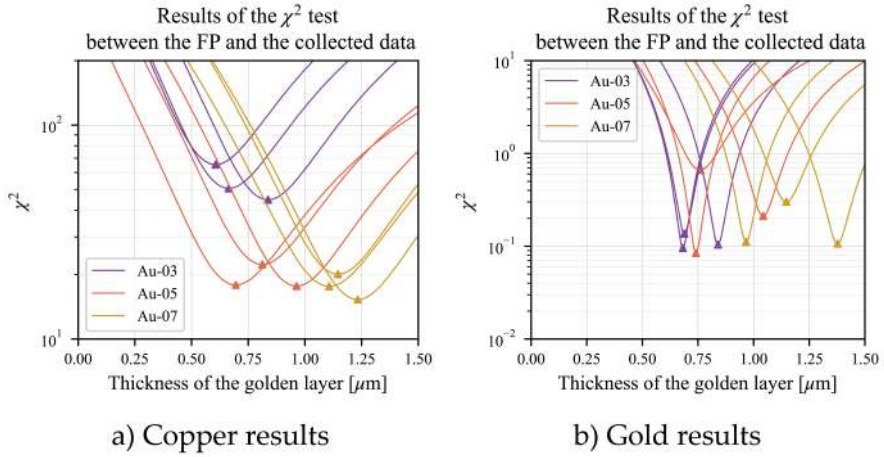

Figure 4.6: χ^2 of the copper (a) and gold (b) fitted profiles and the calculated profiles.

influence the shapes of the profile), both the fitted profiles and the FP-calculated ones have been normalized. Then the χ^2-method has been applied between the calculated profiles and the fitted data, to obtain the best match with the gold-layer thickness. As the χ^2-distributions shows a minimum corresponding to a gold-layer thickness, referring to that minimum we retrieved the top layer thickness, see triangles in figure 4.6.

4.3.4 Calculation of the gold layer thickness

Taking into account the lateral inhomogeneities shown by the SEM images (see figure 4.2), intrinsic to the sample production technique, the thicknesses of the top layers measured in the three spots for each sample have been averaged out. The results are in this way representative of the thickness of the whole layer covering the sample. The data, retrieved using the AR-XRF profiles, are shown in Fig. 4.7. The thicknesses calculated both using the attenuation of the top layer (profile of copper) and the self-attenuation of the top layer (profile of gold) are compatible, as they both fall inside the estimated errors. In this sense, the two methods, as expected, give the same results. As the error in the estimation for these gilded samples has proved to be always lower than 17 %, this technique seems actually to be a useful tool to analyze non-invasively gilded samples in the field of CH.

If we compare the thickness of the single foil, calculated dividing the thickness of the golden top layer by the number of golden foils deposited on the copper plate (figure 4.8, we can see that the single foil thickness tend to reach the nominal thickness (0.15 µm) as the number of foils increases. This is due by the fact that the higher is the number of foils, the lower is the influence of foldings and fractures

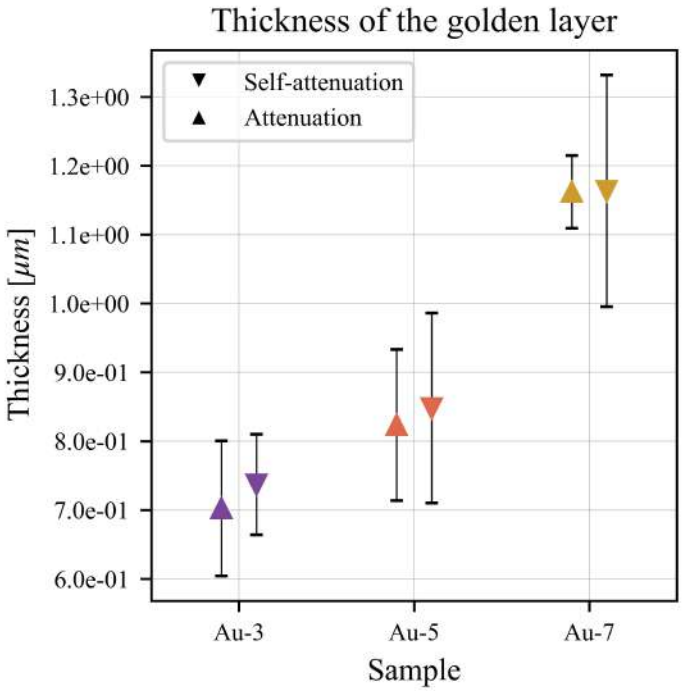

Figure 4.7: Thickness of the golden layer calculated using AR-XRF and the comparison with the calculated profiles. The triangle represents the data calculated employing the self-attenuation, thus the gold profiles; while the downward triangle represents the data calculated employing the attenuation, or the copper profiles

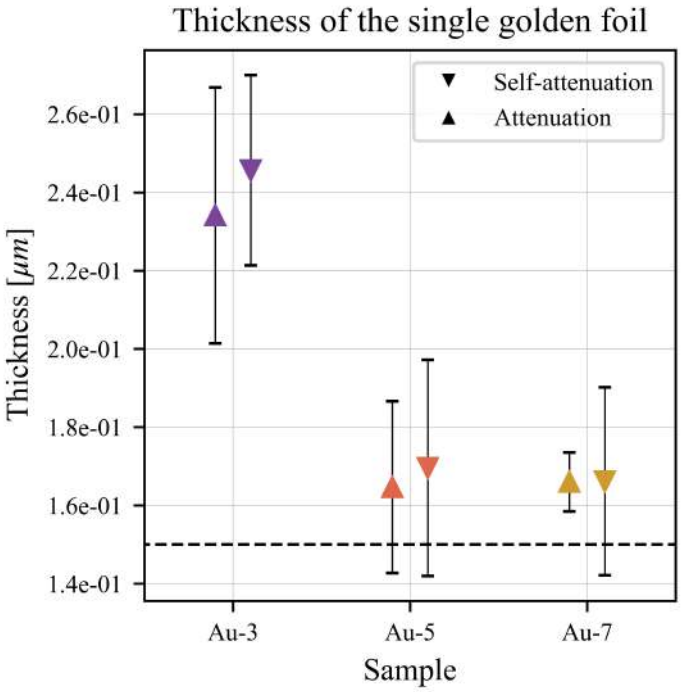

Figure 4.8: Thickness of the single golden foil composing the top layer, and nominal thickness of the golden foil (dashed line)

on the total thickness, thus the thickness of the single foil is measured with a higher accuracy.

5 PUEBLA CERAMIC ANALYSIS

The second step of the project consists in the evaluation of the applicability of AR-XRF for the analysis of more complex samples, where more variables affect the fluorescence profiles of the analytes. The sample here analysed is a sherd of a Majolica ceramic coming from Puebla, Mexico, depicted in figure 5.1. The only knowledge we have of this artifact is the composition of the white glaze, which is employed as a background for all the decorations, as it has been previously characterized by Padilla et al. [48]. The composition of the decorations and their thickness, instead, was unknown, and is the aim of this study.

5.1 THE CERAMIC SAMPLE

The sample analyzed is a majolica sherd with the size of nearly $7 \times 5 cm^2$ of the Puebla Policromo production (Mexico), presenting white, blue and black decorations.

Majolica is a distinct Hispanic category of glazed, wheel-thrown ceramics, distinguished by its soft earthenware paste covered by an opaque vitreous enamel or glaze. The addition of tin oxide to the glaze produces opacity, which is found also in the technically related French faience and English and Dutch delftware [28, 48].

The main characteristic of Majolica is indeed the white alkali glaze that covers homogeneously the ceramic biscuit. To obtain this homogeneous white opaque glaze, artisans employed minerals of lead and tin. Lead has been added to the glaze recipe since the Roman period, as it works as softener of the, allowing to heat at lower temperatures the artifact during the decoration process; instead, the addition of tin in the mixture works as opacifier. Tin reacts with the silica mixture to create small crystals of cassiterite (SnO_2); these crystals together with the presence of quartz, feldspars and air bubbles, scatter and reflect the light, creating the characteristic white appearance [28].

As the ingredients vary with the place of production and the availability of the raw materials, different recipes were followed around the world. In general, it was quite common to use a ratio of 1:6 lbs of tin and lead to prepare the ground mixture, to which different substances were added. In Italy, it was common to add sand, potash, and salt; while in Spain potash was substituted with wine lees, in Mexico instead potash was substituted with soda ash.

The blue decoration is characterized by the presence of cobalt as chromophore and is clearly not homogeneous in thickness: in the

Figure 5.1: Puebla ceramic sample *(courteously supplied by Gabinete de Arqueología, Havana, Cuba)*. The white glaze is characterized by the presence of tin and lead. The blue decoration by the presence of cobalt and the black decorations by the high amount of iron.

center, where the color is more intense, the glaze is thicker than along the borders, where the color is lighter.

The black decorations can be divided in two categories, the small stripes present a vitreous luster and seems very thin, while the black spots seem thicker and present small crystals with a submetallic luster. In both kind of black decorations, the main composing elements are iron and lead.

Roisine et al. [59] highlighted that common mineralogical forms that give the black color are melanotekite ($Pb_2Fe_2Si_2O_9$), hematite (Fe_2O_3) and magnetoplumbite ($PbFe_{12}O_{19}$), and their presence depends on the firing temperature. Melanotekite is stable at low temperatures ($\leqslant 875\,^{\circ}C$) and form small facetted plate crystals, usually covered with primary hematite, it seems indeed that hematite reacts with the silica-lead melt to form melanotekite. At higher temperature ($\leqslant 1022\,^{\circ}C$) melanotekite is dissolved and only secondary hematite is found, in this case hematite crystals are larger than the previous formed primary hematite and more faceted. Finally, at $1023\,^{\circ}C$ hematite dissolves to form magnetoplumbite, composed of micron-sized dark hexagonal platelets.

5.2 SAMPLE ANALYSIS AND QUALITATIVE COMPOSITION

The decoration of the ceramic sherd can be divided in three groups, the white decoration, the blue decorations, and the black decorations. The blue decorations in turn can be divided in light and dark, depending on the thickness of the blue glaze, while the black decorations present distinctive characteristics if we consider the black spots and the black stripes. The black stripes present a glassy lustre, and they seem to be embedded inside the white glaze, while the black spots show a metallic lustre and they seem to be on top of the white glaze. For this very reason we collected three measurement points for each kind of decoration: white glaze, light blue, dark blue, black spots and black stripes, mapped in figure 5.2.

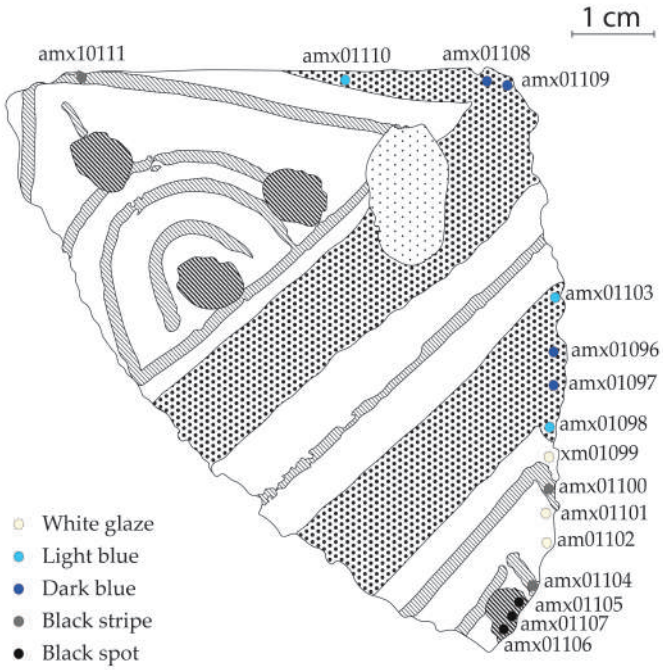

Figure 5.2: Map of the point collected with AR-XRF, the colour of the spots represent the colour of the glaze. The area with black dots represents the blue glaze, while the area filled with diagonal stripes represent the black decoration. The central region filled with small dots represent a fracture area.

As can be seen from the map, all the spots have been collected near the border of the sherd, this was a mere practical choice. As the distance between the source and the focus spot is of few millimetres, if we would have analysed areas in the centre of the ceramic during the tilting of the sample, its surface would have collided with the source collimator, thus the only points we could measure are those on the borders. This problem can be resolved by increasing the source-sample

distance. All the spots have been analysed with the same protocol employed for the metallic samples, with an angular range from −5° to 45°, an angular step of 0.4°. The dwell time for each spectrum collection is of 20 s.

The only known information we have on the ceramic composition is given by Padilla et al. [48], whose data are summarized in table 5.1.

Table 5.1: Composition of the white glaze in the Puebla sample, from Padilla et al. [48]

Glaze composition (wt.%)					
Na_2O	4.3	SiO_2	54.1	Fe_2O_3	0.76
MgO	0.23	K_2O	3.08	SnO_2	3.5
Al_2O_3	9.7	CaO	1.2	PbO	26.0

The white glaze is characterized by a high content of lead (26 %) and the presence of tin (3.5 %). Besides, the white glaze is thick enough and the white layer can be considered of infinite thickness, thus no signal from the ceramic bulk is detected.

To have a first idea of the qualitative composition of the ceramic decorations we considered the cumulative spectra, shown in figure 5.3, which were obtained summing all the individual XRF spectra of the AR-XRF measurement. All the cumulative spectra collected from the same type of decoration have been averaged out to obtain a final spectrum that could be representative of the general composition of each glaze. These spectra allow to distinguish each glaze by its own composition.

The white glaze (yellow spectrum), for instance, is mainly characterized by the presence of lead and tin, whose L_α line can be distinguished between the potassium and calcium K_α lines. It also contains traces of iron, manganese, and nickel.

Blue decorations (dark blue and blue spectra) contain a high amount of lead (the L_β line intensity is higher respect to that of the white glaze), cobalt as a chromophore and arsenic, usually co-related to cobalt; also, a higher amount of iron is attested. Cobalt and arsenic are usually difficult to quantify especially if iron and lead are present in the sample, as Co K_α fluorescence line superimpose partially with Fe K_β fluorescence line, and As K_α fluorescence line superimpose with Pb L_α fluorescence line.

Finally, black decorations (green spectra) are characterized by a high content of iron (higher for the thicker spots and lower for the thinner black stripes) and a lower amount of lead.

In all the coloured glaze, we cannot distinguish or detect the L_α fluorescence line of tin, which is characteristic of the white glaze. As Sn L_α is a low energy line (3.44 keV), it provides information on the superficial presence of tin; thus, the absence of this line in the

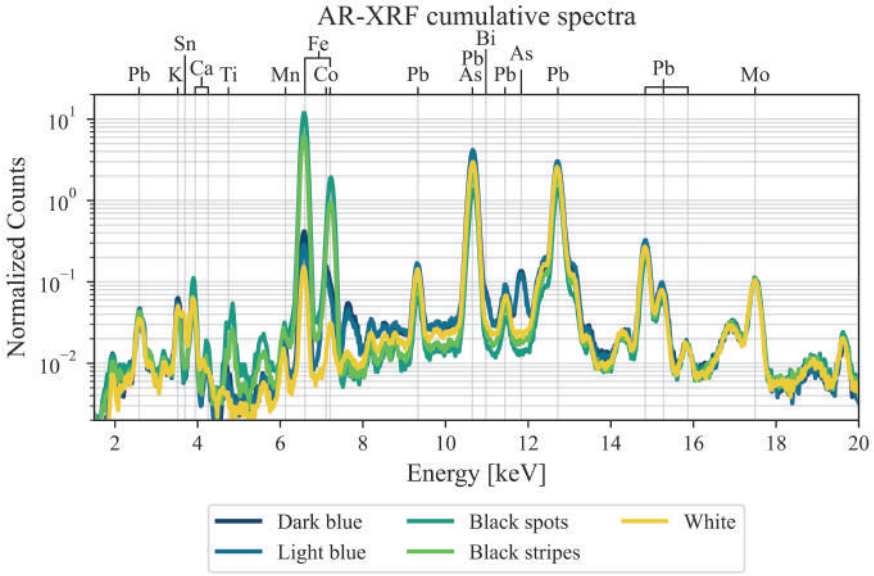

Figure 5.3: Cumulative spectra of the decorations, each colour represent one decoration; on the top x-axis the element, on the bottom axis the energy. The spectra are weighted for the Rayleigh scattering peak for representation purposes and is shown in logarithmic scale.

decorated spots suggests that, if present, tin is found in a deeper layer. Finally at 2.35 keV is possible to see the M lines of lead, suggesting that lead is always present on the sample surface, independently of the decoration.

5.3 DATA ANALYSIS

After the experience with the metallic samples, we opted for a different approach. The analysis of the Majolica sample revealed the presence of many more elements; thus, we could not apply the ROIs method to retrieve the intensity profiles and a fitting of the XRF spectra, performed with *Pymca* [63], was necessary. In this way we could distinguish the fluorescence profiles of overlapping elements fluorescence lines like Co K_α (6.93 keV) and Fe K_β (7.06 keV), or As K_α (10.54 keV) and Pb L_α (10.55 keV). Besides, we decided to compare the FP-profiles directly with the peak areas arising from the raw data, to ease the calculation and perform a more robust analysis, introducing less errors in the data treatment process.

Finally, due to the geometric and shadowing effect, we did not relate the profiles as they have been obtained but we compare the ratio of the profiles. In particular as lead is the main element composing the white glaze, i.e. the background, the profiles of interest have been normalized for the profile of lead L_α fluorescence line. The use of an intensity ratio instead an the absolute intensity values has a second

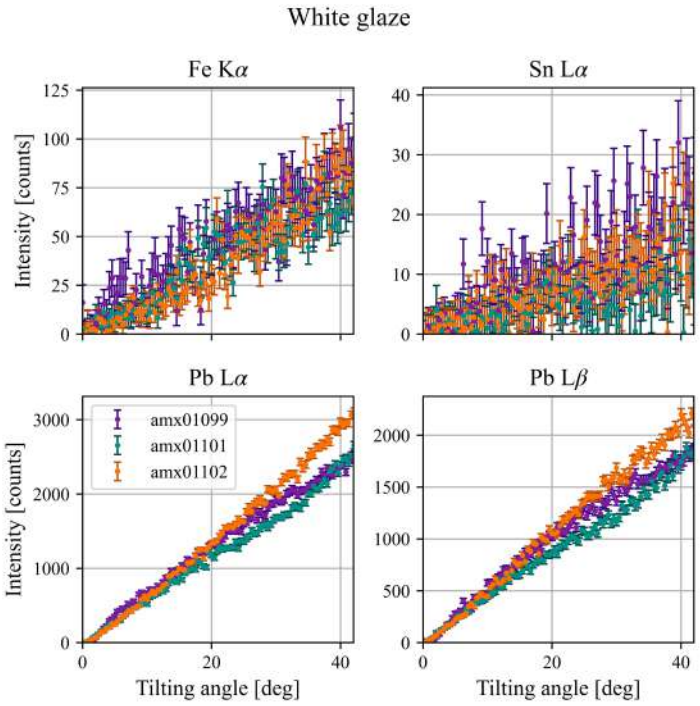

Figure 5.4: Intensity profiles of Sn L_α, Fe K_α, Pb L_α and Pb L_β for the measures on the white glaze.

advantage, as all the factors affecting homogeneously the intensity of the profile, like the source flux (but not the source shape distribution) can be neglected.

The analysis of the data has then followed these steps (for more details see Appendix B):

1. fit of the spectra using *Pymca*;
2. correction of the angle using a surface element fluorescence profile;
3. calculation of the ratios;
4. comparison of the ratios with those calculated with the FP-method.

To obtain information on the structure we firstly considered the raw profiles of the main elements, shown in figures 5.4, 5.5, 5.6.

In Fig. 5.4 are depicted the main profiles of the white glaze, that we consider a reference due to its homogeneity and the fact that we know the composition. Thus you can see the profiles of lead (both Lα and Lβ) and those of other two elements: tin (employed as opacifier) and iron. These two elements have a really low intensity, anyway all the profiles show a similar behaviour.

For the black glazes we present in figure 5.5 the two main elements: iron, which is the chromophore, and lead; for iron only the K_α line is

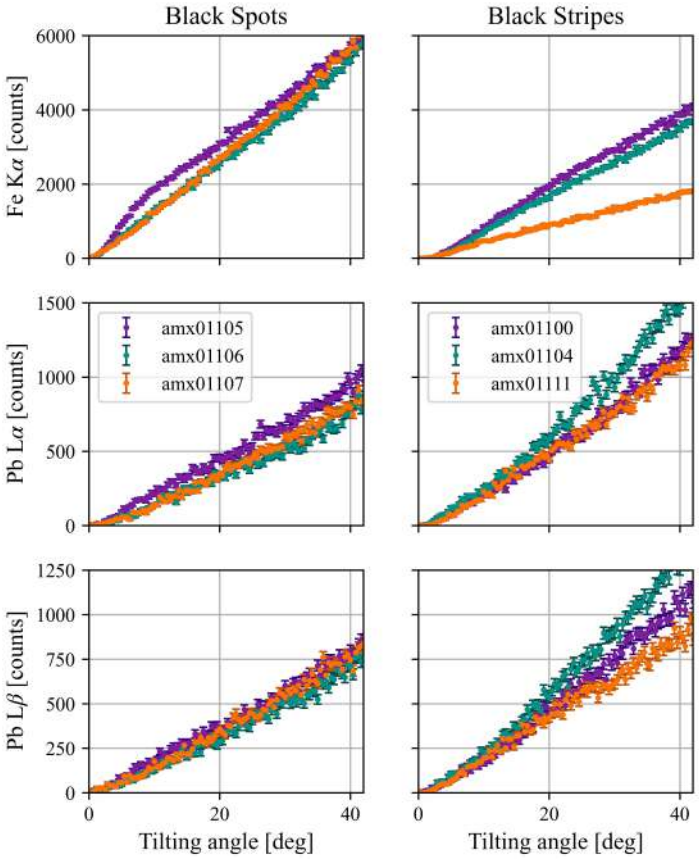

Figure 5.5: Intensity profiles of Fe K_α, Pb L_α and Pb L_β for the measures on the black glaze decorations. On left the data of the black spots, on right those of the black stripes.

shown. We can observe that the intensity of iron is higher in the black spots than in the black stripes, while lead has a higher intensity in the stripes. Besides, we can observe that profiles of the three fluorescence lines appears more homogeneous for the black spots respect to the stripes; this is probably because all the measured point of the black spots have been collected on the same decoration, while the sample points of the black stripes have been collected on different areas of the sample, thus the variability of the structure in the latter case in enhanced.

Finally, it is interesting to look at the raw profiles of the blue decorations, depicted in figure 5.6. We plotted here the lead profiles, which we use as reference for our normalization, and the chromophore elements profiles (cobalt and iron). The shape of the profiles of the dark blue glaze, especially for the point 01097 and 1108, do not increase steadily, as the others. These two profiles show decrements after 32° and 37°, probably due to the tridimensional shape of the decoration. The blue glaze indeed is not flat but is thicker in the center (dark blue glaze) and thinner on the borders (light blue glaze). Thus, when analyzing the borders, the glaze can be considered flat, even though it

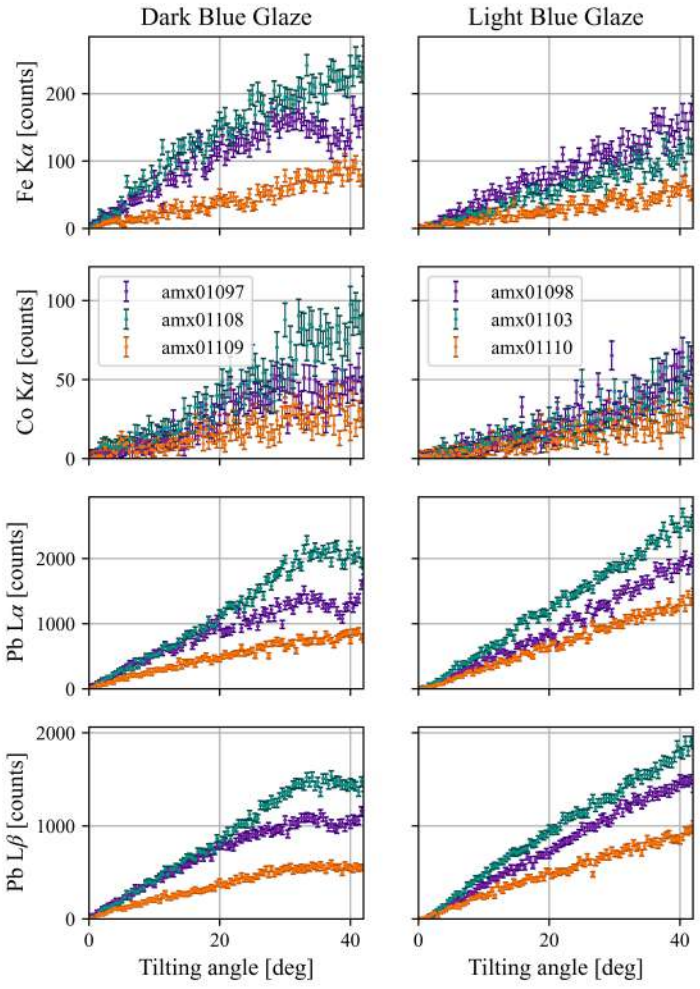

Figure 5.6: Intensity profiles of the blue decorations of Fe K_α, Co K_α, Pb L_α and Pb L_β. On left the profiles obtained on the darker blue areas, on right those obtained on the lighter areas.

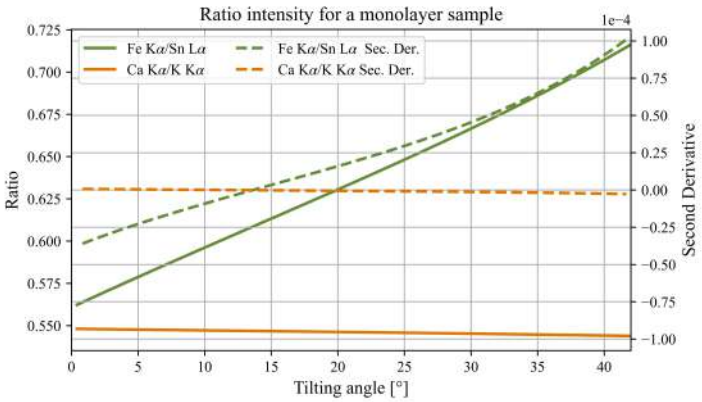

Figure 5.7: Fe K_α/Sn L_α (green) and Ca K_α/K K_α (orange) ratio for a bulk layer with a composition like that of the white glaze. Dashed the second derivatives, y-axis on the right.

is not parallel to the sample surface, while the dark blue areas may give shadowing effects. For this reason, the use of intensity ratio can be more effective, as geometrical effects that would influence the intensity of all the elements in the same way are removed.

5.4 RATIO OF TWO ELEMENTS

Before proceeding with the ratio data analysis, we evaluated the shapes of the profile's ratios calculated for different samples with the FP-method. They have been calculated for a bulk sample and for a bi-layer sample, in the second case we changed different parameters to observe how these affected the ratio distribution. The hypothesis of a three-layers case will be left out for now, as too many parameters are involved.

5.4.1 Ratio distribution - Monolayer

For the first example we have calculated the Fe K_α/Sn L_α and the Ca K_α/K K_α intensity ratios for a possible composition of a bulky glaze, similar to the one of the ceramic sample; shown in figure 5.7. From the picture we can observe that the ratio tends to increase (or decrease) linearly: as the composition is always the same, the intensity variation is due to the path-length crossed by the source and by the fluorescence radiation that is related with the geometry of analysis. To attest the linearity we can also observe that the magnitude of the second derivative is lower than 10^{-4}.

5.4.2 Ratio distribution - Bilayer

Considering then a bilayer system, we can describe the ratio distributions using two variables. Indeed, if we fix the bulk composition, and we consider the bulk to be of infinite thickness for the employed energies, we can generate all the possible distributions varying the top layer thickness and the top layer composition. To create a system that we can easily describe and analyse we can suppose the top layer to have a ternary composition, containing one element no present in the bulk (Fe), one element which is also present in the bulk (Pb) and a closure element. The first element will be the numerator of our ratio, while the second element will be the denominator. We consider here the bulk to have the same composition of the white glaze of the Puebla ceramic, and the top layer to have a compositional range of:

- Fe_2O_3: $x \in [10, 60]\%$,
- PbO: $y \in [5, 35]\%$,
- SiO_2: $100 - x\% - y\%$

this same system will be used later to describe the black decorations.

This specific system is then described by three variables, at which we must add the tilting angle of the sample: two variables describe the top layer composition, and one is the top layer thickness.

If we change the thickness of the top layer and we keep constant its composition, fig. 5.8 top, we can observe that the ratio of iron and lead decreases with the increase of the tilting angle. If we look at the first derivative, fig. 5.8 centre, we see that for low and high angles the derivative is close to 0, and that the thicker is the top layer the bigger is the range at low angles for which the derivative is close to 0. This is due by the fact that for low angles the signal comes only from the top layer, which can be considered, in this region, as infinitely thick; then we start collecting signal from the bottom layer, and we see a change in the ratio. Finally, the variation of path-length inside the top layer become more and more negligible, and the dependence on the angles of irradiation and detection on the attenuation become weaker. We can also observe that the minimums of the first derivative, or the zeros of the second derivative, shift toward higher angles as the thickness increases. If the thickness of the top layer increases, then the range of low angles for which it can be considered of infinite thickness increases, until we reach the limit case, in which for the whole range of scan we cannot get any information from the bulk. To emphasise the difference between the low angles and high angle intensity ratios, the profiles are plotted for a top layer composition very different respect to the bottom layer; if the concentration of the two elements is similar, the difference between the two layers is given only by the difference in the attenuation coefficient, as the concentration can be simplified

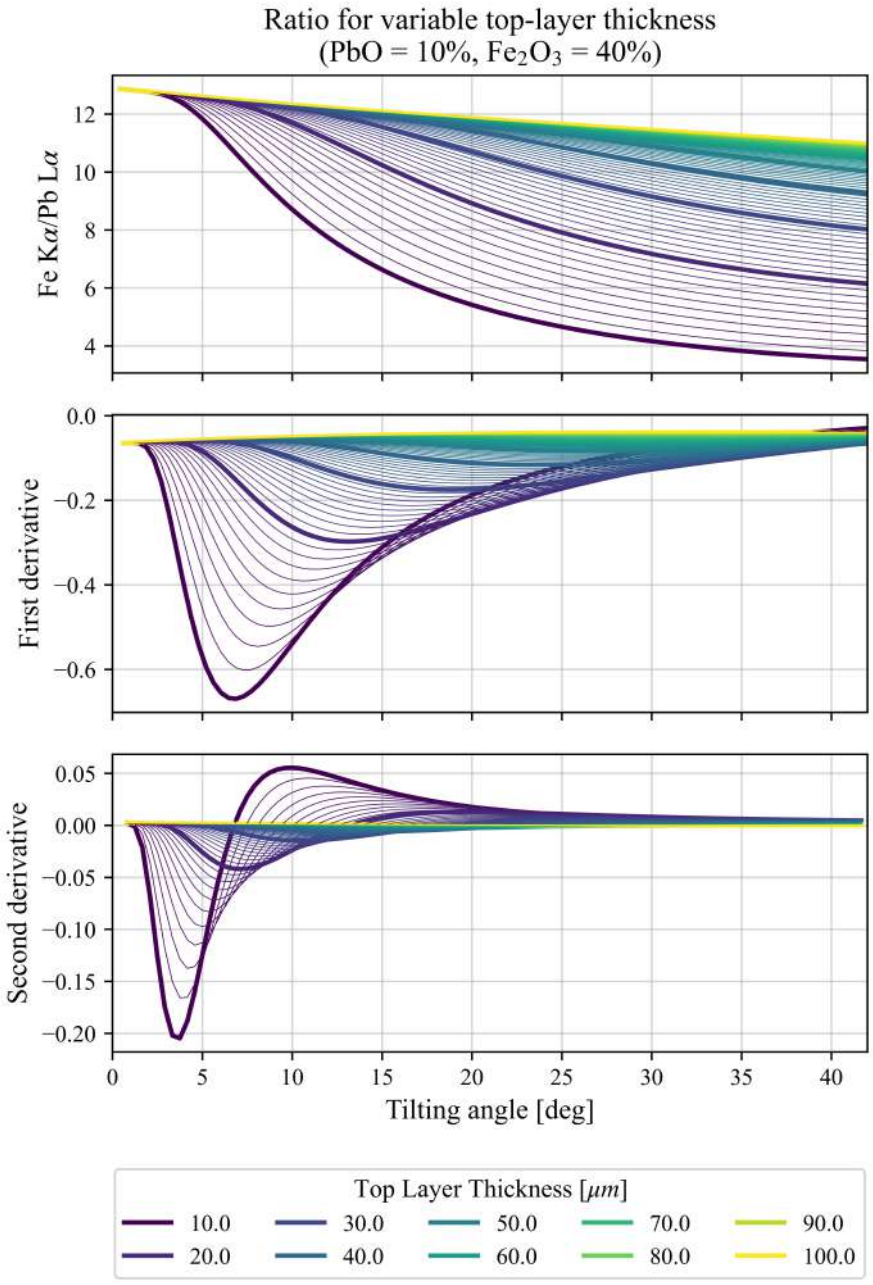

Figure 5.8: Intensity of iron and lead K_α and L_α fluorescence lines in function of the top layer thickness. On top the ratio profiles, in the centre plot its first derivative, on the bottom plot its second derivative

in the calculation of the ratio. In the second derivative plot, fig. 5.8 bottom, we can observe that in the limit case of a top layer of infinite thickness, the ratio become linear, as the concavity is nearly zero in all the angular range.

If the thickness of the top layer is constant and only the lead concentration changes, Fig. 5.9, we observe that the intensity ratio become more linear as the concentration of lead increases. For the maximum lead concentration (35 %), which is higher than the lead concentration of the bulk (26 %) the ratio profile resemble the one of a monolayer, as we see the first derivative absolute value decreases going closer to 0, and the concavity reduces. As the lead amount increases, also the attenuation coefficient and the density increase, as it implies a lower concentration of SiO_2. The increase in massive thickness causes the top layer to behave more like an infinite thickness layer, even if the linear thickness is always the same.

Finally on figure 5.10, it is possible to observe the influence of the iron concentration on the profiles. This plot has been created considering a low lead concentration and a top layer thickness of only 20 µm, to avoid the infinite thickness case limit, and remain in the medium thickness range. As you can see the difference in the ratio intensity at low and high angles drop as the iron concentration reduces. In the presented case the lower is the iron concentration the lighter is the matrix of the top layer: reducing then both density and attenuation. The influence of the top layer to the excitation and the attenuation of the fluorescence signal of the bulk become less prominent, and again, we will reach a limit case of a pseudo-monolayer sample (there is a top layer here, but its influence will be negligible). For the range calculated here we see that the monolayer case is never really observed, as the first and the second derivatives will never be close to 0 for the whole angular range. Nevertheless, we can observe that the minimum of the derivatives shifts toward low angles and reduces in magnitude as the iron concentration decreases; thus only when the angle is very low there the influence of the top layer can be observed.

We must keep in mind thus that the composition has different effects: (I) change in the number of atoms that participate in the fluorescence emission of a fluorescence line; (II) change in the layer characteristics as attenuation, density and, consequently, massive thickness. In particular as the global composition is 100 %, a reduction/increase of an element concentration will lead to an increase/reduction of another element. If the substituting element has a higher/lower attenuation or density, it will cause an increase/decrease of the massive thickness and attenuation properties of the top layer.

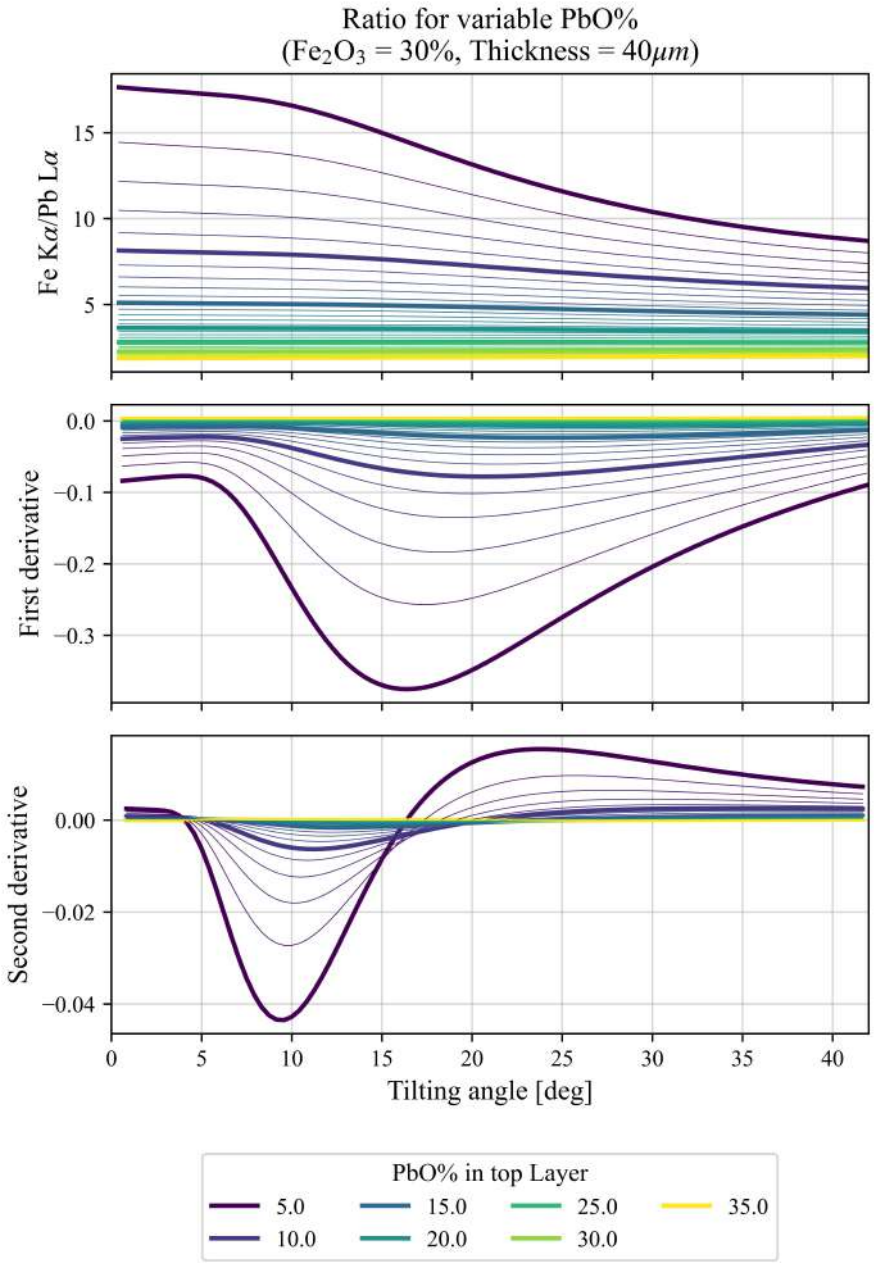

Figure 5.9: Intensity of iron and lead K_α and L_α fluorescence lines in function of the lead content, abundant in the bottom layer. On top the ratio profiles, in the centre plot its first derivative, on the bottom plot its second derivative

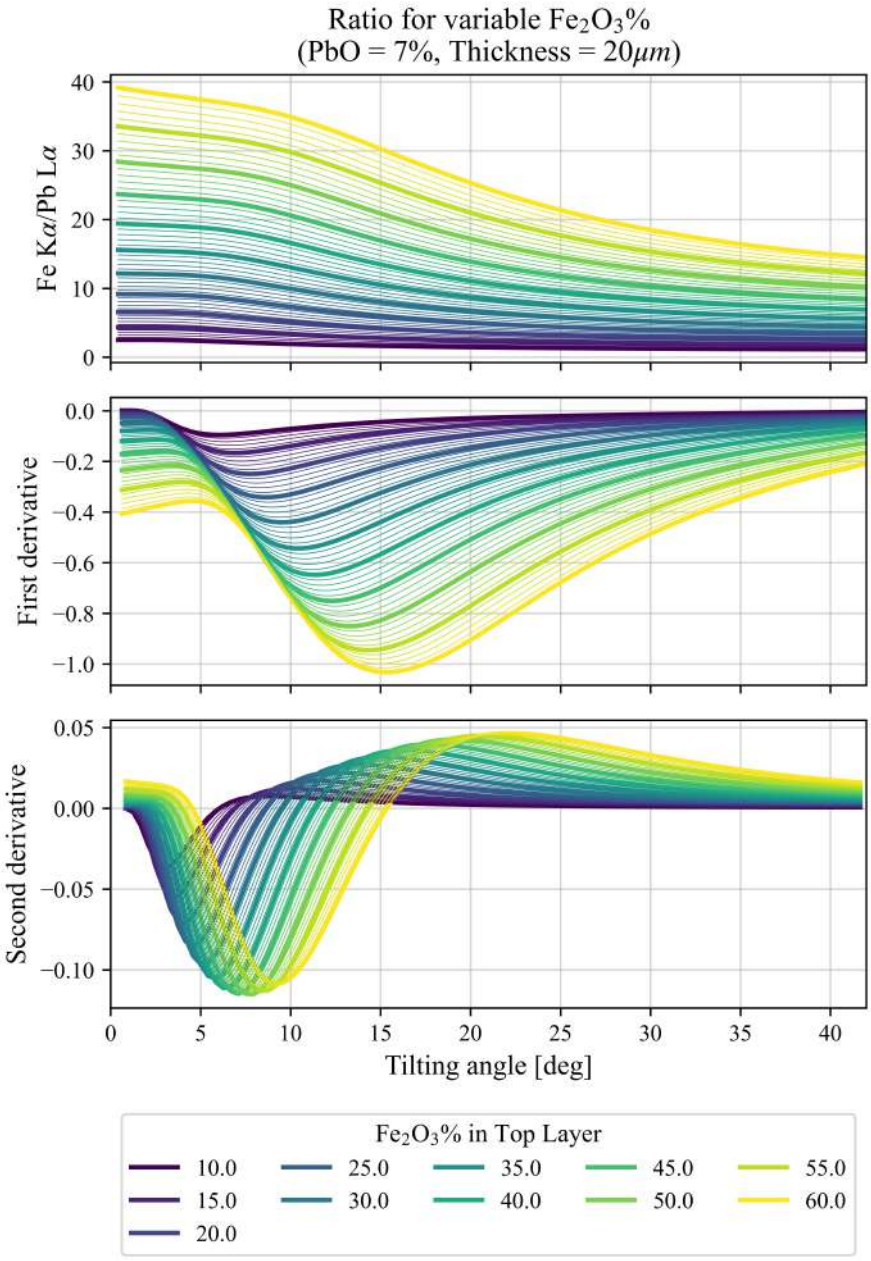

Figure 5.10: Intensity of iron and lead K_α and L_α fluorescence lines in function of the iron content, scarce in the bottom layer. On top the ratio profiles, in the centre plot its first derivative, on the bottom plot its second derivative

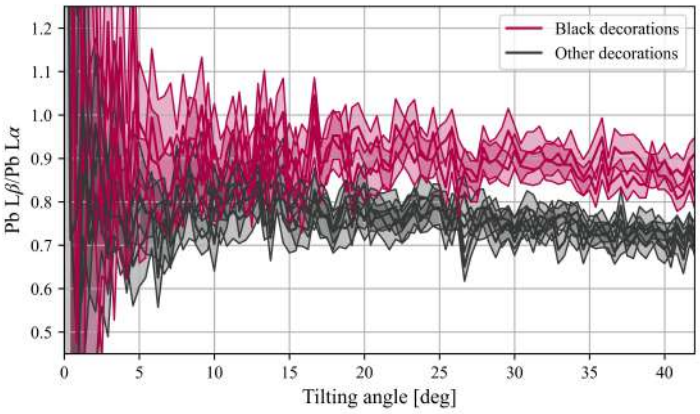

Figure 5.11: Experimental ratio between the lead L_β and L_α lines for the different decoration. Here is highlighted in pink the ratio calculated for the black decorations and in grey the one calculated for all the other decorations (white glaze, and the dark/light blue glaze)

5.5 RESULTS

5.5.1 Lead ratio

The main element, common to all the decorations (regardless the colour) is lead. So it can be useful to evaluate if the ratio of the two most intense fluorescence lines of lead (L_β/L_α) is always the same or if there is a difference, figure 5.11 This ratio has been calculated as weighted mean between the ratios obtained for each decoration.

If we look at the value of this profile, we can split the decorations into two groups: (I) the blue decorations and the white glaze, which present the same ratio; (II) the black decorations (independently by their thicknesses), which present a higher ratio. A higher ratio implies a lower intensity of the L_α line respect to the L_β line, as the latter is usually less attenuated (unless there is an absorption edge of an element between those two lines, like the K edge of Ge or As). We observe that this change can be possible only if a covering layer, with a lower lead content respect to the bulks is present, as even sensible changes in composition, like an increased content of iron, would not result in a sensible change in the lead ratio.

In the case of the blue spots, it seems that the attenuation does not change differently for the energies of the fluorescence lines of lead (10.55 keV for the L_α, 12.62 keV for the L_β). Indeed, even if arsenic is present in the blue decoration layer, it is at lower concentrations [28]. Between the white and the blue glazes, we do not expect a great difference in the matrix composition (but we could infer it also looking at the cumulative spectra shown figure 5.3).

We can also observe that the uncertainty is very high in the range 0° to 4°, as the intensity of the signal is very low: in general the lower

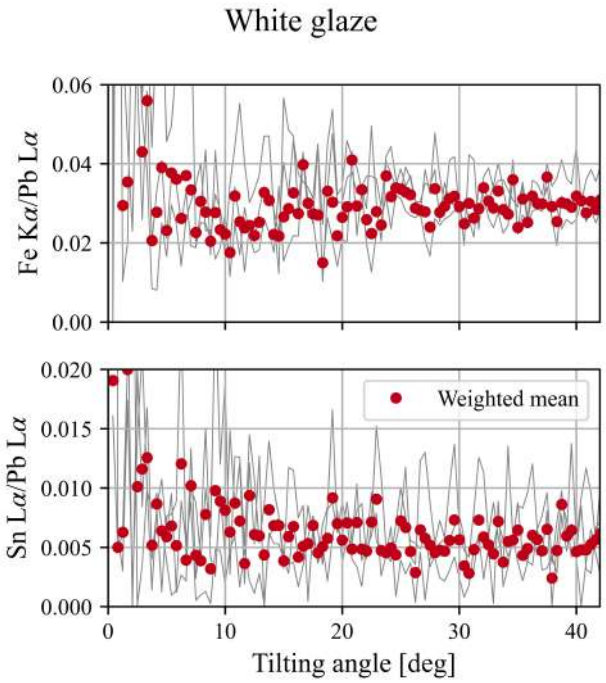

Figure 5.12: Intensity ratio evaluated for tin and iron in the white glaze measurement points, for both the ratios, the reference fluorescence line is lead L_α

is the angle, the lower is the signal, the higher is the error (even if each case must be considered separately).

5.5.2 White glaze and blue decorations

If we look at the ratio calculated for the white glazes, that we consider as a reference, figure 5.12, we see that the iron/lead ratio remains constant for the whole profile, while the tin ratio slightly decreases. We choose iron and tin as characterizing elements, because iron is the main element of the black decorations, thus a comparison may be useful, and the latter characterizes the glaze opacity. The behavior of these ratio is linear, like the one observed for bulk layers, see figure 5.7.

For the blue decorations, we analyzed the ratios of cobalt and iron, related with the blue color of the glaze. For the dark blue glaze all the spots present similar ratios, figure 5.13, thus can be averaged out, and we can observe that the ratio is linear, remaining constant for iron (0.1), and slightly increasing for cobalt (from 0.02 to 0.04).

If we look at the light blue decoration, we observe the same behavior for iron and cobalt, even if the intensity ratio is lower for both elements (iron 0.05, and cobalt is constant at 0.02), as expected for lower contents of the coloring oxide

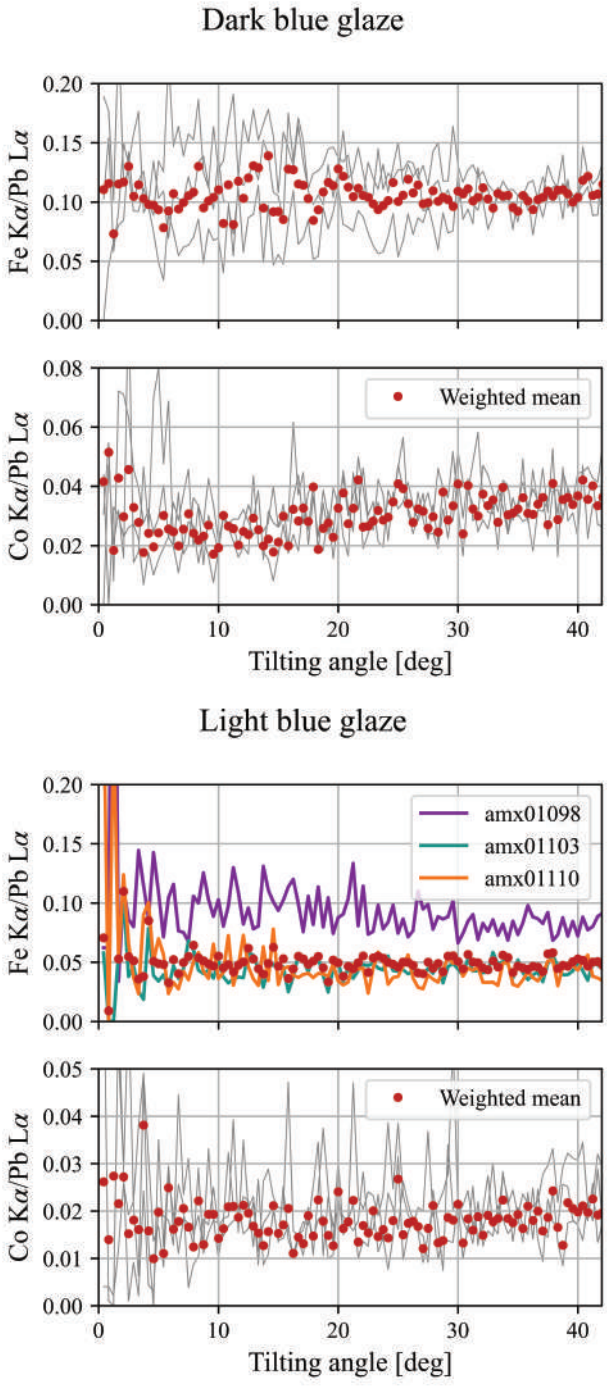

Figure 5.13: Intensity ratio evaluated for cobalt and iron in the blue glaze measurement points, for both the ratios, the reference fluorescence line is lead L_α. On top the data collected from the Dark blue glaze, on bottom those collected from the light blue glaze.

A note must be made for point 01098, collected in the light blue glaze, where the ratio of iron/lead is the same of the dark blue decoration. As the change in colour is given by the thickness of the decoration, we expect the dark blue decoration to be of infinite thickness for the considered energies, this will also explain the lead L_β/L_α ratio, which is the same of the white glaze. For the light blue decoration, we cannot exclude that we are registering signal from the underlying white glaze. Nevertheless, the ratio of iron and cobalt is halved, but has a similar behaviour of the blue dark glaze. This can suggest a penetration of the blue glaze inside of the white glaze, so that for thinner layers we also see a higher dilution of the chromophore elements, yet we are in regime of infinite thickness, thus we cannot distinguish the presence of different layers.

5.5.3 Black spots

As can be seen in figure 5.14, the ratio of Fe K_α and Pb L_α is higher for low angles and decreases for higher angles, while the ratio of Pb L_β/L_α is higher than the one calculated for the white glaze, fig. 5.11. This behavior is logical for the presence of two different layers: the black decoration (iron and lead-rich layer), and the white glaze, lead-rich layer; as seen in the calculation shown in figure 5.10.

The aim now is to evaluate whether is possible to retrieve a range for the composition and thickness of the top layer. The sample points present the same ratio for both iron and lead, thus they can be averaged out, and only the mean profile, which can be considered representative of the analyzed spot, is considered (indeed all the measured points are on the same decoration).

With the Fundamental Parameters we calculated the possible ratio for different top layers composition and thickness. As we were not be able to define the top layer minor and trace elements, we assumed it to be composed only of its main elements expressed as oxides: Fe_2O_3, PbO, SiO_2. The composition employed are:

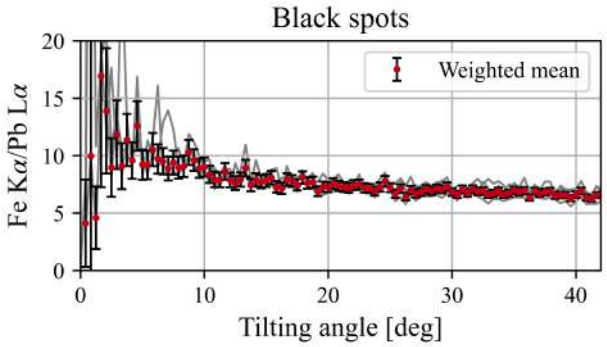

Figure 5.14: Fe K_α/ Pb L_α ratio for the Black spots sampling points.

- $Fe_2O_3\% \in [10, 60]$, step 1 %
- PbO% $\in [5, 35]$, step 1 %
- SiO_2 close the composition at 100 %

To define the thickness ranges we calculated the infinite thickness limit for Pb L_α and Fe K_α, considering the chosen compositional range, and shown in figure 5.15. This limit has been calculated considering the path-length that attenuates 99 % of the fluorescence radiation emitted by an hypothetical buried layer. As it can be seen, the maximum path-length is higher for lead, as the fluorescence energy is higher; or the lightest possible matrix it reaches a value of 500 µm, while for the heaviest composition it reaches a value of 100 µm; for iron it goes from 175 µm to 50 µm for the same conditions. Given these values we chose a range from 10 µm to 100 µm with a step of 1 µm, close to the infinite thickness limit for lead.

The comparison with the simulated and the measured profile has been made through the reduced χ^2-method [18], we considered acceptable all the compositional and thickness values that gave a profile for which the χ^2-test is $\leqslant 1.5$ for both the lead and iron/lead ratios.

The reduced χ^2 is calculated as:

$$\chi^2 = \frac{1}{d} \sum_i \frac{(y_m(i) - y_e(i))^2}{\sigma_m(i)} \tag{5.1}$$

where y_m is the measured value, y_e is the simulated value, σ_m is the uncertainty of the measured value and d are the degree of freedom, calculated as:

$$d = n - \nu \tag{5.2}$$

where n is the number of point and ν is the number of variables, here $n = 3$ (thickness, lead content, iron content).

In figure 5.16 you can see the variables that gives acceptable χ^2 values for the two ratios. The data are presented in a 3D plot, where on the axis are shown the iron and lead concentrations and the black-glaze thickness. In red-black hues are plotted the parameters' values that gives acceptable χ^2-values for Fe K_α / Pb L_α ratio, and in blue for the Pb L_β /L_α ratio; the darker is the color the lower is the χ^2-value.

In figure 5.17 the same data are projected on the three planes. In black are plotted the values and in black are plotted the intersection of the two regions, i.e., the values that return χ^2-value $\leqslant 1.5$ for both the ratios, and then that satisfies both the conditions. This plot is easier to read respect to the 3D-scatter plot, and looking at the ratio of the lead fluorescence lines, we observe that it divides the space into two regions, depending on the lead concentration, and that the accepted values lie in the region where the lead concentration is lower than the 15 %; for higher concentration of lead the amount of this element in

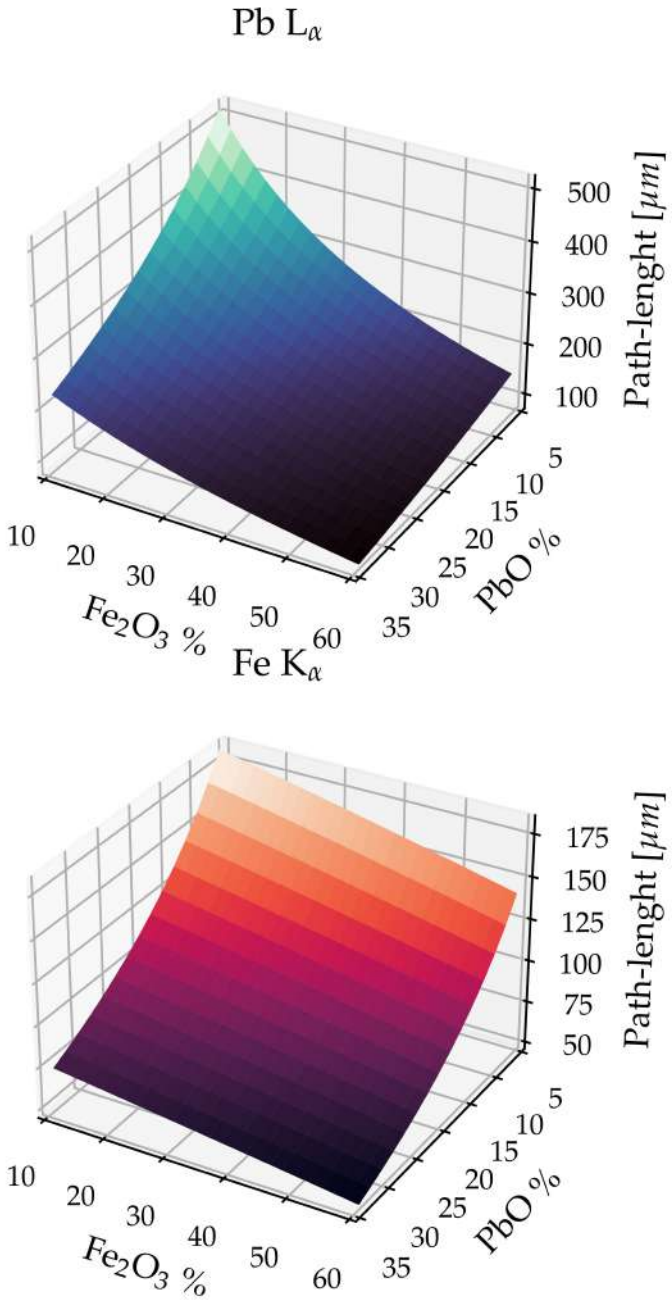

Figure 5.15: Maximum path-length crossed by the fluorescence radiation for a glaze of composition $(Fe_2O_3)_x : (PbO)_y : (SiO_2)_{100-x-y}$

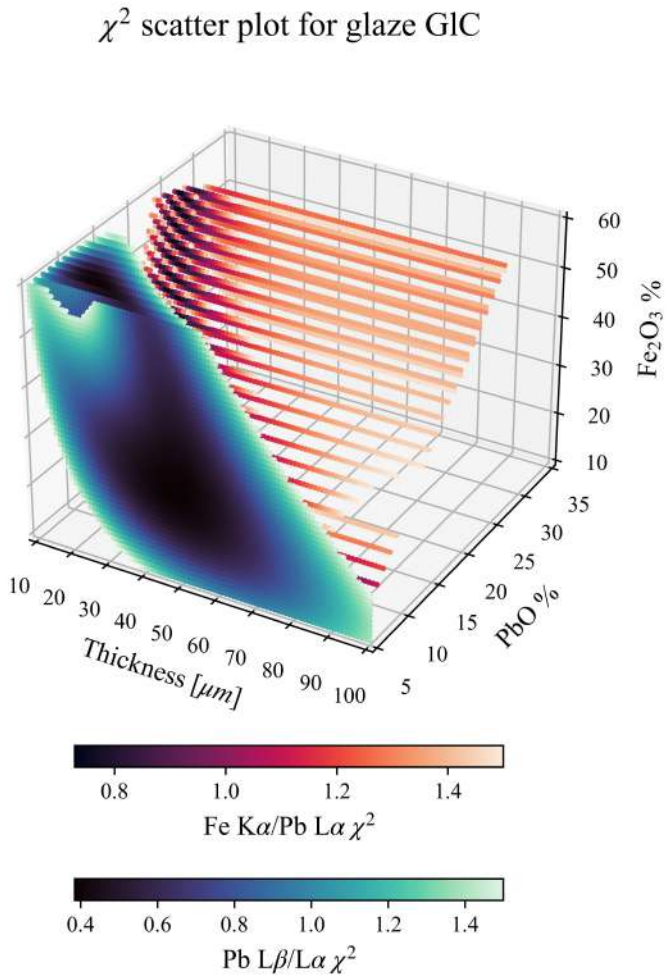

Figure 5.16: Parameters for which the FP-calculations return a profile with an acceptable χ^2-values ($\chi^2 \leqslant 1.5$) when compared with the ratio profiles. In black-red hues the point selected for having accepted χ^2-values for the Fe K_α/ Pb L_α ratio, in black-blue hues the ones have an accepted value for the Pb L_β /L_α. The darker is the color the lower is the χ^2-value.

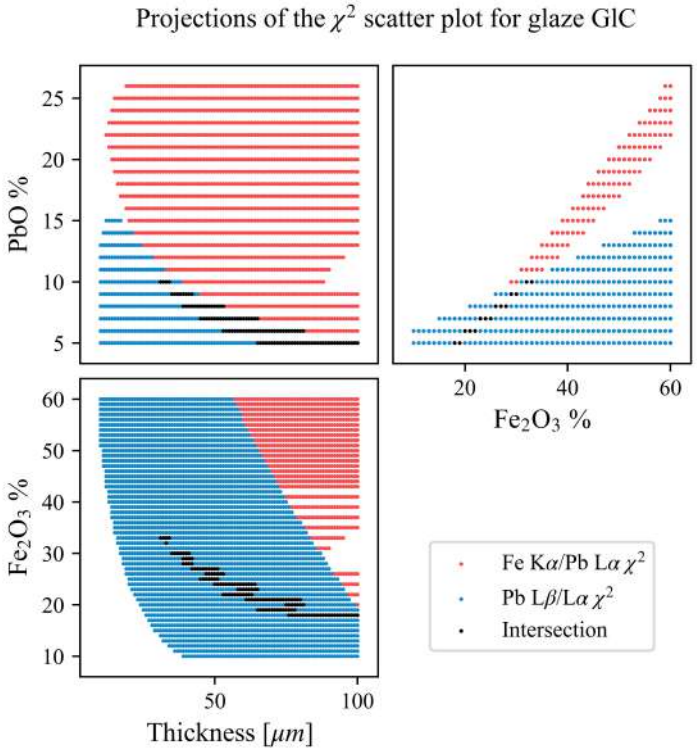

Figure 5.17: Projection of the scatter plot, in red the point selected for having an accepted χ^2 for the Fe K_α/ Pb L_α ratio, the blue ones have an accepted value for the Pb L_β/L_α; while the black are the interception.

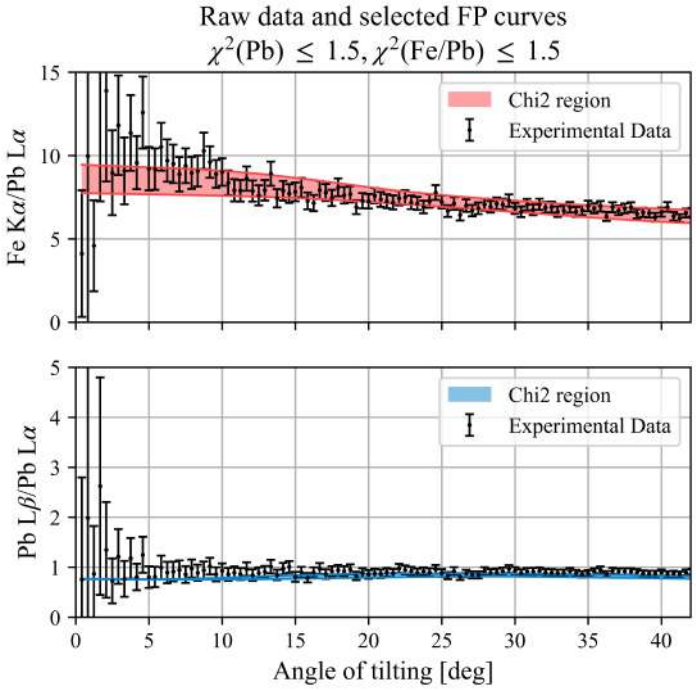

Figure 5.18: Profiles of the selected variables, the black data in the projection plot, compared with the experimental profiles. On top the χ^2 for the Fe K_α/ Pb L_α ratio, on bottom the Pb L_β/L_α.

the top layer becomes too high lowering the ratio's value, and shifting it toward those values observed for the white and the blue glaze. We can observe also that the concentration and thickness values that satisfy the conditions, black points in Figure 5.17, are found for a lead concentration lower than 10 %, a concentration of iron oxide between 18 % to 33 % and a black-glaze thickness higher than 31 µm. Looking at each projection, we can also observe that the thickness is negatively correlated with the amount of iron and lead, indeed, to keep the ratio constant an increase in the top layer thickness implies a reduction in the matrix density (as the attenuation is affected both by density and thickness). Finally, the amount of lead is positively correlated with the amount of iron; as to keep constant the iron/lead ratio, they must vary in the same way (either both increase or both decrease).

Finally we can see in figure 5.18 the resulting profiles, using the variables for which the χ^2-values is acceptable, plotted over the measured profile.

Evaluation of the influence of the white glaze composition

Even though we knew the composition of the white glaze, we decided to evaluate how the amount of lead in the background would have influenced the final results on the estimation of the black glaze. Thus we performed the same evaluation simulating glazes with a different

Table 5.2: Composition of the glazes employed to study the influence of the lead concentration in the background on the composition and thickness results of the covering black glaze. The original glaze of our sample is the one here called Glaze C. Glaze A and B are taken from the work of Padilla et al. [48], while Glaze D and E are taken from the work of Iñañez et al. [28].

Oxide	Glaze					
	A	**B**	**C**	**D**	**E**	**F**
Na_2O	4.50	2.30	4.30	3.70	3.00	4.30
MgO	0.45	0.20	0.23	0.70	0.40	0.23
Al_2O_3	10.30	9.50	9.70	11.10	10.00	9.70
SiO_2	53.90	55.00	54.10	47.10	44.10	54.10
K_2O	3.50	3.70	3.08	2.20	2.10	3.08
CaO	0.78	1.70	1.20	0.70	2.00	1.20
Fe_2O_3	0.78	0.60	0.76	0.60	0.60	0.76
SnO_2	8.30	4.50	3.50	2.80	1.40	3.50
PbO	17.60	22.60	26.00	30.80	36.00	40.00

concentration of lead oxide, some of them were taken from analysis of other Puebla ceramic samples that are published in literature, [28, 48]. The composition employed for this studied are reported in table 5.2, as you can see the lead oxide content ranges from a minimum of 17.60 % in glaze A to a maximum of 40 % in glaze F.

For each glaze we treated the data in the exact same way we did for the real glaze composition, and the results are summarized in appendix C. To better compare the variation of the black spots structure depending on the white glaze composition, we plotted the distributions of intersection of the scatter plots (black spots in figure 5.17). Each scatter plot has been obtained changing the white glaze composition according to table 5.2, and the distributions for each variable are plotted in the violin plots depicted in figure 5.19. In those plots the x-axis represent the glaze composition, the y-axis the variable value, while the width of the violin plot represents the amount of data showing a particular value (i. e.it is the statistical distribution of the data). As you can see the lead maximum concentration in the top layer increases with the increasing of the lead concentration in the glaze, the same happens for iron, as expected being them positively correlated (see figure 5.17). If we look just at the maximum and minimum values, we see that for lead the possible concentration goes from < 7 % for glaze A, to < 12.5 % for glaze F, while for iron the maximum lead concentration has a much wider range, from 25 % to 40 %. Note that the minimum values do not change. The density of data is however skewed toward the low concentration elements range, which means

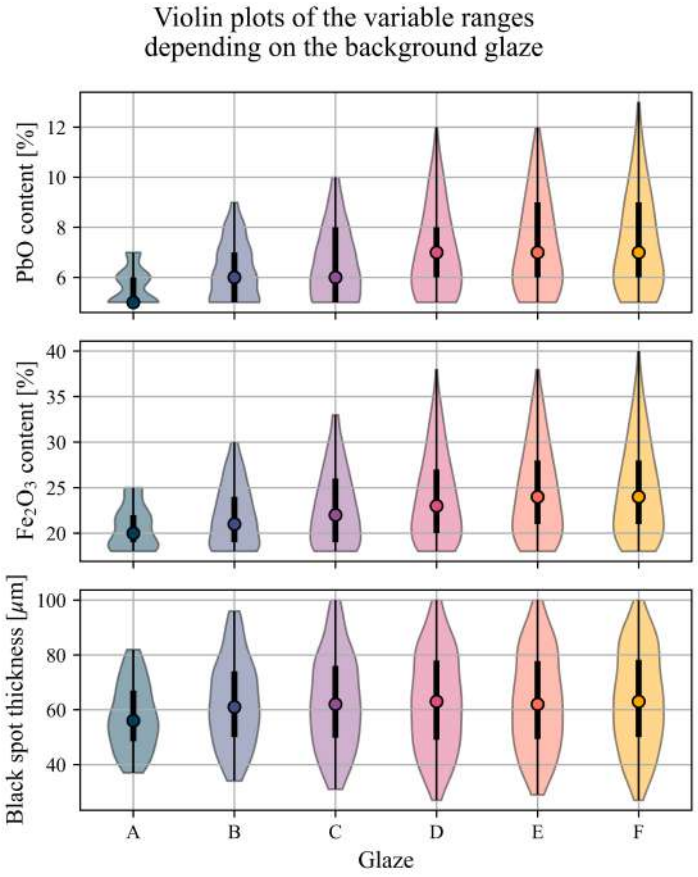

Figure 5.19: Summary of the ranges of composition and thickness for the different background glaze composition. The circles represent the median value, the thick line the interquartile range, while the thin line the total range; the area represent the distribution for each variable.

that more profiles generated with low elemental concentration are similar to the measured one. Intuitively, to maintain the same Fe/Pb intensity ratio, if the lead in the bottom layer is increased, iron concentration should also increase in the top layer, and to maintain the same lead L_α/L_β ratio also the lead in the top layer must increase. We can finally observe that for a lead concentration higher than 26 % in the glaze (Glaze C) the possible thickness of the black glaze is higher than 100 µm.

5.5.4 Black stripes

The black stripes decorations show a different behavior with respect to the black spots, as shown in figure 5.20. Firstly, we can observe that for the Fe/Pb ratio the sample points show different profiles, thus we cannot average out the results, as they will not be representative.

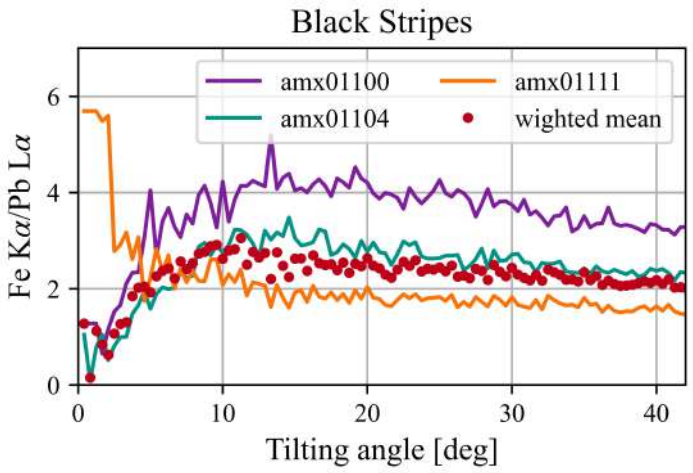

Figure 5.20: Fe K_α / Pb L_α intensity ratio of the black stripes decorations. As can be observed the lead ratio is the same for the different sample points, while the iron/lead ratio is different.

For this very reason we chose to treat separately these measures, comparing each one with the calculated data. The second feature we observe is that the iron profile is sensitively different respect those observed for bilayer samples, in this case the profile increases for the first 10°, than it decreases steadily. That is why here we assumed the presence of a trilayer system, where there is a first layer with low iron content, a second layer with high iron content (black decoration) and then the white glaze underneath.

The difference in the profiles can be given by two factors: different composition of the black glaze in the three spots or by a different thickness of the black glaze. During the production process is unlikely that the painter uses different pigments in different regions of the ceramic to create the same decoration; on the contrary, is more probable that a difference in the glaze thickness is responsible for this profile difference, as it is given only by the amount of material placed on the decoration, or by the fact that the covering low-iron content layer has different thicknesses. Besides, no information of the covering low-iron content glaze is known (nor its thickness nor its composition), thus we have to consider all the possibilities.

For this reason, we considered three different cases, observing how they affected the possible ranges of composition and of thickness of the black stripe decorations. In this case we do not expect to infer which case describes the layer system, as too many variables are involved; besides, if a different combination result in the same AR-XRF profile they can be equally accepted. The expectation is then to observe if despite the composition and thickness of the low-iron content covering glaze is possible to obtain any information on the composition or thickness of the black glaze.

Then we consider three different cases:

1. the black glaze during the firing process has been covered by a thin layer of the white glaze;
2. the black glaze during the firing process has undergone a process similar to that occurring in the lustre preparation, i. e.ionic exchange, thus the top layer is made of silicon oxide;
3. a reaction process has left a top layer with a lead content in between the background glaze content and the silicon oxide content.

For the first case, we simulated a sample made of: white glaze, black glaze, white glaze; for the second case a sample made of SiO_2, black glaze and white glaze; for the third case a sample made of white glaze (with a lead concentration of 10 %), black glaze, white glaze. The top layer was simulated with a thickness of 0.1 µm to 20 µm with a step of 0.2 µm; the black layer has been simulated with a thickness ranging from 14 µm to 110 µm with a step of 2 µm. The concentration of iron and lead in the black layer were changed within the following ranges:

- $PbO\% \in [0, 35]$
- $Fe_2O_3\% \in [5, 30]$

both with a step of 0.5 %.

Each sample point has then been compared with all the simulated data to find the best match, obtaining different χ^2-scatter plots and projection plots, one for each simulated black layer thickness. Also in this case we considered to have found a good match to all the data that gave a reduced $\chi^2 \leqslant 1.5$ was obtained for both the iron/lead and lead/lead ratios.

To reduce the number of data we also have to consider that the composition of the black glaze is the same for each sampling point, thus that the difference in the profiles is due to a different thickness of the black decoration, or a different thickness in the top glaze. Thus we have to find which compositions are common to all the all the measured spots, without taking into account the the black spots or the top glaze related thickness. Thus for each point we collapse the 4D-space (top glaze thickness, black glaze thickness, PbO%, Fe_2O_3%) into the PbO-Fe_2O_3 plane. Each measured point is then related to a region on this plane describing all the possible compositions that can provide the right information of the sample structure (when related to the respective thicknesses), figures 5.21 and 5.22. As the three stripes are supposed to have the same composition, the expected concentration of PbO and Fe_2O_3 are those found in the intersection of the contoured regions (purple area), which are common for all the measured spot.

Found the possible composition of the black glaze from the intersection of the selected areas of the compositional plane (purple areas),

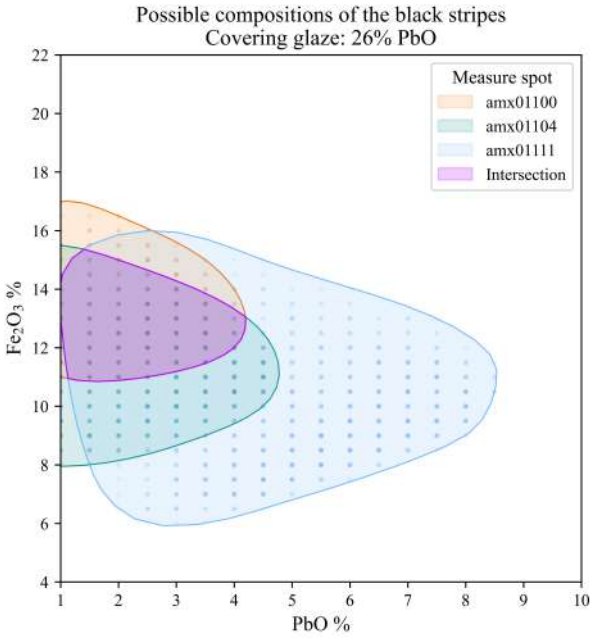

Figure 5.21: Region of composition of the three sample points taken on the black stripes, for each colour is shown the compositional range of one sample point, the intersection, in purple, represent the supposed composition of the black glaze for a covering layer with a lead content of 26 %

we could find what thicknesses of the black layer and of the top layer corresponded to those composition.

The variable distributions of the three considered cases are summarized in figure 5.23, were we have plotted the distributions of the acceptable values for each parameter. These violin plots have been created in the same way of the plots shown in figure 5.19.

In the first two plots we observe the compositional ranges obtained for each case, and they are indeed affected by the composition of the low iron covering glaze, which is unknown. Thus, no reliable information can be inferred besides a low lead content (lower than 6 %) and a content of iron between 7 % and 17.5 %.

What can be observed instead is that the thickness of the black glaze is not affected by the composition of the covering glaze, as each measurement point shows nearly the same thickness range. Sample amx01100 is the thickest layer, and its maximum thickness is higher than 110 µm, in this case the real median value is higher than the one calculated, as also simulations with thicker value would have been considered as acceptable. Sample point amx01104 has a thickness of nearly 50 µm, with an overall range spanning from 20 µm to 80 µm, while sample point amx01111 seems to be the thinnest with a range between 14 µm and 47 µm.

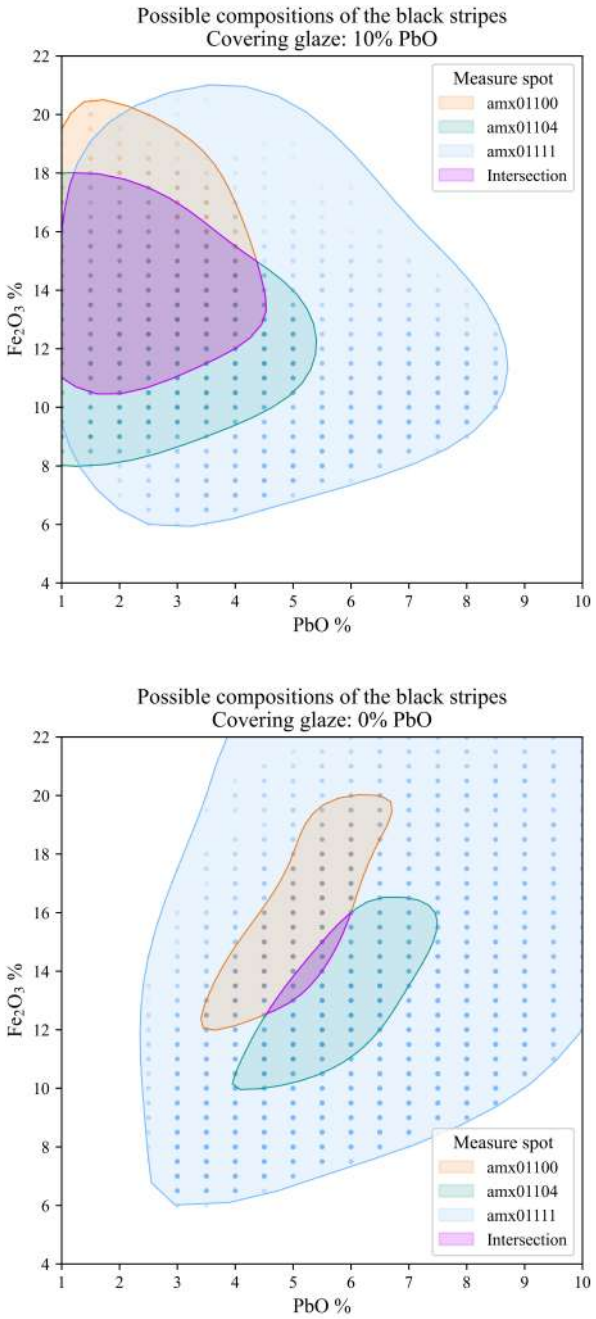

Figure 5.22: Region of composition of the three sample points taken on the black stripes, for each colour is shown the compositional range of one sample point, the intersection, in purple, represent the supposed composition of the black glaze for a covering layer with a lead content of 10 %, top figure, and SiO_2 bottom figure.

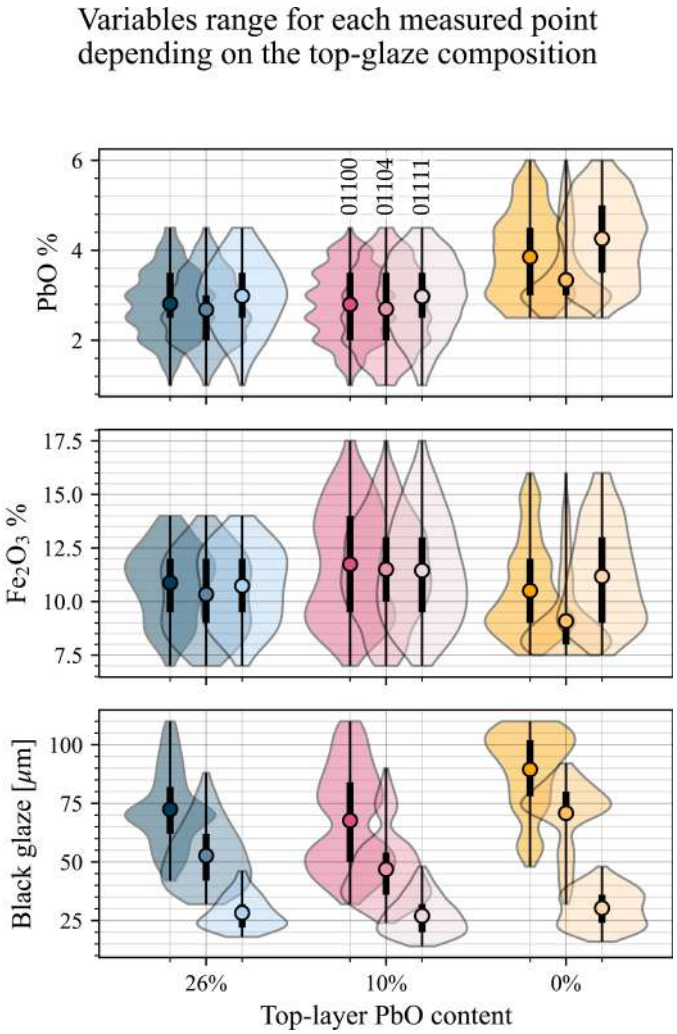

Figure 5.23: Violin plots representing the distribution of the variables and the selected compositional and thicknesses ranges. Each colour (blue, yellow and pink) corresponds to a different composition of the covering top-glaze, each hue instead, represents one of the measured sample spots. The dots represent the median value for each parameter, the thick line the interquartile range, and the thin line the total range of distribution.

6 ANALYSIS OF THE LUSTER CERAMIC

A recurring problem in the analysis of the stratified Cultural Heritage materials is the need to produce thin sections of such materials, or to analyze fractures and sherd. Thus complete, unfractured, artifacts are inaccessible to the stratigraphic study, unless we apply accelerated particle techniques, like RBS, that however requires the access to accelerators. Instead techniques like all the angle dependant XRF techniques can be employed also in a laboratory system, are cheaper to develop, and will increase the amount of samples that can be studied. After having assessed the applicability, the reliability and the limits of these techniques in well-known samples, we can then apply them for studying unknown artifacts.

In the last part of the investigation, we the proceeded to apply not only AR-XRF but also GE-XRF and GI-XRF for the analysis of nanostructures in the field of Cultural Heritage. For this reason we have analyzed a sample of luster ceramic originating from Casteldurante, a Renaissance center of luster production in the central Italy [44, 46]. This sample has been thoroughly studied, thus many information on the structure and composition are already available.

The measurements have been performed at the XRF beamline of the Elettra Synchrotron, Trieste, Italy. As it has been the first time that these kind of sample have been investigated by means of GI-XRF and GE-XRF the measurements of the luster sample have been preceded by the measure of a standard sample, used as a reference for the alignment protocol and for the data analysis. Then, applying the same analytical protocol of the reference, we proceeded analyzing the lusterware shred.

6.1 LUSTER TECHNOLOGY: NANOPARTICLES AND NANOLAYERS

Lustered ceramic is precious type of pottery characterized by the presence of a decorative metal-like film applied on the surface (figure 6.1, and is the first production to employ (unknowingly) nanostructures for their optical properties [19, 27, 58, 61].

Figure 6.1: Example of a lustered sherd, the two pictures are taken at a different angle with the same light. On right the color of the glaze and of the luster layer without the metallic shine, on right the ruby red colour of the metallic shine of luster.

6.1.1 A brief history of luster pottery

Luster technology has a long and complex story, and has followed the rising and fall of many dynasties; indeed, the complex technology suggests that instead of the spread of luster production thanks to a copying process, the shift of the production centers was due to the migration of the potters and for direct transmission.

Firstly luster was employed in Syria and Egypt to decorate glass objects, the first manufacture dates back to the end of the VII cent. CE, during the Islamic domination [16].

The production of luster decorated glazes, on the other hand, began in Iraq, during the Abbasid period (750 – 1258 CE.): the first artifacts dates back to the half of the VII cent. CE., and the Iraqi production seems to continue until the end of the X cent. CE. It is probable, then, that due to the fracture of the Abbasid caliphate, potters moved to Egypt, where in the Fatimid period (909 – 1171 CE.) the new center of production of lusterware arises.

The Egyptian production ended with the take over of the country by Saladin and the beginning of the Ayyubid dynasty (1171—1260 CE.), when it moved to Iran (Kashan) [57]. Even though Egypt had been the center of production for nearly two hundreds years, during the Fatimid period, the technology of lusterware started to spread all over the Islamic territories. New production sites has been found indeed in Tunisia [79] and Spain (Al-Andalus); the latter giving rise to the Hispano-Moresque production (XIII-XIV cent.), that quickly spread all over Europe.

Then, during the XVI cent., in the cities of Gubbio and Deruta (center of Italy), a new important center of production was estabilished, here

the red ruby luster was reintroduced along with the characteristic local yellow golden luster [15, 44, 45].

6.1.2 The production technology

The main characteristic of the lusterware structure is the presence of a complex stratigraphy that requires a high technological production process. What defines the luster is the metallic nanoparticle layer (usually composed of copper or silver naoclusters) dispersed in a glassy matrix. This layer is placed below a glass-like surface and above a white or coloured opacified glaze, and adds a shiny and iridescent appearance to the ceramic glaze. To achieve this results the luster production requires two different firing process: the first one stabilizes the glaze, and the second one creates the luster layer. Indeed, after the pottery has been fired for the first time, the luster painting is applied on top of it; then the excess is removed after the firing, uncovering the iridescent decoration.

The luster paint is composed of finely ground copper and silver salts, mixed with sulphur compounds (like cinnabar, copper or iron sulphides or sulphates...), clay or an organic medium and an acidic solution, like vinegar or citrus juice, added to avoid flocculation. During the second firing the metal salts react with the sulfur compounds, forming copper and silver sulphates and sulphides, which then react with the underlying glaze, in a process called ionic exchange. The sulfur works as a carrier for the ion exchange process in which silver (Ag^+) and copper ions (Cu^+ and Cu^{2+}) [50] penetrate into the glaze, substituting potassium and sodium ions (Na^+ and K^+).

Some authors [19, 40] performed different attempts to produce lusters following the medieval recipes, and discovered that an important requirements to produce the lustered ceramics lays in the glaze composition, the firing temperature and the firing atmosphere. The ion exchange process alone does not imply the development of a iridescent layer, as copper and silver nanoparticles must be in their metallic form (reduced) to achieve this optical feature. The firing process thus must be well controlled: the luster formation takes place at 550 °C, at first, in neutral/oxidizing atmosphere to allow the migration of copper and silver inside the glassy matrix, then, in reducing atmosphere to reduce copper and silver ions in their metallic form. After the nucleation process, the growth of the nanoparticles slows and then stops their penetration inside the glaze, producing the characteristic superficial thin layer. As this process takes place at relatively low temperatures, the underlying glaze must soften easily, that is why the presence of lead into the glaze is of the utmost importance; besides, the presence of the Pb^{2+} ions reduces the ionic mobility of silver and copper ions, allowing the formation of nanolayers just below the surface.

Table 6.1: Parameters describing the reference samples from the XRR and GI-XRF analyses of Karydas et al. [32]

Composition	Thickness [nm]	Density [g/cm^2]	Roughness [nm]
Fe_2O_3	3.9 ± 0.7	4.25 ± 0.30	0.5 ± 0.1
Fe	23.7 ± 0.7	6.8 ± 0.2	0.7 ± 0.2
SiO_2	7.5 ± 2.5	1.6 ± 0.2	-

The use of non-destructive techniques, like RBS [47, 56] has been employed to infer the layer composition of the lusterware, showing:

- the presence of a first layer is made of a lead-free and silica-rich glassy matrix whose thickness is in a range from 10 to 300 nm, on the surface no metal nanoparticles are formed;
- one or more luster luster layers, 30 to 200 nm thick each, depleted in alkali and lead (due to the ionic exchange process), which may show a compositional gradient.

6.2 ANALYSIS OF STANDARD SAMPLE

The reference sample analyzed is a silicon disk covered by a nanolayer of iron, with the nominal thickness of 24 nm. This samples has been previously measured by Karydas et al. [32] whose results are summarized in table 6.1.

Due to oxidation processes, however, we do not expect to obtain the same exact results, indeed the oxidation layer may have thickened since the last time the sample has been analyzed.

The measurements with both GE-XRF and GI-XRF has given precious information on the efficiency of each technique, and the count-rate expected, and as a consequence an idea on the measurement time required for the luster sample analysis.

6.2.1 GI-XRF analysis

The analysis of GI-XRF on the reference sample has been performed with a source energy of 10.5 keV employing the Si (111) crystals monochromator; the slits of the beam have been opened into a rectangle of area $200 \times 100\mu m$. The sample has been irradiated along an angular scanning from $-0.2°$ to $2.5°$, with a step of $0.005°$ (for a total collection of 541 spectra), with a dwell time of 30 s.

The detector (Bruker, see section 3.2 for the specifications) has been placed at a distance of 10 mm from the sample surface.

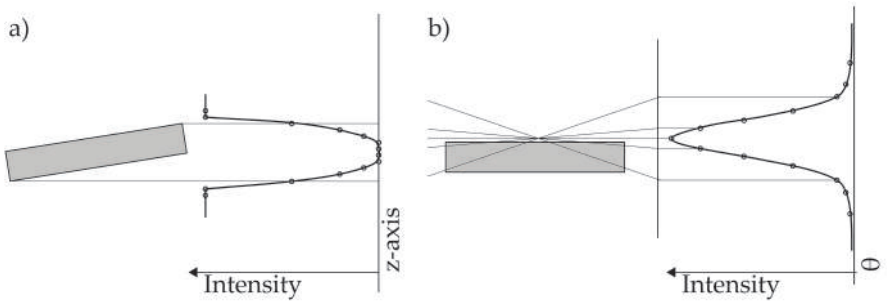

Figure 6.2: Intensity of the source signal during the alignment process; (a) when moving the z-axis, (b) when rotating the sample along the θ axis.

Prior to measure the sample, we performed the alignment to ensure that the sample surface was parallel to the source. The alignment process is divided into 4 steps. Placing the detector in front of the sample, and tilting the sample of few degrees with respect to the source:

- Scanning the x-axis to center vertically the sample,
- Scanning the y-axis to center horizontally the sample.

The center is the peak of the Gaussian distribution of the fluorescence signal of one of the elements of interest (in this case iron, or silicon). Note that for the Elettra manipulator x and y axis are inverted, the former is the horizontal axis, and the latter is the vertical.

Placing the diode on the opposite side respect to the source, measure the source intensity, and:

- scan along the z-axis,
- rotate the sample.

Moving the sample along the z-axis (figure 6.2a) allows to measure the length of the shadow of the sample over the diode, as soon as the signal intensity drops the beam is being covered by the sample; thus, if the sample surface is parallel to the beam, the sample is aligned. When aligned with the z-axis, the rotation of the sample will cause an increase or a decrease of the shadow over the detector (figure 6.2b). If the beam reaches completely the detector the sample is out of focus (the beam does not hit the sample surface), while if the signal is too low, the sample is not parallel or is blocked by the lateral surface of the sample. To be well-aligned, when the sample is parallel to the beam, it should halve the beam intensity. Iterating this process multiple times the sample is aligned with the direction of the beam.

The data of the reference sample are plotted in figure 6.3, where you can see the iron and silicon data, their first and second derivative. The second derivative is employed to retrieve the critical angle of total

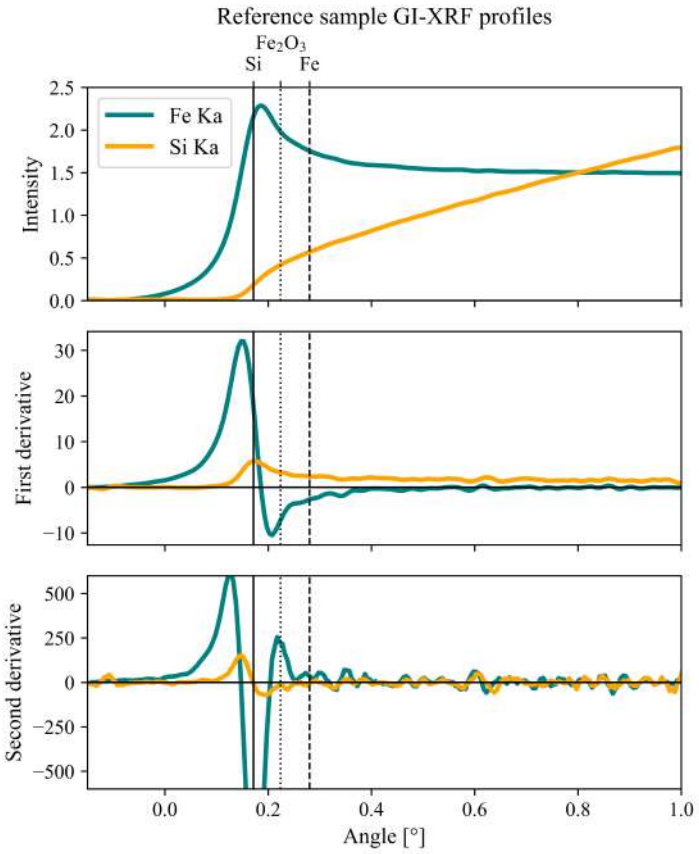

Figure 6.3: GI-XRF profile of iron and silicon of the reference sample, on top the intensity, normalized for the iron K_α plateau; in the middle the first derivative and in the lower plot the second derivative. The vertical lines represent the critical angles calculated for the source energy, respectively for Si, Fe_2O_3 and Fe, employing the density values of table 6.1

reflection which is in the inflection point of the grazing profile. As you can see the zero of the second derivative of iron, the sample is misaligned respect to the critical angle both of iron and iron oxide, with an error of approximately 0.13°. Indeed, the profile of iron rises at lower angles respect to both the calculated critical angles, which is physically not possible.

6.2.2 GE-XRF analysis

On the other hand, GE-XRF measurements have been performed with a source energy of 7.2 keV, using the multilayer monochromator to enhance the source intensity, with an irradiated area of $100 \times 100\mu m$. The energy employed has been chosen to better excite iron. Angular range employed is the same of the GI-XRF measurement: 0° to 1.2°, with a step of 0.01°; but this time the dwell time is of 60 s.

An Amptek detector was employed, placed at a fixed distance of 146 mm. The angular resolution of the detector, which is collimated with a slit with an opening of 200 µm and is 300 µm thick, is of 1.4 mrad (or 0.08°).

The GE-XRF data are plotted in figure 6.4, also in this plot we can observe the misalignment of the data, this time however the signal rises after the calculated critical angle.

As the sample is aligned only during the grazing incidence measurement, a rotation of the sample of 90° causes the misalignment to effect the data on the opposite direction, and the signal seems to rises after the critical angle.

6.2.3 Simulations of the data

Due to the alignment problems, that may also be caused by a non perfect flatness of the sample surface, we tried to evaluate if it is possible to perform an angular correction after the acquisition, during the data analysis process.

To perform this task we employed a simulation and fitting code (courteously supplied by dr. Andreas Karydas from the NCRS Demokritos, Athens). We then simulated the possible GI-XRF profiles that are obtained analysing an iron nanolayer over silicon. The parameters changed are the iron layer thickness, the iron density, the thickness of the oxidation layer taking into account the oxidation process (i. e. part of the mass is converted from metallic iron to iron oxide). For each case we calculated the value of the critical angle of total reflection (for silicon, iron and iron oxide), and we retrieved the position of the inflection point of the GI-XRF profiles. The simulated profiles are plotted in figures 6.5 and 6.6. In the left columns there are the profiles of iron, while in the right one the profiles of silicon.

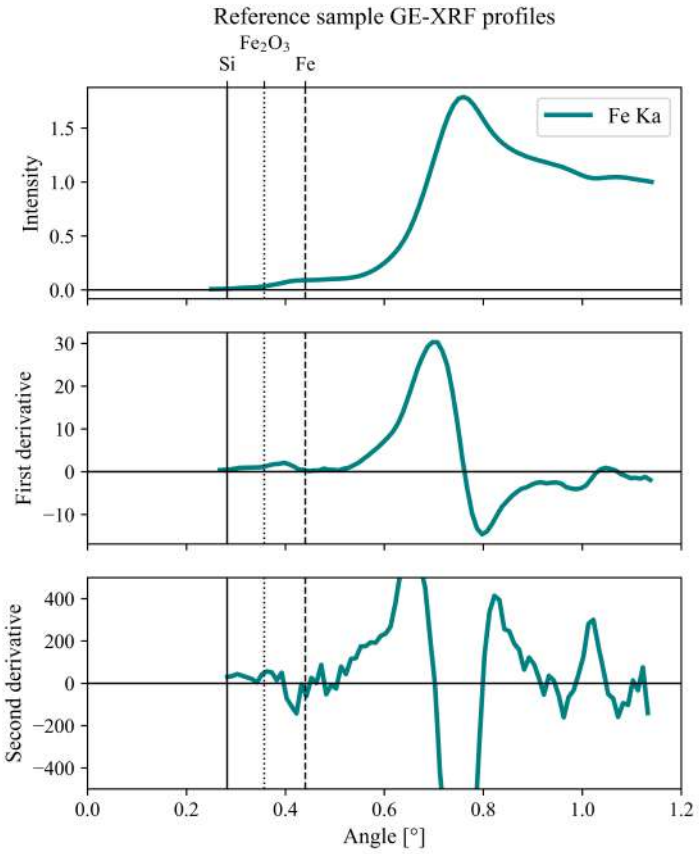

Figure 6.4: GE-XRF profile of iron f the reference sample, on top the intensity, normalized for the iron K_α plateau; in the middle the first derivative and in the lower plot the second derivative. The vertical lines represent the critical angles calculated for the iron fluorescence energy, respectively for Si, Fe_2O_3 and Fe, employing the density values of table 6.1

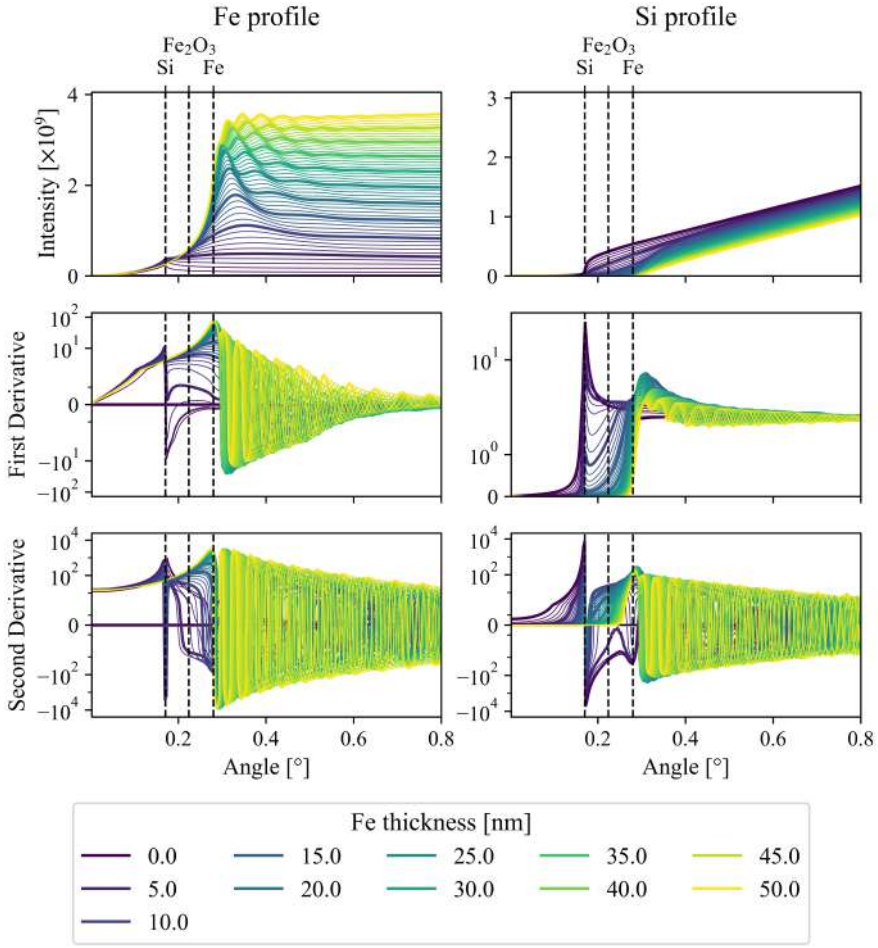

Figure 6.5: GI-XRF profiles of iron and silicon in the case of a bilayer system, in which a nanolayer of iron covers a bulk of silicon. On left the profiles of iron, on right those of silicon. The vertical lines represent the values of the critical angles of silicon, iron oxide and iron.

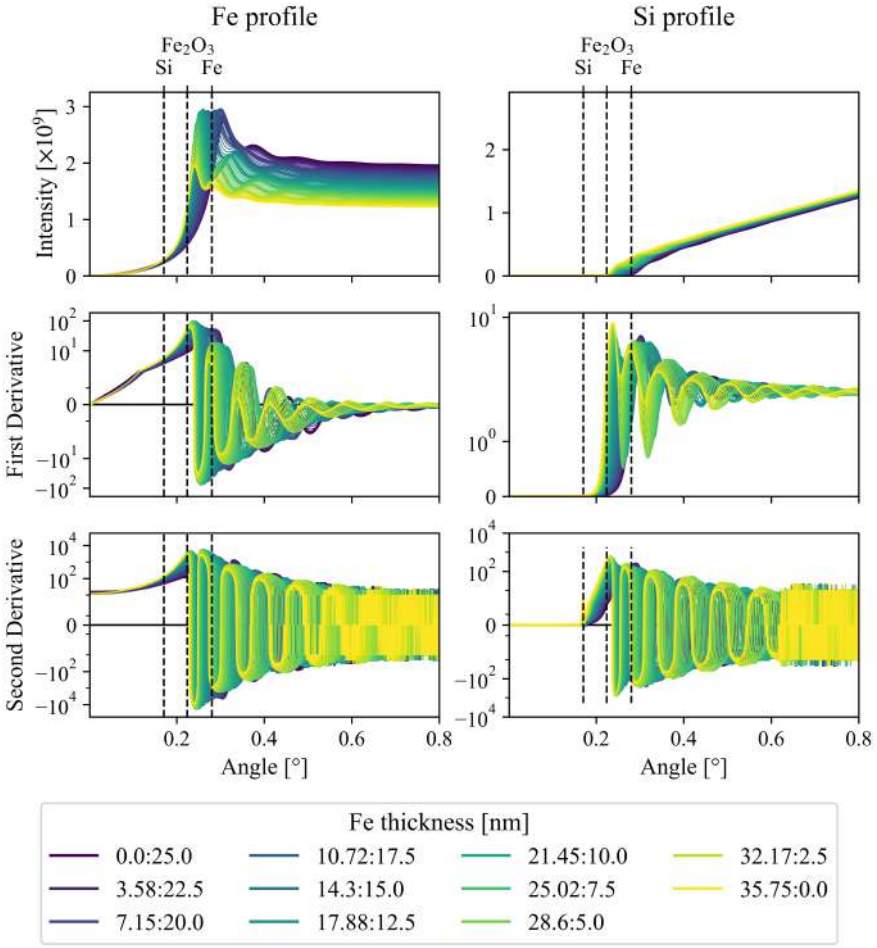

Figure 6.6: GI-XRF profiles of iron and silicon in the case of a three-layer system, in which a a bulk of silicon is covered by a nanolayer of iron which is oxidized as the time passes by. On left the profiles of iron, on right those of silicon. The vertical lines represent the values of the critical angles of silicon, iron oxide and iron.

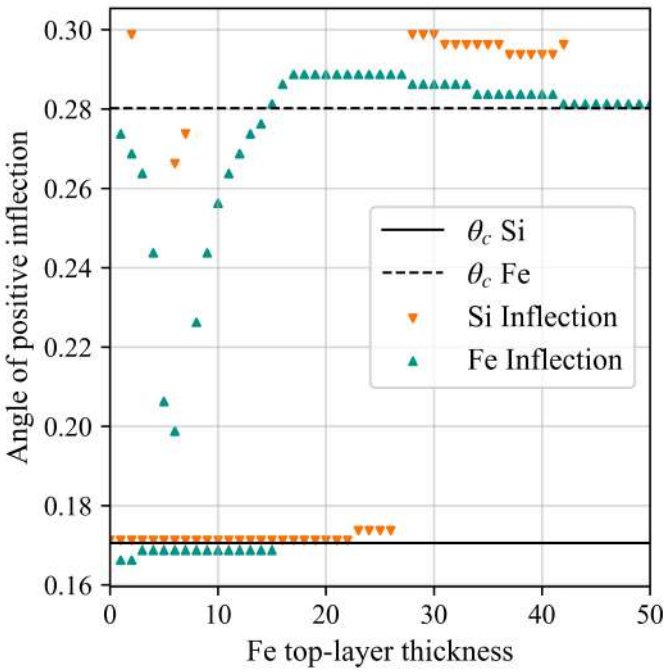

Figure 6.7: Inflection point for the bilayer case of iron over silicon, in orange the inflection point of silicon, in green those of the iron profiles.

The profiles shown in figure 6.5 refers to a bilayer of iron and silicon, where the thickness of iron is changed, and is possible to see that the profiles shift toward greater angles as the iron nanolayer thickness increases, until the inflection point stabilizes at the critical angle of iron.

Those plotted in figure 6.6 show a GI-XRF profiles for a three-layers system composed of Fe_2O_3, Fe and Si. In this case we simulated how the oxidation process affects the grazing profile, i. e., in each step we have a thin layer of iron that is converted in iron oxide, changing composition, density and thickness of the top layer, and reducing the thickness of the second layer As the iron mass is preserved, for these profiles we start from a case in which silicon is covered by a 25 nm layer of iron, and we reach a case in which silicon is covered by a 35.75 nm of iron oxide. The inflection points thus shift from the critical angle of iron to the one of iron oxide.

Finally in figures 6.7 and 6.8 the inflection points values in function of the thickness or composition of the covering layer are plotted.

As you can see the iron inflection point, in the case of the bilayer system in which no oxidation takes place, moves from the critical angle of silicon in the case of a layer less than 10 nm thick to the critical angle of iron for thicker values. Instead, when the oxidation process takes place the inflection point moves from the critical angle of iron toward the critical angle of iron oxide.

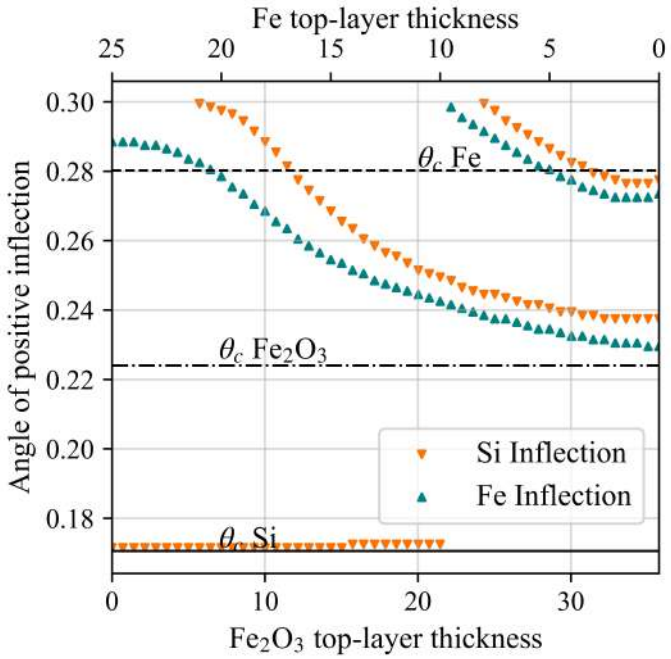

Figure 6.8: Inflection point for the bilayer case of iron over silicon, as the oxidation process takes place, in orange the inflection point of silicon, in green those of the iron profiles.

For this very reason a correction of the x-axis after the measurement has been performed is impossible, indeed the composition of the sample (even of the oxidation process occurring on the sample) must be well-known, which is a paradox.

6.3 ANALYSIS OF THE LUSTER SAMPLE

As the alignment of the reference sample is not reliable we will discuss here the results of the measurements of the luster sample only in a qualitative way.

The sherd here analyzed is a luster fragment decorated with simple and geometrical motifs (figure 6.9) and showing gold lustre, coming from the Italian Renaissance productions. It is part of a set of samples coming from dishes, basins, plates or bowls that have already been analysed with micro-destructive, invasive and non-invasive techniques [44–46] and have also been dated by thermoluminescence [24, 25]. Thanks to data supplied in the cited literature we already know the sample composition and thus we can verify if the application of Grazing techniques can be applied also in the analysis of CH samples.

A lead-tin alkali glaze is employed as white decoration, the presence of lead is important to lower the melting/softening temperature of the paint, while tin oxides are employed as opacifiers, as they aggregate

Figure 6.9: Sample analyzed at the XRF line of the Elettra synchrotron, the lustered part investigated is the central golden stripe.

into small crystals of cassiterite (SnO_2) that disperse light inside the matrix. The range of composition of the white glaze is given in table 6.2, as a result from sample analysis by means of ICP-OES, silicon and tin have not been quantified [44].

Table 6.2: Range of composition of the white glaze in the Italian Renaissance lusters, [44]

Glaze composition (wt.%)				Glaze composition (ppm)	
PbO	15.0–29.8	MgO	0.1–1.4	Cu	76–2800
K_2O	5.7–9.6	Fe_2O_3	0.3–3.9	Mn	30–385
Na_2O	0.9–12.7	TiO_2	0.1–0.3	Cr	10–134
Al_2O_3	1.1–5.7			Ni	6–293
CaO	1.1–8.7			Zn	0–974

Yellow decorations are characterized by the presence of lead-antimonate yellow ($Pb_2Sb_2O_7$), sometimes also by the use of iron oxides (Fe_2O_3) that may give hues closer to orange. Cobalt oxides containing also traces of iron, nickel and arsenic are employed to give blues hues to the glaze. The colorant employed in this case is smalt, a potassium silicate glass containing cobalt (also called *zaffera*). For this colorant the Co/As ratio is important, that can give key information on the production technologies and on the provenance of the pigment.

In plot 6.10 you can see the cumulative spectrum obtained with GI-XRF, where the main component with fluorescence energy below 9 keV can be observed.

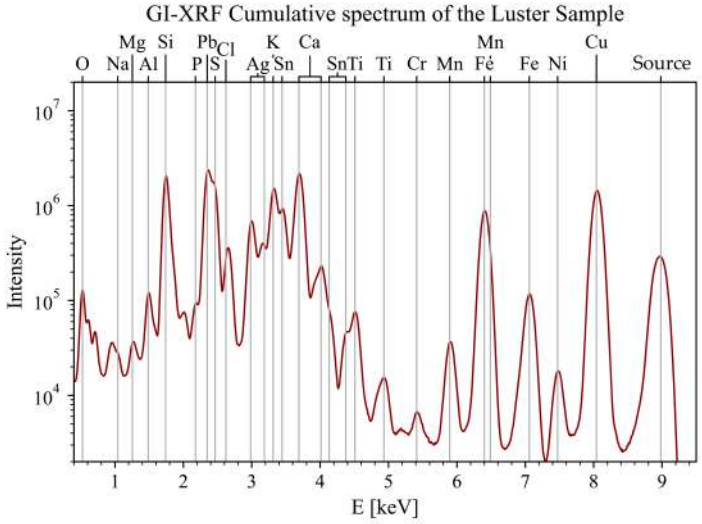

Figure 6.10: Cumulative spectrum collected summing the GI-XRF measurements, the main component with fluorescence energy below 9 keV can be observed. Element like Sr or Rb that may be present in ceramics cannot be distinguished through their L

6.3.1 Measurement protocol

The first measurement involved the GI-XRF scanning, where the sample has been excited with a source energy of 9.2 keV (just above the copper K edge), the angle of irradiation has been scanned in a range of 0° to 4.5° with a step of 0.005°, for a total of 901 spectra. The dwell time for each measurement is of 40 s and the detector has been placed at a distance of 9 mm from the sample. The source had an opening of $200 \times 100\mu m$.

In a second phase GE-XRF measurements were performed; also in this case the source energy has been kept at 9.2 keV, but the monochromator has been changed with the multilayer crystal, that ensures a higher source flux. The range of measurement has been divided into two step, a first scansion from 0° to 6° with a step of 0.01° (511 spectra), and a second one from 3° to 10° with a step of 0.1° (71 spectra). The dwell time has been kept always at 120 s. The detector in this case could not be moved closer to the sample, which also would have worsen the angular resolution of the measurement, and is placed at a distance of 146 mm.

6.3.2 Results

In figure 6.11 are shown the GI-XRF profiles collected on the luster sample, each plot highlights different elements.

In the plot is highlighted the profile of silver, which is the only element present only in the nanolayer, and of silicon which is instead

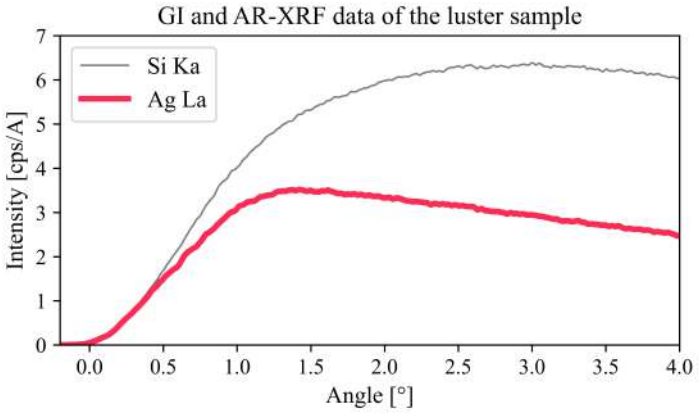

Figure 6.11: Profiles of silicon and silver collected with GI-XRF measurements on the luster sample.

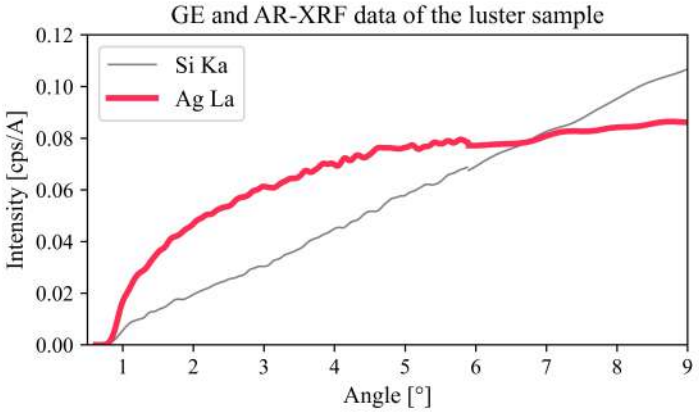

Figure 6.12: Profiles of silicon and silver collected with GE-XRF and AR-XRF measurements on the luster sample.

part of the matrix. Respect to the other profile, the profile of silver having reached the maximum intensity at approximately 1.2° steadily decreases. This behaviour is due to the fact that as the angle increases the path-length of the source radiation inside the nanolayer decreases, reducing the excitation of this layer.

With respect to the GI-XRF profile of the reference sample here the shape of the curves is completely different, first of all the surface is not optically flat with respect to the X-ray fluorescence wavelength, also the layers are not completely separated but there is a compenetration of the different materials. The composition of the interfaces is more similar to a gradient that to a real interface. For these reasons we do not expect fringes, on the opposite, we expect the behaviour of a bulk sample or of a buried layer inside a sample [33].

Also considering the GE-XRF and the AR-XRF profiles, plotted in figure 6.12, we can observe that silver profile has a different behaviour, respect to the one of silicon. In this case the excitation of each layer does not change during the scanning, but is the path-length of the

fluorescence radiation that changes, thus the self-attenuation of each signal. For this reason, at low angles, where we enhance the signal coming from the surface (indeed, we suppress the signal coming from the bulk), the profile of silver increases, then after all the signal coming from this layer has escaped, it remains constant. Instead, the signal of the elements present below the nanolayer continues increasing until: (I) the volume investigates is higher than the volume in which the element is present, (II) the volume analyzed is the maximum probed volume for that energy.

7 CONCLUSIONS

The study of the layered metal samples has shown that among the various angle dependant XRF techniques, AR-XRF, can easily be implemented in a laboratory, as a table-top instrument. To perform an AR-XRF measurement, the system only requires to tilt either the sample, the detector, or the source and to collect an XRF spectrum in each angular position. As the intensity of an analyte depends on its distribution inside the sample, on the sample structure, and on the geometry of measurement (the analyte excitation depends on the path-length crossed by the source radiation, while the fluorescence attenuation depends on the path-length crossed by the fluorescence radiation), a change in the latter parameter can be employed to retrieve information on the sample structure and to measure the massive thickness (if the density is unknown) of a layer.

For the golden foils on copper plate samples prepared in laboratory, we considered both the fluorescence signal coming from the bulk attenuated by the top-layer, and the one of the top-layer affected only by self-attenuation. The AR-XRF profiles have been modelled using the Sherman's equation for a monochromatic source with only three parameters: one that considers the top-layers absorption, one for the instrumental probability of the line emission and one for the background. The limited number of parameters has thus allowed to perform a reliable and fast fitting of the profiles, which have been compared with the profiles calculated with the FP-algorithm using the χ^2-method. The technique has shown good results, both using the self-attenuation of the gold fluorescence signal and the attenuation of the copper fluorescence signal, allowing to measure the gold layer thickness.

Then we applied the same technique on the analysis of a Puebla majolica sample, to retrieve information on the decoration structure. In this case thus, AR-XRF has been applied to analyze a real sample, where many more variables must be considered. Indeed only the composition of the underlying white glaze was known, while composition and thickness of the blue and black decoration was known only qualitatively. The main elements of the white glaze are lead and tin, employed respectively to reduce the softening temperature and to opacify the glaze. Blue decoration shows a similar composition with the addition of cobalt as chromophore and iron. Finally, black decorations, both the spots and the stripes, showed an intense signal of iron, and a lower signal of lead. With Respect to the metal samples prepared in our laboratory, the Puebla sample present a more com-

plex geometry, thus we decided to apply the data analysis not on the AR-XRF profiles but on their ratio with a reference line (Pb L_α that is present in all the spectra and characterizes the underling white glaze).

We observed then that the blue glazes have a composition too similar to the white glaze to be distinguished, indeed the ratio of the elements characterizing the blue glaze with the lead line (Co and Fe) are similar to those obtained from a bulk sample. It is proper to underline that long-distance diffusion phenomena and thickness can be a limit of this technique.

The analytical data derived from the black spot decorations behaves like a bilayer system, where the main elements composing the top-layer (the black glaze) are iron, lead and silicon. To retrieve information on the composition and thickness we compare the ratio with those calculated for a glaze composed by $(Fe_2O_3)_x(PbO)_y(SiO_2)_{(100-x-y)}$, keeping also the glaze thickness as an unknown parameter. The algorithm created for the FP-algorithm has been developed in-house ad employed a multidimensional matrix to speed-up the processing time. The χ^2-test has shown that the black glaze has a concentration of lead oxide lower than 10 %, an iron concentration in between 18 % and 33 %, and a thickness greater than 31 µm. To observe also how the effect of the underling glaze on the results we applied the same data analysis comparing the measures with profiles calculated employing different underling glazes (whose compositions have been found in literature).

Finally, the black stripes show a more complex layer structure, where the black glaze is covered by a Fe-poor top-layer. Three kinds of Fe-poor top-layer have been considered, keeping in mind the possible interaction during the firing process: silicon oxide, a glaze with a composition equal to the background glaze, and a glaze with a lower lead concentration respect to the background white glaze. As is reasonable to believe that the painter had employed the same material to create the same kind of decoration, the glaze concentration has been retrieved as the intersection of all the possible valid concentration of the measured spots. From the possible composition we could hence retrieve the thickness of the black layer. We observed then than the the black layer in any case has a concentration of lead oxide between 1 % and 6 %, and of iron oxide from 7 % to 17.5 %; while the thickness of both the black glaze and the top-layer depends indeed on the sampled spot.

In the case of micrometer-size layers AR-XRF seems to be an effective way to retrieve useful information on the sample structure, both for the layer thickness and composition. In our experiment only the main elements have been found useful to perform the data analysis, with different conditions (a different excitation or a longer dwell time and less steps) may be also other elements (like minor elements) can be employed. In the case of flat sample it is possible to use the net profiles, while for more complex geometries that can cause, for example,

shadowing effects (on the source or o the detector) is better to use the ratio profiles, that removes these effects. Besides, the layers must have a reasonable different composition to be distinguished, as minor differences become smeared out in the whole volume investigated, and they cannot be appreciate during the measurement, as in the case of the blue glaze.

The main limit of this technique is the number of parameters of the system. Even if from the ratio profiles is possible to evaluate the number of layers and their composition, like the presence of an iron-rich/lead-poor layer over an iron-poor/lead-rich layer, or the presence of a third covering layer; if no parameters are known the numerical estimation is quite poor, as more structure may give the same results.

At last, we employed grazing techniques to the analysis of a renaissance Italian luster sample; these techniques are indeed more suitable to analyze nanolayers. The main problems we faced are due to the alignment, even with the reference sample. We must keep in mind that in the Cultural Heritage field, the sample will not show the same effects that we observe in the field of material science, like fringes in the profiles, as net interfaces are quite rare and layers thicknesses are usually one or two order of magnitude higher. Nevertheless we could observe that silver, the sole element present exclusively in the more superficial nanolayer, was the only one behaving differently respect to the others, suggesting indeed that its presence is limited to a thin portion inside the sample. Beside, in the case of GE-XRF we employed a monochromatic source, the use of a polychromatic source instead, would probably give a better and more intense signal of all the elements contained in the sample. Finally, the other great limit is that the data treatment, performed comparing the measured profiles with simulated profiles, is at the moment difficult, as the softwares are developed for the field of material science where the samples contains few elements and many parameter are known (indeed this kind of samples is usually industrially or laboratory made). More studies and trials should be performed, however, also these techniques seem promising to give useful information where the layers thickness is too low to be characterized by AR-XRF.

The study of these samples has shown that AR-XRF and grazing techniques can be useful tools to analyse layered structure present in CH samples, both in the case of thin layered structure (like gilding) and in the case of thicker structures, i. e.glaze over a ceramic body. Nevertheless this technique, at the moment, is not as straightforward, at least in the data analysis, as other existing set-up, as confocal measurements; it requires the cross-checking of different data, as the number of variable is high (e. g.knowing the composition of the background glaze to obtain information on the covering coloured glaze). Despite these limits, that can be overcame with the analysis of more samples, and preforming more trials, Angle Resolved analysis

can be easily implemented in a laboratory system as requires little costs if compared to the employment of capillary lenses, especially considering new portable technologies like Arduino or Raspberry, that allows the creation of low-cost set ups, that easily match the requirements for the analysis of Cultural Heritage artifacts. For these reasons I believe that AR-XRF and grazing techniques deserve to be studied and employed in the field of Cultural Heritage.

APPENDIX

A FITTING PLOT OF THE GILDED SAMPLE

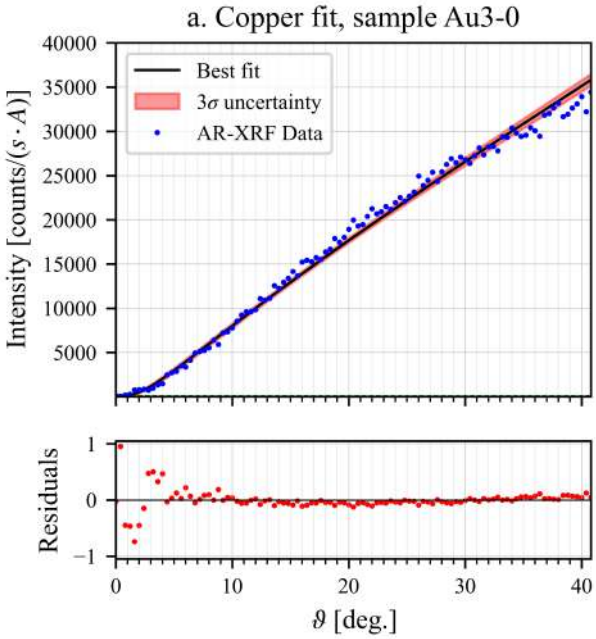

Figure A.1: Fitting plot of the gold Kα fluorescence line of the gilded sample made of 3 golden foils, spot 0.

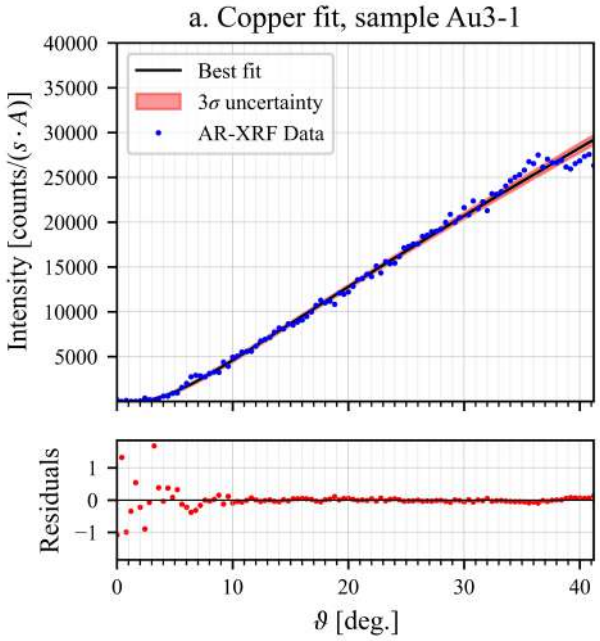

Figure A.2: Fitting plot of the gold Kα fluorescence line of the of the gilded sample made of 3 golden foils, spot 1.

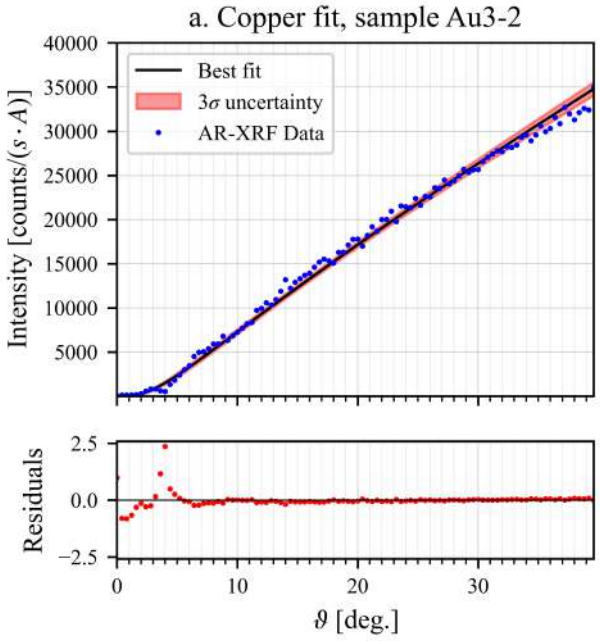

Figure A.3: Fitting plot of the gold Kα fluorescence line of the of the gilded sample made of 3 golden foils, spot 2.

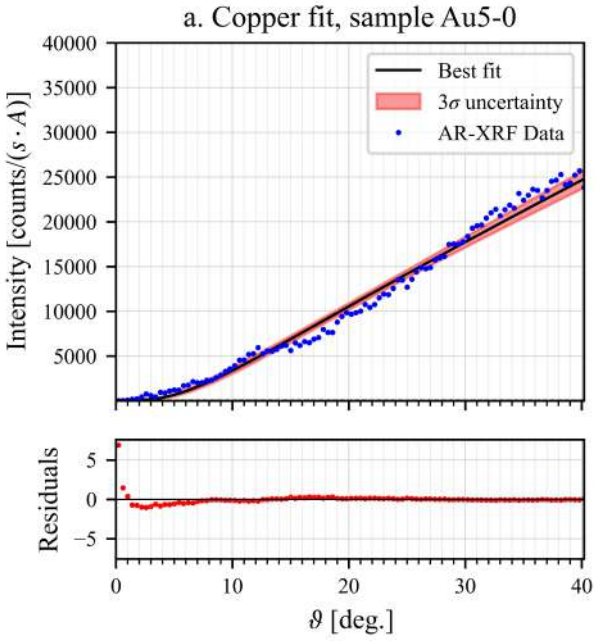

Figure A.4: Fitting plot of the gold Kα fluorescence line of the of the gilded sample made of 5 golden foils, spot 0.

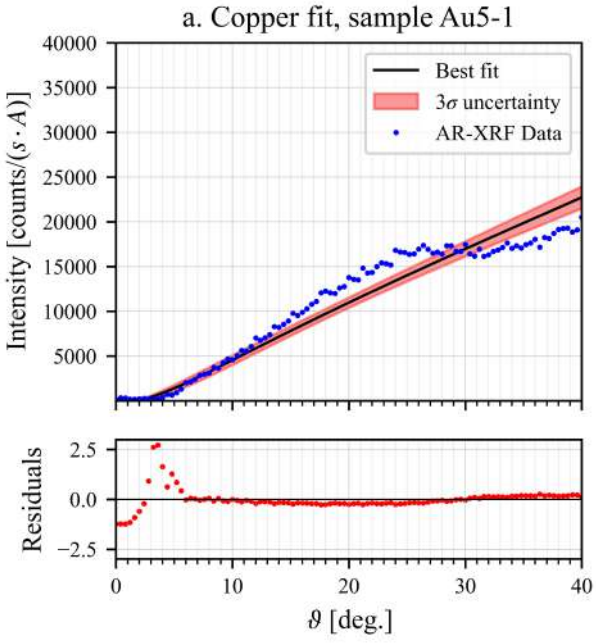

Figure A.5: Fitting plot of the gold Kα fluorescence line of the of the gilded sample made of 5 golden foils, spot 1.

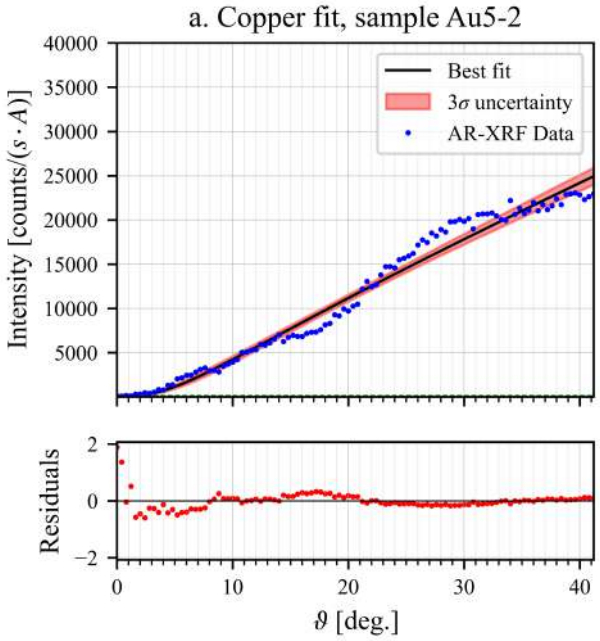

Figure A.6: Fitting plot of the gold Kα fluorescence line of the of the gilded sample made of 5 golden foils, spot 2.

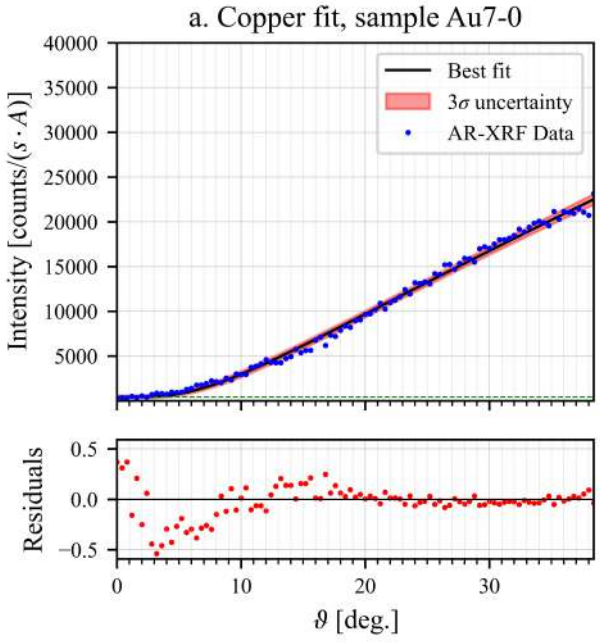

Figure A.7: Fitting plot of the gold Kα fluorescence line of the of the gilded sample made of 7 golden foils, spot 0.

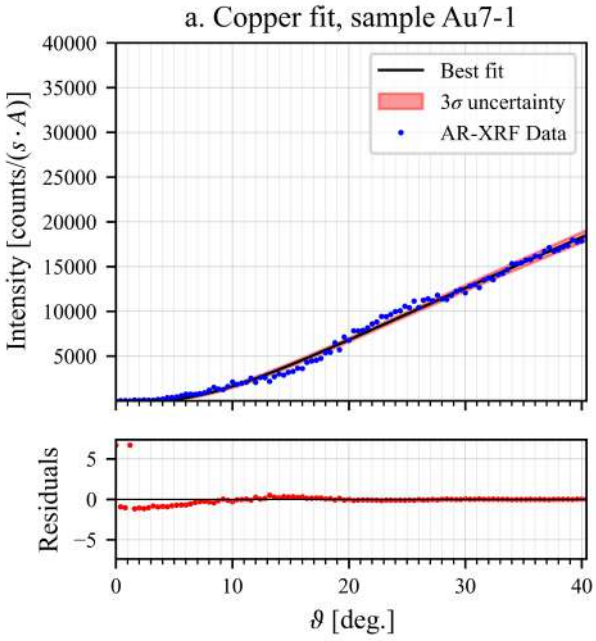

Figure A.8: Fitting plot of the gold Kα fluorescence line of the of the gilded sample made of 7 golden foils, spot 1.

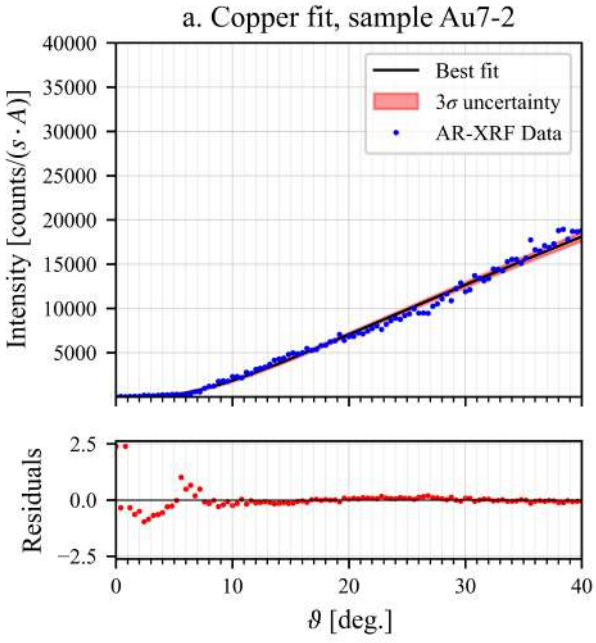

Figure A.9: Fitting plot of the gold Kα fluorescence line of the of the gilded sample made of 7 golden foils, spot 2.

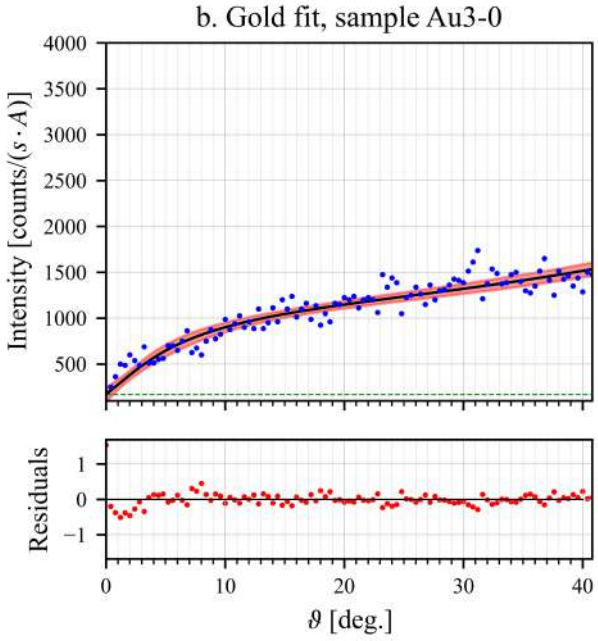

Figure A.10: Fitting plot of the gold Lα fluorescence line of the gilded sample made of 3 golden foils, spot 0.

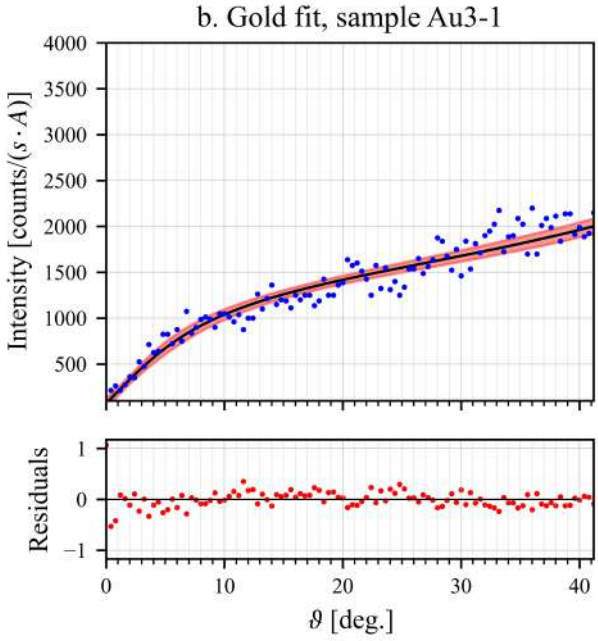

Figure A.11: Fitting plot of the gold Lα fluorescence line of the of the gilded sample made of 3 golden foils, spot 1.

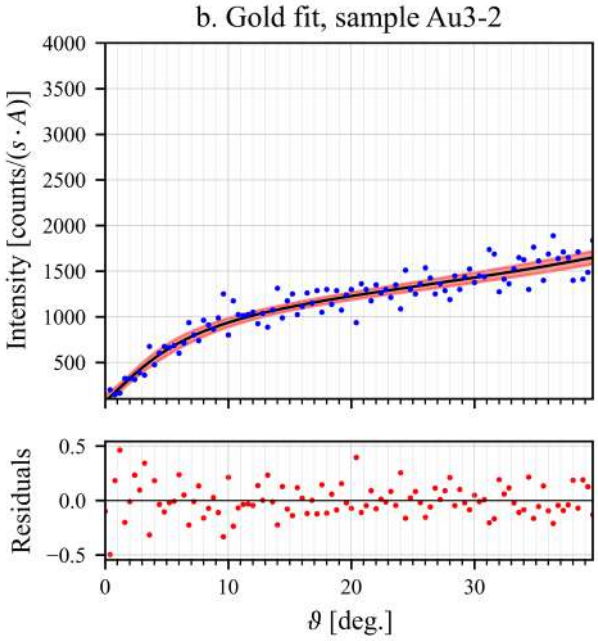

Figure A.12: Fitting plot of the gold Lα fluorescence line of the of the gilded sample made of 3 golden foils, spot 2.

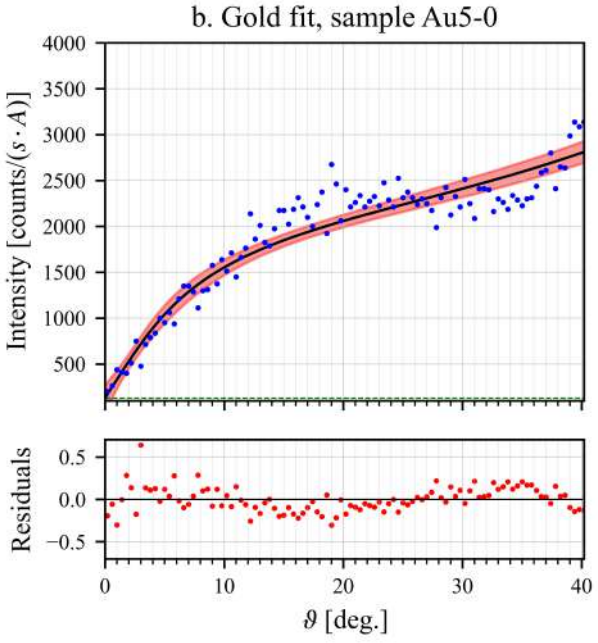

Figure A.13: Fitting plot of the gold Lα fluorescence line of the of the gilded sample made of 5 golden foils, spot 0.

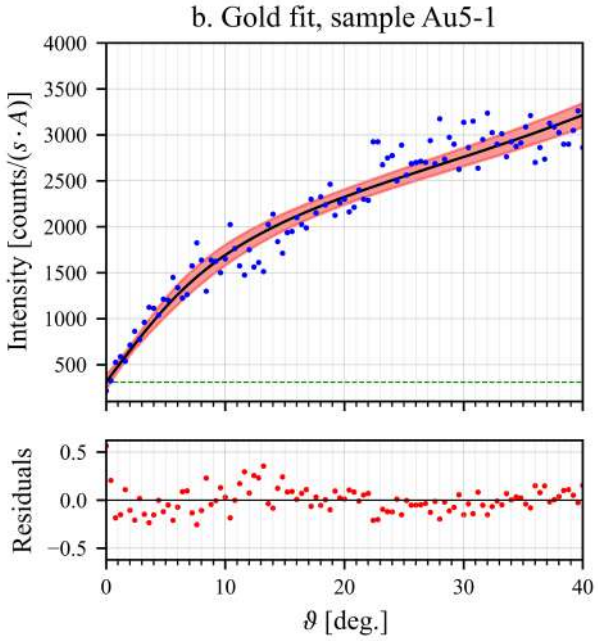

Figure A.14: Fitting plot of the gold Lα fluorescence line of the of the gilded sample made of 5 golden foils, spot 1.

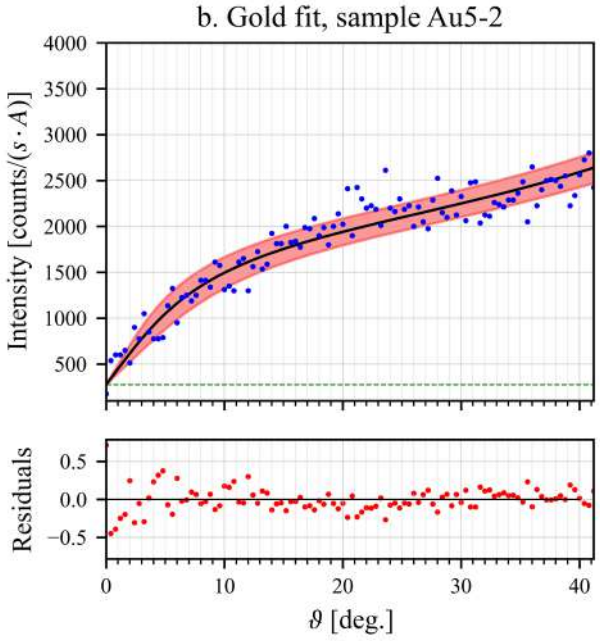

Figure A.15: Fitting plot of the gold Lα fluorescence line of the of the gilded sample made of 5 golden foils, spot 2.

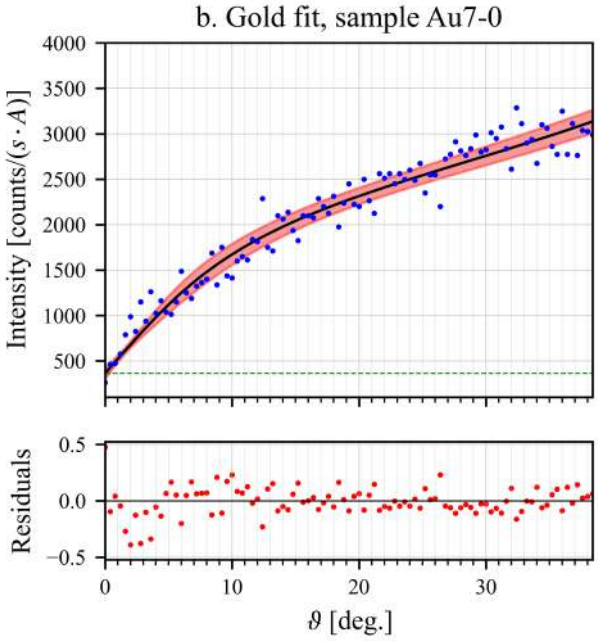

Figure A.16: Fitting plot of the gold Lα fluorescence line of the of the gilded sample made of 7 golden foils, spot 0.

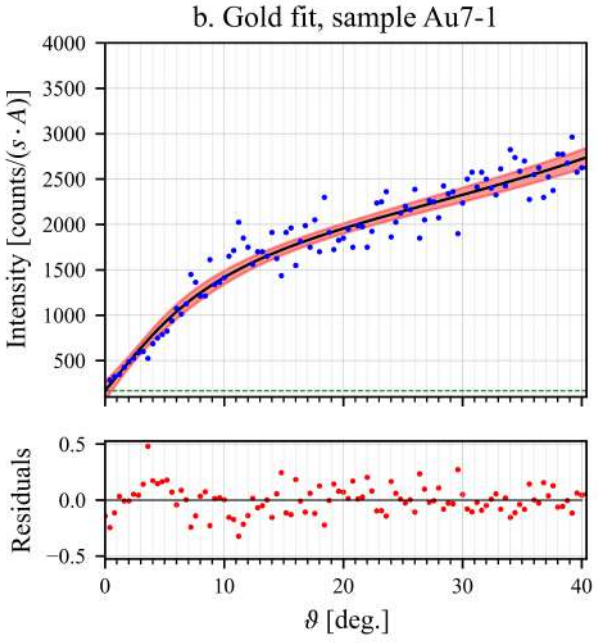

Figure A.17: Fitting plot of the gold Lα fluorescence line of the of the gilded sample made of 7 golden foils, spot 1.

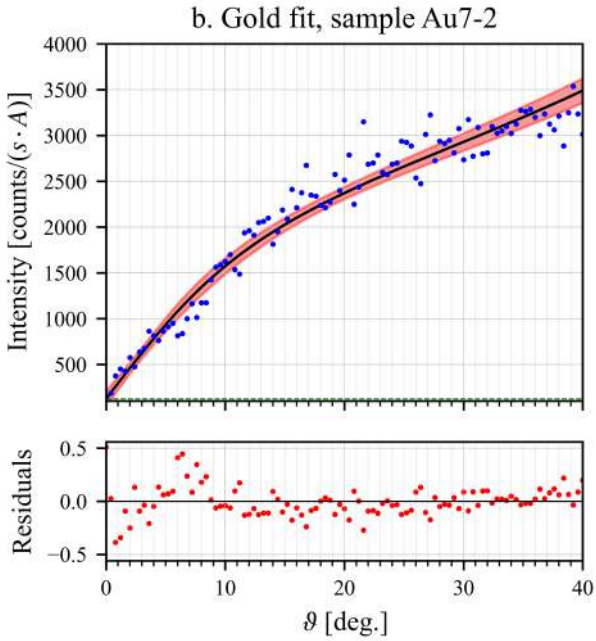

Figure A.18: Fitting plot of the gold Lα fluorescence line of the of the gilded sample made of 7 golden foils, spot 2.

B FP-ALGORITHM: PYTHON IMPLEMENTATION

Here we report step-by-step the algorithm and the code implementation to calculate the FP-profile. As a multi-layer system is complex, the calculations of the FP data requires a long machine time. The algorithm has been built in-house, using python codes; to reduce the machine time it works in a five-dimensional space, in which each dimension represents one of the variables, as summarized in table B.1.

The final results is then a 5-dimensional matrix, in which each value represents the intensity of one analyte, composing a specific layer, excited by one discretized energy of the source, for a tilting angle of the sample and attenuated by a top-layer with a certain thickness. If this matrix is collapsed, summing along the dimensions m and n (source energies and layers), we obtain the total intensity of each element, measured with a specific geometry and attenuated by a top-layer with a defined thickness.

The use of multidimensional matrices has the advantage of increasing the calculation speed as less cycles are employed in the calculations themselves; anyway as more data are stored in the calculation process, more space is needed (even though the final space required is the same).

We will describe now the algorithm employed for the FP-calculations, and the functions created to optimize the process. The code work in a four steps process:

1. Definition of the parameters: the only part of the script which is changed by the user;

Table B.1: Dimensions employed to calculate the Fundamental Parameters profiles, the numbering follows the python convention for which the first element is the 0 element.

Dimension	Name	Description
0	m	Source Energy
1	n	Layer
2	o	Element
3	p	Angle of tilting
4	q	Thickness of the top layer

2. Entering the cycles: the index of the final dataframe is created to reduce the required space and calculation time, the variables are inserted in the calculation algorithm;

3. Final definition of the structure: the structure of the sample is created, if defined as oxides composition is converted in elemental composition; the density of each layer is calculated;

4. Calculation of the data: here the real calculations are processed, the data that are constant for all the cycles (like the probability emission of each fluorescence line) are calculated only on the first cycle to reduce the algorithm time; the data are finally saved in a *.csv* file.

Definitions of the parameters

The parameters inserted by the user are:

- The source distribution,
- The layers composition,
- The layer numbers and positions,
- The thickness of each layer
- The angles of irradiation and detection
- The elements for which we want to calculate the intensity
- The lines for which we want to calculate the intensity

As for each element the code accepts only one fluorescence line if we want to calculate the intensity of more fluorescence lines we have to run the code again, this issue will be corrected in future versions.

Here we show and explain the code as is employed for the calculations of the black stripes structure, that as we will explain later, is assumed to be a tri-layers system, composed of a thin layer of the white glaze, the black glaze and again the white glaze.

```
#Top-Layer thickness in cm
TX0 = np.round(np.arange(0.1e-4, 10.1e-4, 0.2e-4), 6)

#Second Layer thickness in cm
TX1 = np.arange(14-4, 52e-4, 2e-4)

#Source stored as a csv file
Source = pd.read_csv('Source_path.csv', index_col = ['E'])

#Tilting angle
alpha = np.deg2rad(np.arange(1, 102)*0.41666)

#Irradiation and detection angles
```

```
phi = np.cos(alpha)
theta = np.sin(alpha)/np.sqrt(2)

#The angles are converted in vectors with dimensions [1 x 1 x 1 x
     p x 1]
B = ExpDims(1/phi, 0, 3)
D = ExpDims(1/theta, 0, 3)

# White glaze composition and name
Glazes = [WGlazeC]
GlazesNames = ['GlC']

# Here we define the composition of the black glaze
# Concentration of Fe2O3 in %
VarFe = np.arange(5, 24.5, .5)

#Concentration of PbO in %
VarPb = np.arange(.5, 15.5, .5)

#Elements for which we want to calculate the fluorescence
    intensity
FluoEls = ['Fe', 'Pb']
FluoEls = [pt.elements.symbol(i) for i in FluoEls]

# Lines for which we want to obtain the profiles
LLines = [[xl.KA_LINE, xl.LA_LINE],
          [xl.KB_LINE, xl.LB_LINE]]
```

Enetering the cycles

As we want have to perform different calculations with different structures, and we need to calculate the fluorescence profiles for both the α and β fluorescence lines, we nest different *for* cycles:

1. the profiles for two group of lines (Kα and Lα on the firs cycle, and Kβ and Lβ on the second cycle)
2. we change the thickness of the black layer (the second layer)
3. we change the amount of Fe_2O_3 in the black layer
4. we change the amount of PbO in the black layer

```
# Cycle on the fluorescence lines we create also a suffix to save
     the data
for Lines in LLines:
    if xl.KB_LINE in Lines:
        NL = 'B'
    elif xl.KA_LINE in Lines:
        NL = 'A'
```

```
    #To save memory and time we create here the index of the
        final dataframe
    IDX = cartesian_product(np.array(FluoEls), np.round(np.
        rad2deg(alpha), 4), np.round(Tx0, 6))
    IDX = pd.MultiIndex.from_arrays(IDX.transpose(), names = ['El
        ', 'Th', 'MT0'])

    # Inzialize a counter to 0
    ncount = 0

    # Cycle on the second layer thickness
    for tx1 in TX1:

        # Define here the matrix conatining the thiknesses of the
             layers
        DFT = TriLayersThick(TX0, tx1)

        # Cycle on the iron and lead content
        for x in VarFe:
            for y in VarPb:
                ...
```

The function *TriLayerThick* define the linear thickness of the layers composing the sample and expands it along the dimension q:

```
def TriLayersThick(Tx0, Tx1):
    # Thickness of the fist layer [size 1 x q]
    tx0 = np.expand_dims(Tx0, axis = 1)

    # Thickness of the second layer converted into an array that
        has the same lenght of the array tx0 [size 1 x q]
    tx1 = Tx1*tx0/tx0

    # Thickness of the bulk [size 1 x q]
    tx2 = 600E-4*tx0/tx0

    # We store all the thicknesses in an array with size [n x q]
    DFT = np.array([tx0.flatten(), tx1.flatten(), tx2.flatten()])
    DFT = pd.DataFrame(DFT)

    return DFT
```

Final definition of the structure and calculation of the densities

Inside the cycle is defined the algorithm to calculate the fluorescence intensity of the sample.

```
# Composition of the top-layer
TopGlaze, y, z = Top_LayComp(x, y)

# Definition of the compositions and layers
```

```
Layers = [TopLayer, SecondLayer, BottomLayer]

# Create a unique dataframe with the composition in oxides
OxComp = pd.DataFrame(Layers).fillna(0)

# Convert the dataframe in its elemental version
DFc = NOX_Calc(OxComp)

# Calculate the density of each layer
DLay = CalcOXDens(Layers)
DLay = pd.DataFrame([DLay], index = ['Density']).transpose()

# Convert the densities in massive thicknesses
MassT = DFT*DLay.values
```

Each layer composition is defined with a dictionary in which the element or the oxide is the *key*, and the concentration is the *value*. For example the composition of a layer can be defined as:

```
Composition = {'Na2O': 4.3,
               'MgO': 0.23,
               'Al2O3': 9.7,
               'SiO2': 54.1,
               'K2O': 3.08,
               'CaO': 1.2,
               'Fe2O3': 0.76,
               'SnO2': 3.5,
               'PbO': 26
              }
```

The composition of the top-layer is defined by the x and y values cycled in the two *for* cycles, the dictionay is then created using the *Top_LayComp* function. This function assume the layer to be a ternary system in which SiO_2 closes the composition at 100 %:

```
def Top_LayComp(x, y):
    z = 100 - x - y

    TopGlaze = {'Fe2O3': x,
                'PbO': y,
                'SiO2': z,
               }
    return TopGlaze, y, z
```

The other two functions *NOX_Calc* and *CaclOXDens* convert the dataframe from oxides concentration in elemental concentration, and calculate the layer density starting from the oxides composition:

```
def NOX_Calc(OxComp):
    # OxComp is a dataframe that has as rows the layers and as
        columns the oxides and
```

```
    as values their percentage concentrations

    # Creates the dataframe
    NOxComp = pd.DataFrame()

    # Cycle on the layer
    for Layer in OxComp.index:

    # Initialize the Oxygen and Non Oxygen amount
        O = 0
        NO = 0
        RowComp = {}

        # Cycle on the oxides
        for Ox in OxComp.columns:

            # Convert in formula and extract the mass fractions
            MF = pt.formula(Ox).mass_fraction

            # Cycle on the elements composing the oxides
            for k in MF.keys():

                # Add the oxygen to its own value
                if k == pt.elements.O:
                    O += OxComp.loc[Layer, el]*MF[k]

                # Add the other elements to their own columns
                else:
                    RowComp[k] = OxComp.loc[Layer, el]*MF[k]
                    pDensity = []
        RowComp[pt.elements.O] = O

        NOxComp = NOxComp.append(RowComp, ignore_index = True)

    # Normalizes the rows
    Norm = NOxComp.values.sum(axis = 1)
    DFc = NOxComp.divide(Norm, axis = 0)
    DFc.index.name = 'Layer'
    DFc.columns.name = 'Element'

    return DFc

def CalcOXDens(Comps, DenDB = OXDensities):
    # Comps is the composition dictionary, while DenDB is a
        dictionary in which the keys are the oxides and the
        values are their densities

    #Initialize the density
    Dens = []

    # Cycle on the composition
    for Comp in Comps:
```

```
        #Initialize the denominator and numerator of the fraction
        D = 0
        N = 0

        # Cycle on the oxides
        for key in Comp.keys():

            # Check if the oxide is in the database and updates
                the numerator and denominator of the fractions
            if key in DenDB.keys():
                N += Comp[key]
                D += Comp[key]/DenDB[key]

            # If the oxide is not in the database raises an erorr
            else:
                print(f"{key} density is not in the database")

        # Calculate the density
        Dens += [N/D]
    return Dens
```

Calculation of the FP data

In the code here presented we calculate the fluorescence intensity for each fluorescence element, the calculations allows also to retrieve the single contributions of each layer, just avoiding to sum along the n dimension will return a dataframe of size $[n \times o \times p \times q]$ with the individual intensities (already weighted for the self-attenuation and the attenuation of the covering layers).

```
# In the first cycle it calculates all the physical values needed
# DFmi is the DataFrame of the elements attenuations at the
    fluorescence energies
# DFm0 is the DataFrame of the elements attenuations at the
    source energies
# Cost is the Line probability (considering fluorescence yield,
    jump factor and rad. rate) at the source energy weighted for
    the detector efficiency and the source intensity

if ncount == 0:
    DFmi, DFm0, Cost = Calc_cost(DFc, FluoEls, Source, Lines)

# Calculates the total attenuation of the layers at the source
    and fluorescence energy using a dot product [Layers x
    Elements] dot [Elements x Energy] = [Layer x Energy] [m x o]
DFs0 = DFc.dot(DFm0)  #Source Energy
DFsi = DFc.dot(DFmi)  #Fluorescence Energy

# Expand the composition of the fluorescence elements on the
    layer axis
```

```
DFc = np.expand_dims(DFc.loc[:, FluoEls], axis = 1)

# Mutiplies the concentration of the fluorescence elements for
    the probability of line emission
# G has dimensions [m x n x o]
G = DFc*Cost

## M is the effective attenuation coefficient u_s(E_0)/sin(phi) +
     u_s(E_i)/sin(theta)
## M ha dimensions [m x n x o x p]
## M = A x B + C x D
A = ExpDims(DFs0, 2, 4)              # [m x n x 1 x 1] u_s(E_0)
C = ExpDims(DFsi, 1, 2, 4)           # [m x 1 x o x 1] u_s(E_i)
M = (A*B+C*D)                        # [m x n x o x p]

## Expand G along the dimension p
G = np.expand_dims(G, axis = 3)      # [m x n x o x 1]
I0 = G*B/M

# Expand I0 along q [m x n x o x p x 1]
I0 = np.expand_dims(I0, axis = 4)    # [m x n x o x p x 1]

## Calculate the self attenuation and the attenuation of the
    layers, they can be calculated starting from the matrix M
## X and Y are two matrixes [m x n x o x p x q]
## X = 1-exp[-R*M] self  attenuation of each layer
## Y = exp[-Sum[R*M]] attenuation of the covering layers
## R is the matrix of dimensions [m x 1 x 1 x 1 x q] of massive
    thickness
## NB. Y = 1 for each element of the layer 0

## Add the dimension q for the thicknesses
M = np.expand_dims(M, axis = 4)      # [m x n x o x p x q]
R = ExpDims(MassT, 1, 4)             # [m x 1 x 1 x 1 x q]

# Calculate X
X = 1-np.exp(-R*M)                   # [m x n x o x p x q]

# Calculate Y, then roll each row of one position [0 -> 1, 1 -> 2
     etc]
# Substitute the firs row with all 1
Y = np.exp(-np.cumsum(R*M, axis = 0))
Y = np.roll(Y, 1, axis = 0)
Y[0] = 1

# Calculate the final intensity
I = I0*X*Y

# Calculate the total intensity summing along the m and n
    dimension
# IT has size [o x p x q]
IT = I.sum(axis = 1).sum(axis = 0)
```

```
# Create and save the DataFrame
DFIT = pd.DataFrame(IT.flatten(), IDX, columns = ['TIntensity'])
DFIT.to_csv(f'file_path.csv', sep = ';')

# Add one counter
ncount += 1
```

The function employed on the first cycle to calculate the fluorescence and attenuation constants is so defined:

```
def Calc_cost(DFc, FluoEls, Lines, Source):
# DFc is the DataFrame of the concentrations, in which each
    column is an element and each row is a layer
# Fluo Els are the elements we want to calculate the fluorescence
# Lines are the fluorescence lines (one for each Fluo Els)
# Source is the source distribution

    #Initialize the variables
    DFmi = []
    DFm0 = []
    Cost = []
    Eff = []
    Ei = []

    # Cycle on the composing elements
    for j in DFc.columns:

        # Extract the atomic number
        Zj = j.number

        # Cycle on the fluorescence elements
        if j in FluoEls:
                if Zj <= 42:
                    Line = Lines[0]
                else:
                    Line = Lines[1]

                # Calculate the fluorescence energy
                Ei += [xl.LineEnergy(Zj, Line)]

        # Cycle on the source energy
        for E0 in Source.index:

            # Extract the total attenuation coefficient at the
                source energy
            DFm0 += [{'Element': j,
                      'Energy': E0,
                      'u_E0': xl.CS_Total(Zj, E0)}]

            # Extract the fluorescence line probability for each
                Fluo Els at each source energy
```

```
            if j in FluoEls:

                Cost += [{'Energy': E0,
                          'Element': j,
                          's_Ph': xl.CS_FluorLine(Zj, Line, E0)
                         }]

    # Cycle on the fluorescence energy
    for E in Ei:

        # Calculates the efficiency at the fluo energy
        Eff += [Efficency(E)]

        # Cycle on the elements
        for j in DFc.columns:
            Zj = j.number

            # Extract the attenuation at the fluorescence nergy
            DFmi += [{'Energy': E,
                      'Element': j,
                      'u_Ei': xl.CS_Total(Zj, E)
                      }]
    # Creates an arrey of the efficiency
    Eff = np.array(Eff)

    # Creates the DataFrames
    DFm0 = pd.DataFrame(DFm0).set_index(['Element', 'Energy']).
        unstack().droplevel(0, axis = 1)
    DFmi = pd.DataFrame(DFmi).set_index(['Element', 'Energy']).
        unstack().droplevel(0, axis = 1)

    # Cost is multiplied for the efficiency and the Source
        intensity
    Cost = pd.DataFrame(Cost).set_index(['Energy', 'Element']).
        unstack().droplevel(0, axis = 1)*Eff*Source.values
    Cost = np.expand_dims(Cost, axis = 0)

    return DFmi, DFm0, Cost
```

The efficiency is calculated through its own function *Efficiency* that only has an argument `E`, the energy; all the parameters needed are already inside this function (as the instrument employed is always the same):

```
def Efficency(Ei):

    # Window data: elements, attenuation, density and thickness
        in cm
    W = pt.elements.Be
    muW = xl.CS_Total(W.number, Ei)
    rhoW = W.density
    dW = 8e-4
```

```
# Crystal data
Cr = pt.elements.Si
muCr = xl.CS_Total(Cr.number, Ei)
rhoCr = Cr.density
dCr = 450e-4

# Atmosphere data
A = 'Air, Dry (near sea level)'
dA = 1.697
rhoA = 1.225e-3
muA = xl.CS_Total_CP(A, Ei)

## Calculates the efficiency
Eff = np.exp(-(muW*rhoW*dW+muA*rhoA*dA))*(1-np.exp(-muCr*
    rhoCr*dCr))

return Eff
```

C VARIATION OF THE WHITE GLAZE COMPOSITION

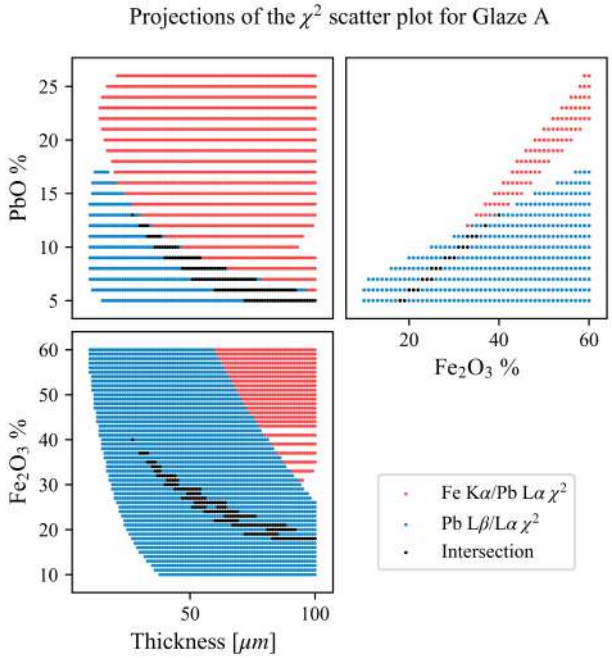

Figure C.1: Scatter plot projection of the accepted variables for a sample with a background with the glaze A composition.

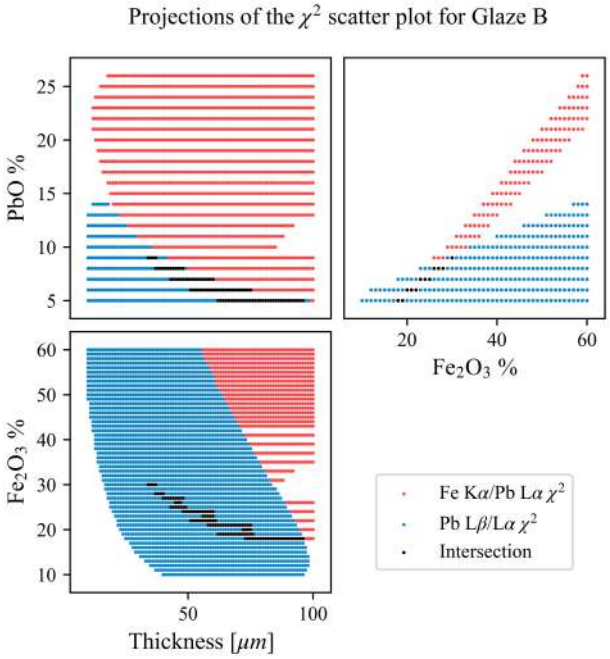

Figure C.2: Scatter plot projection of the accepted variables for a sample with a background with the glaze B composition.

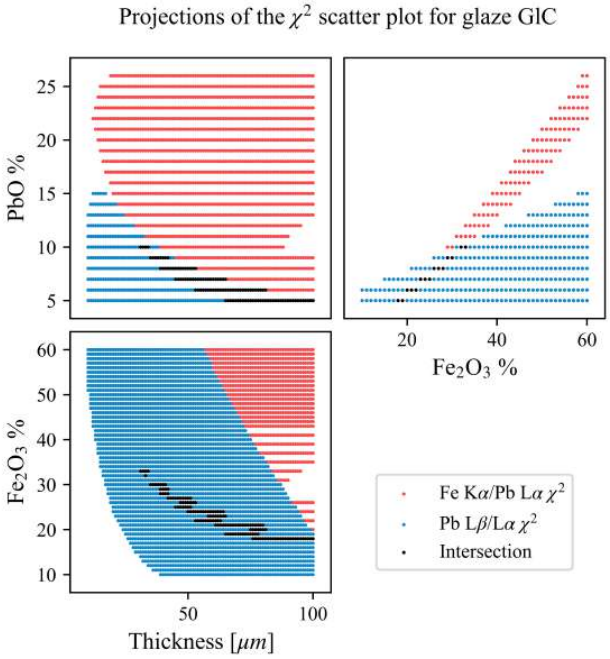

Figure C.3: Scatter plot projection of the accepted variables for a sample with a background with the glaze C composition.

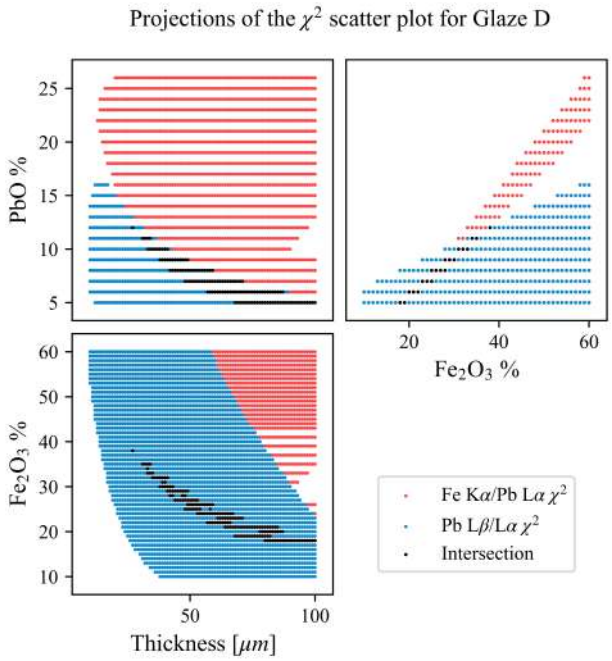

Figure C.4: Scatter plot projection of the accepted variables for a sample with a background with the glaze D composition.

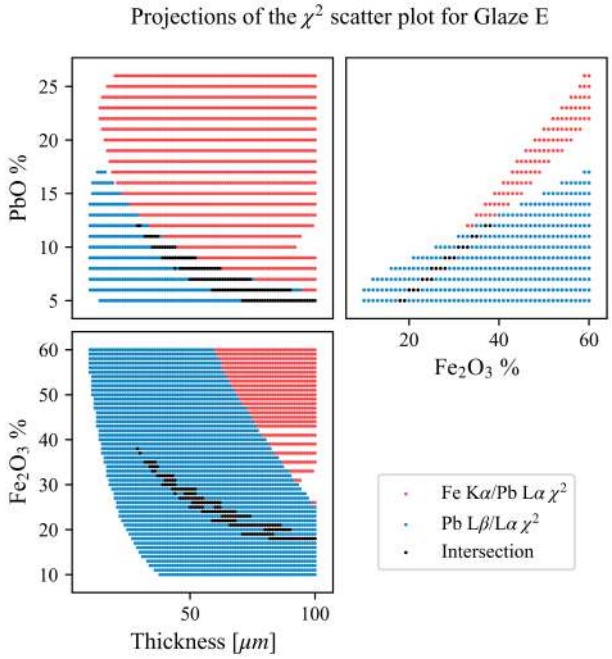

Figure C.5: Scatter plot projection of the accepted variables for a sample with a background with the glaze E composition.

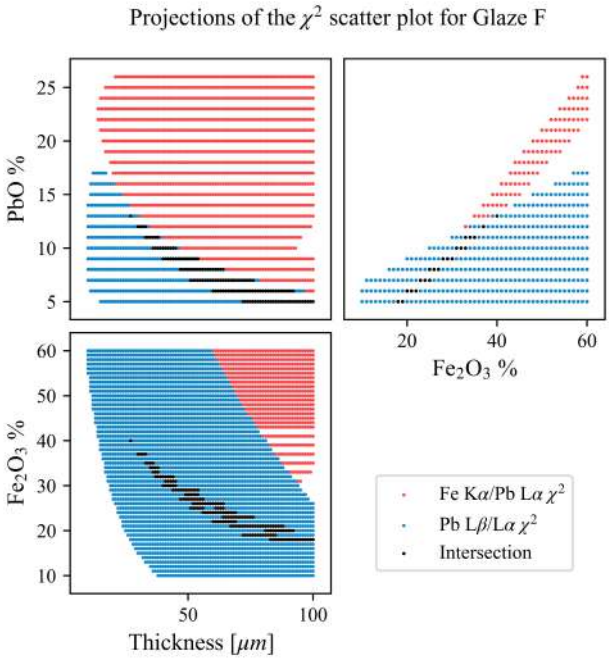

Figure C.6: Scatter plot projection of the accepted variables for a sample with a background with the glazeF composition.

BIBLIOGRAPHY

[1] F. Ager, M. Ferretti, M. Grilli, D. Juanes, I. Ortega-Feliu, M. Respaldiza, C. Roldán, and S. Scrivano. "Reconsidering the Accuracy of X-ray Fluorescence and Ion Beam Based Methods When Used to Measure the Thickness of Ancient Gildings." In: *Spectrochimica Acta Part B: Atomic Spectroscopy* 135 (Sept. 2017), pp. 42–47. ISSN: 05848547. DOI: 10.1016/j.sab.2017.06.017.

[2] M. Alfeld and L. de Viguerie. "Recent Developments in Spectroscopic Imaging Techniques for Historical Paintings - A Review." In: *Spectrochimica Acta Part B: Atomic Spectroscopy* 136 (Oct. 2017), pp. 81–105. ISSN: 05848547. DOI: 10.1016/j.sab.2017.08.003.

[3] J. Als-Nielsen and D. McMorrow. *Elements of Modern X-ray Physics: Als-Nielsen/Elements*. Hoboken, NJ, USA: John Wiley & Sons, Inc., Mar. 18, 2011. ISBN: 978-1-119-99836-5 978-0-470-97395-0. DOI: 10.1002/9781119998365.

[4] D. Attwood. *Soft X-Rays and Extreme Ultraviolet Radiation: Principles and Applications*. 1st ed. Cambridge University Press, Aug. 28, 1999. ISBN: 978-0-521-65214-8 978-0-521-02997-1 978-1-139-16442-9. DOI: 10.1017/CBO9781139164429.

[5] J. Baumann, D. Grötzsch, O. Scharf, T. Kodalle, R. Bergmann, F. Bilchenko, I. Mantouvalou, and B. Kanngießer. "A Compact and Efficient Angle-Resolved X-ray Fluorescence Spectrometer for Elemental Depth Profiling." In: *Spectrochimica Acta Part B: Atomic Spectroscopy* 181 (July 1, 2021), p. 106216. ISSN: 0584-8547. DOI: 10.1016/j.sab.2021.106216.

[6] J. Baumann et al. "Laboratory Setup for Scanning-Free Grazing Emission X-ray Fluorescence." In: *Analytical Chemistry* 89.3 (Feb. 7, 2017), pp. 1965–1971. ISSN: 0003-2700, 1520-6882. DOI: 10.1021/acs.analchem.6b04449.

[7] J. Baumann, Y. Kayser, and B. Kanngießer. "Grazing Emission X-Ray Fluorescence: Novel Concepts and Applications for Nano-Analytics." In: *physica status solidi (b)* 258.3 (2021), p. 2000471. ISSN: 1521-3951. DOI: 10.1002/pssb.202000471.

[8] R. S. Becker, J. A. Golovchenko, and J. R. Patel. "X-Ray Evanescent Wave Absorption and Emission." In: *Physical Review Letters* 50.3 (Jan. 17, 1983), pp. 153–156. DOI: 10.1103/PhysRevLett.50.153.

[9] L Bonizzoni, A Galli, and M Milazzo. "Direct Evaluation of Self-Absorption Effects in Dark Matrices by Compton Scattering Measurements." In: (2000), p. 6.

[10] L. Bonizzoni, A. Galli, and M. Milazzo. "Analyses of the Stained Glasses of Certosa Di Pavia." In: *X-Ray Spectrometry* 31.1 (2002), pp. 35–38. ISSN: 1097-4539. DOI: 10.1002/xrs.530.

[11] C. E. Bottaini, A. Brunetti, I. Montero-Ruiz, A. Valera, A. Candeias, and J. Mirão. "Use of Monte Carlo Simulation as a Tool for the Nondestructive Energy Dispersive X-ray Fluorescence (EDXRF) Spectroscopy Analysis of Archaeological Copper-Based Artifacts from the Chalcolithic Site of Perdigões, Southern Portugal." In: *Applied Spectroscopy* 72.1 (Jan. 2018), pp. 17–27. ISSN: 0003-7028, 1943-3530. DOI: 10.1177/0003702817721934.

[12] J. Brocchieri, E. Scialla, and C. Sabbarese. "Estimation of Ag Coating Thickness by Different Methods Using a Handheld XRF Instrument." In: *Nuclear Instruments and Methods in Physics Research Section B: Beam Interactions with Materials and Atoms* 486 (Jan. 1, 2021), pp. 73–84. ISSN: 0168-583X. DOI: 10.1016/j.nimb.2020.11.006.

[13] A. Brunetti, B. Golosio, T. Schoonjans, and P. Oliva. "Use of Monte Carlo Simulations for Cultural Heritage X-ray Fluorescence Analysis." In: *Spectrochimica Acta Part B: Atomic Spectroscopy* 108 (June 2015), pp. 15–20. ISSN: 05848547. DOI: 10.1016/j.sab.2015.03.014.

[14] C. Bui, L. Confalonieri, and M. Milazzo. "Use of Compton Scattering in Quantitative XRF Analysis of Stained Glass." In: *International Journal of Radiation Applications and Instrumentation. Part A. Applied Radiation and Isotopes* 40.5 (Jan. 1989), pp. 375–380. ISSN: 08832889. DOI: 10.1016/0883-2889(89)90200-1.

[15] A. Caiger-Smith. *Lustre Pottery*. Gentle Breeze Pub Co, Jan. 1, 1985. 246 pp. ISBN: 978-0-9650786-5-8.

[16] S. Carboni. "The Early Period." In: *Glass from Islamic Lands*. London: Thames & Hudson, June 17, 2002. ISBN: 978-0-500-97607-4.

[17] R. Cesareo, J. T. de Assis, C. Roldán, A. D. Bustamante, A. Brunetti, and N. Schiavon. "Multilayered Samples Reconstructed by Measuring Kα/Kβ or Lα/Lβ X-ray Intensity Ratios by EDXRF." In: *Nuclear Instruments and Methods in Physics Research Section B: Beam Interactions with Materials and Atoms* 312 (Oct. 2013), pp. 15–22. ISSN: 0168583X. DOI: 10.1016/j.nimb.2013.06.019.

[18] W. G. Cochran. "The χ2 Test of Goodness of Fit." In: *The Annals of Mathematical Statistics* 23.3 (Sept. 1952), pp. 315–345. ISSN: 0003-4851, 2168-8990. DOI: 10.1214/aoms/1177729380.

[19] P. Colomban. "The Use of Metal Nanoparticles to Produce Yellow, Red and Iridescent Colour, from Bronze Age to Present Times in Lustre Pottery and Glass: Solid State Chemistry, Spectroscopy and Nanostructure." In: *Journal of Nano Research* 8

(2009), pp. 109–132. ISSN: 1661-9897. DOI: 10.4028/www.scientific.net/JNanoR.8.109.

[20] D. K. G. De Boer. "Calculation of X-Ray Fluorescence Intensities from Bulk and Multilayer Samples." In: *X-Ray Spectrometry* 19.3 (June 1990), pp. 145–154. ISSN: 0049-8246, 1097-4539. DOI: 10.1002/xrs.1300190312.

[21] P. de Bokx, C. Kok, A. Bailleul, G. Wiener, and H. Urbach. "Grazing-Emission X-ray Fluorescence Spectrometry; Principles and Applications." In: *Spectrochimica Acta Part B: Atomic Spectroscopy* 52.7 (July 1997), pp. 829–840. ISSN: 05848547. DOI: 10.1016/S0584-8547(96)01644-8.

[22] T. Emoto, Y. Sato, Y. Konishi, X. Ding, and K. Tsuji. "Development and Applications of Grazing Exit Micro X-ray Fluorescence Instrument Using a Polycapillary X-ray Lens." In: *Spectrochimica Acta Part B: Atomic Spectroscopy*. 10th Symposium on Total Reflection X-Ray Fluorescence Analysis and 39th Discussion Meeting on Chemical Analysis 59.8 (Aug. 31, 2004), pp. 1291–1294. ISSN: 0584-8547. DOI: 10.1016/j.sab.2004.05.016.

[23] P. S. Foundation. *Python*. Python. URL: https://www.python.org/ (visited on 01/03/2022).

[24] A. Galli, M. Martini, E. Sibilia, C. Montanari, and L. Panzeri. "Photoluminescence Emissions of Ceramics: A Marker of Production Technology." In: *Applied Physics A* 83.4 (June 2006), pp. 681–684. ISSN: 0947-8396, 1432-0630. DOI: 10.1007/s00339-006-3547-7.

[25] A. Galli, M. Martini, E. Sibilia, G. Padeletti, and P. Fermo. "Luminescence Properties of Lustre Decorated Majolica." In: *Applied Physics A* 79.2 (July 2004), pp. 293–297. ISSN: 0947-8396, 1432-0630. DOI: 10.1007/s00339-004-2517-1.

[26] B. Golosio, T. Schoonjans, A. Brunetti, P. Oliva, and G. L. Masala. "Monte Carlo Simulation of X-ray Imaging and Spectroscopy Experiments Using Quadric Geometry and Variance Reduction Techniques." In: *Computer Physics Communications* 185.3 (Mar. 2014), pp. 1044–1052. ISSN: 00104655. DOI: 10.1016/j.cpc.2013.10.034.

[27] D. Hélary, E. Darque-Ceretti, and M. Aucouturier. "Contemporary Golden-Like Lusters on Ceramics: Morphological, Chemical, and Structural Properties." In: *Journal of the American Ceramic Society* 88.11 (2005), pp. 3218–3221. ISSN: 1551-2916. DOI: 10.1111/j.1551-2916.2005.00549.x.

[28] J. G. Iñañez, M. Madrid-Fernández, J. Molera, R. J. Speakman, and T. Pradell. "Potters and Pigments: Preliminary Technological Assessment of Pigment Recipes of American Majolica by Synchrotron Radiation Micro-X-ray Diffraction (Sr-μXRD)." In:

Journal of Archaeological Science 40.2 (Feb. 1, 2013), pp. 1408–1415. ISSN: 0305-4403. DOI: 10.1016/j.jas.2012.09.015.

[29] K. Janssens, K. Proost, and G. Falkenberg. "Confocal Microscopic X-ray Fluorescence at the HASYLAB Microfocus Beamline: Characteristics and Possibilities." In: *Spectrochimica Acta Part B: Atomic Spectroscopy* 59.10-11 (Oct. 2004), pp. 1637–1645. ISSN: 05848547. DOI: 10.1016/j.sab.2004.07.025.

[30] B. Kanngießer, W. Malzer, I. Mantouvalou, D. Sokaras, and A. G. Karydas. "A Deep View in Cultural Heritage—Confocal Micro X-ray Spectroscopy for Depth Resolved Elemental Analysis." In: *Applied Physics A* 106.2 (Feb. 1, 2012), pp. 325–338. ISSN: 1432-0630. DOI: 10.1007/s00339-011-6698-0.

[31] M. Karimi, N. Amiri, and A. A. Tabbakh Shabani. "Thickness Measurement of Coated Ni on Brass Plate Using Kα/Kβ Ratio by XRF Spectrometry." In: *X-Ray Spectrometry* 38.3 (May 2009), pp. 234–238. ISSN: 00498246, 10974539. DOI: 10.1002/xrs.1146.

[32] A. G. Karydas et al. "An IAEA Multi-Technique X-ray Spectrometry Endstation at Elettra Sincrotrone Trieste: Benchmarking Results and Interdisciplinary Applications." In: *Journal of Synchrotron Radiation* 25.1 (Jan. 1, 2018), pp. 189–203. ISSN: 1600-5775. DOI: 10.1107/S1600577517016332.

[33] Y. Kayser et al. "Depth Profiling of Dopants Implanted in Si Using the Synchrotron Radiation Based High-Resolution Grazing Emission Technique." In: *X-Ray Spectrometry* 41.2 (2012), pp. 98–104. ISSN: 1097-4539. DOI: 10.1002/xrs.2372.

[34] R. Klockenkämper and A. von Bohlen. *Total-Reflection X-Ray Fluorescence Analysis and Related Methods*. 2nd ed. Vol. 181. Chemical Analysis. John Wiley & Sons, 2015. 555 pp. ISBN: 978-1-118-46027-6.

[35] I. Koshelev, A. P. Paulikas, M. Beno, G. Jennings, J. Linton, S. Uran, and B. W. Veal. "Characterization of the Scale on Oxidized Fe–Ni–Cr Alloys Using Grazing Emission X-ray Fluorescence." In: *Physica B: Condensed Matter* 304.1 (Sept. 1, 2001), pp. 256–266. ISSN: 0921-4526. DOI: 10.1016/S0921-4526(01)00557-9.

[36] K. Laclavetine, F. J. Ager, J. Arquillo, M. Respaldiza, and S. Scrivano. "Characterization of the New Mobile Confocal Micro X-ray Fluorescence (CXRF) System for in Situ Non-Destructive Cultural Heritage Analysis at the CNA: μXRF-CONCHA." In: *Microchemical Journal* 125 (Mar. 2016), pp. 62–68. ISSN: 0026265X. DOI: 10.1016/j.microc.2015.11.013.

[37] S. Manninen, T. Pitkänen, S. Koikkalainen, and T. Paakkari. "Study of the Ratio of Elastic to Inelastic Scattering of Photons." In: *The International Journal of Applied Radiation and Isotopes* 35.2

(Feb. 1984), pp. 93–98. ISSN: 0020708X. DOI: 10.1016/0020-708X(84)90190-X.

[38] A. Markowicz. "X-Ray Physics." In: *Handbook of X-ray Spectrometry*. Ed. by R. van Grieken and A. Markowicz. 2nd ed., rev. and expanded. Vol. 29. Practical Spectroscopy. New York: Marcel Dekker, 2002, p. 983. ISBN: 978-0-8247-0600-5.

[39] J. Miranda, J. Rickards, and R. Trejo-Luna. "PIXE Depth Profiling Using Variation of Detection Angle." In: *Nuclear Instruments and Methods in Physics Research Section B: Beam Interactions with Materials and Atoms*. Ion Beam Analysis 249.1 (Aug. 1, 2006), pp. 394–396. ISSN: 0168-583X. DOI: 10.1016/j.nimb.2006.04.062.

[40] J. Molera, C. Bayés, P. Roura, D. Crespo, and T. Pradell. "Key Parameters in the Production of Medieval Lustre Colours and Shines." In: *J. Am. Ceram Soc.* 90 (Jan. 1, 2007), pp. 2247–2257.

[41] K. Nakano and K. Tsuji. "Nondestructive Elemental Depth Profiling of Japanese Lacquerware 'Tamamushi-nuri' by Confocal 3D-XRF Analysis in Comparison with Micro GE-XRF." In: *X-Ray Spectrometry* 38.5 (Sept. 2009), pp. 446–450. ISSN: 00498246, 10974539. DOI: 10.1002/xrs.1163.

[42] M. Newville et al. *Lmfit/Lmfit-Py 1.0.2*. Zenodo, Feb. 7, 2021. DOI: 10.5281/zenodo.4516651.

[43] A. Okhrimovskyy and K. Tsuji. "Numerical Approach for Depth Profiling with GE-XRF." In: *X-Ray Spectrometry* 35.5 (2006), pp. 305–311. ISSN: 1097-4539. DOI: 10.1002/xrs.912.

[44] G. Padeletti and P. Fermo. "How the Masters in Umbria, Italy, Generated and Used Nanoparticles in Art Fabrication during the Renaissance Period." In: *Applied Physics A: Materials Science & Processing* 76.4 (Mar. 1, 2003), pp. 515–525. ISSN: 0947-8396, 1432-0630. DOI: 10.1007/s00339-002-1935-1.

[45] G. Padeletti and P. Fermo. "Italian Renaissance and Hispano - Moresque Lustre-Decorated Majolicas: Imitation Cases of Hispano - Moresque Style in Central Italy." In: *Applied Physics A: Materials Science & Processing* 77.1 (June 1, 2003), pp. 125–133. ISSN: 0947-8396, 1432-0630. DOI: 10.1007/s00339-002-2048-6.

[46] G. Padeletti, P. Fermo, S. Gilardoni, and A. Galli. "Technological Study of Ancient Ceramics Produced in Casteldurante (Central Italy) during the Renaissance." In: *Applied Physics A* 79.2 (July 2004), pp. 335–339. ISSN: 0947-8396, 1432-0630. DOI: 10.1007/s00339-004-2521-5.

[47] G. Padeletti, G. Ingo, A. Bouquillon, S. Pages, M. Aucouturier, S. Röhrs, and P. Fermo. "First-Time Observation of Mastro Giorgio Masterpieces by Means of Non-Destructive Techniques." In: *Applied Physics A* 83 (June 1, 2006), pp. 475–483. DOI: 10.1007/s00339-006-3549-5.

[48] R. Padilla, O. Schalm, K. Janssens, R. Arrazcaeta, and P. Van Espen. "Microanalytical Characterization of Surface Decoration in Majolica Pottery." In: *Analytica Chimica Acta* 535.1 (Apr. 11, 2005), pp. 201–211. ISSN: 0003-2670. DOI: 10.1016/j.aca.2004.11.082.

[49] R. Padilla, P. Van Espen, A. Abrahantes, and K. Janssens. "Semi-empirical Approach for Standardless Calibration in μ-XRF Spectrometry Using Capillary Lenses: Standardless Calibration in μ-XRF Using Capillary Lenses." In: *X-Ray Spectrometry* 34.1 (Jan. 2005), pp. 19–27. ISSN: 00498246. DOI: 10.1002/xrs.781.

[50] S. Padovani, C. Sada, P. Mazzoldi, B. Brunetti, I. Borgia, A. Sgamellotti, A. Giulivi, F. D'Acapito, and G. Battaglin. "Copper in Glazes of Renaissance Luster Pottery: Nanoparticles, Ions, and Local Environment." In: *Journal of Applied Physics* 93.12 (June 15, 2003), pp. 10058–10063. ISSN: 0021-8979. DOI: 10.1063/1.1571965.

[51] L. G. Parratt. "Surface Studies of Solids by Total Reflection of X-Rays." In: *Physical Review* 95.2 (July 15, 1954), pp. 359–369. ISSN: 0031-899X. DOI: 10.1103/PhysRev.95.359.

[52] R. D. Perez, H. J. Sánchez, C. A. Perez, and M. Rubio. "Latest Developments and Opportunities for 3D Analysis of Biological Samples by Confocal μ-XRF." In: *Radiation Physics and Chemistry*. Special Issue on Future Directions in Atomic and Condensed Matter Research and Applications 79.2 (Feb. 1, 2010), pp. 195–200. ISSN: 0969-806X. DOI: 10.1016/j.radphyschem.2009.04.034.

[53] S. Pessanha, M. Manso, V. Antunes, M. Carvalho, and J. Sampaio. "Monte Carlo Simulation of Portable X-ray Fluorescence Setup: Non-invasive Determination of Gold Leaf Thickness in Indo-Portuguese Panel Paintings." In: *Spectrochimica Acta Part B: Atomic Spectroscopy* 156 (June 2019), pp. 1–6. ISSN: 05848547. DOI: 10.1016/j.sab.2019.04.006.

[54] P. Poths, E. Chinea-Cano, N. Dzigal, I. G. Darby, J. Osan, and R. Padilla-Alvarez. "Experimental Assessment of Effectively Probed Volume in Confocal XRF Spectrometry Using Microparticles." In: *X-Ray Spectrometry* 48.5 (2019), pp. 553–560. ISSN: 1097-4539. DOI: 10.1002/xrs.3045.

[55] R. J. Potton. "Reciprocity in Optics." In: *Reports on Progress in Physics* 67.5 (Apr. 2004), pp. 717–754. ISSN: 0034-4885. DOI: 10.1088/0034-4885/67/5/R03.

[56] T. Pradell, A. Climent-Font, J. Molera, A. Zucchiatti, M. D. Ynsa, P. Roura, and D. Crespo. "Metallic and Nonmetallic Shine in Luster: An Elastic Ion Backscattering Study." In: *Journal of Applied Physics* 101.10 (May 15, 2007), p. 103518. ISSN: 0021-8979. DOI: 10.1063/1.2734944.

[57] T. Pradell, J. Molera, A. D. Smith, and M. S. Tite. "Early Islamic Lustre from Egypt, Syria and Iran (10th to 13th Century AD)." In: *Journal of Archaeological Science* 35.9 (Sept. 1, 2008), pp. 2649–2662. ISSN: 0305-4403. DOI: 10.1016/j.jas.2008.05.011.

[58] T. Pradell. "Lustre and Nanostructures—Ancient Technologies Revisited." In: *Nanoscience and Cultural Heritage*. Ed. by P. Dillmann, L. Bellot-Gurlet, and I. Nenner. Paris: Atlantis Press, 2016, pp. 3–39. ISBN: 978-94-6239-198-7. DOI: 10.2991/978-94-6239-198-7_1.

[59] G. Roisine, N. Capobianco, D. Caurant, G. Wallez, A. Bouquillon, O. Majérus, L. Cormier, S. Gilette, and A. Gerbier. "The Art of Bernard Palissy (1510 – 1590): Influence of Firing Conditions on the Microstructure of Iron-Coloured High-Lead Glazes." In: *Applied Physics A* 123.8 (July 5, 2017), p. 501. ISSN: 1432-0630. DOI: 10.1007/s00339-017-1089-9.

[60] R. S. Santos, D. F. Oliveira, J. T. Assis, and M. J. Anjos. "Development of a Portable System of Grazing Exit X-Rray Fluorescence Applied to Environmental and Biological Studies." In: (2017), p. 10.

[61] P. Sciau. "Nanoparticles in Ancient Materials: The Metallic Lustre Decorations of Medieval Ceramics." In: *The Delivery of Nanoparticles*. Ed. by A. A. Hashim. Intechopen, May 16, 2012, pp. 525–540. ISBN: 978-953-51-0615-9. DOI: 10.5772/34080.

[62] J. Sherman. "The Theoretical Derivation of Fluorescent X-ray Intensities from Mixtures." In: *Spectrochimica Acta* 7 (Jan. 1, 1955), pp. 283–306. ISSN: 0371-1951. DOI: 10.1016/0371-1951(55)80041-0.

[63] V. A. Solé, E. Papillon, M. Cotte, P. Walter, and J. Susini. "A Multiplatform Code for the Analysis of Energy-Dispersive X-ray Fluorescence Spectra." In: *Spectrochim. Acta B* 62.1 (2007), pp. 63–68. DOI: 10.1016/j.sab.2006.12.002.

[64] Z. Spolnik, K. Tsuji, and R. Van Grieken. "Grazing-Exit Electron Probe x-Ray Microanalysis of Light Elements in Particles." In: *X-Ray Spectrometry* 33.1 (2004), pp. 16–20. ISSN: 1097-4539. DOI: 10.1002/xrs.656.

[65] V. Szwedowski-Rammert, J. Baumann, C. Schlesiger, U. Waldschläger, A. Gross, B. Kanngießer, and I. Mantouvalou. "Laboratory Based GIXRF and GEXRF Spectrometers for Multilayer Structure Investigations." In: *Journal of Analytical Atomic Spectrometry* 34.5 (2019), pp. 922–929. ISSN: 0267-9477, 1364-5544. DOI: 10.1039/C8JA00427G.

[66] V. Szwedowski, J. Baumann, I. Mantouvalou, L. Bauer, W. Malzer, and B. Kanngießer. "Scan-Free Grazing Emission XRF Measurements in the Laboratory Using a CCD." In: *physica status solidi c* 14.12 (2017), p. 1700158. ISSN: 1610-1642. DOI: 10.1002/pssc.201700158.

[67] R. Tertian and F. Claisse. *Principles of Quantitative X-ray Fluorescence Analysis*. Heyden, 1982. 412 pp. ISBN: 978-0-85501-709-5. Google Books: 5OrvAAAAMAAJ.

[68] T. Trojek. "Iterative Monte Carlo Procedure for Quantitative X-ray Fluorescence Analysis of Copper Alloys with a Covering Layer." In: *Radiation Physics and Chemistry* 167 (Feb. 2020), p. 108294. ISSN: 0969806X. DOI: 10.1016/j.radphyschem.2019.04.044.

[69] T. Trojek and D. Wegrzynek. "X-Ray Fluorescence Kα/Kβ Ratios for a Layered Specimen: Comparison of Measurements and Monte Carlo Calculations with the MCNPX Code." In: *Nuclear Instruments and Methods in Physics Research Section A: Accelerators, Spectrometers, Detectors and Associated Equipment* 619.1-3 (July 2010), pp. 311–315. ISSN: 01689002. DOI: 10.1016/j.nima.2009.10.157.

[70] T. Trojek, L. Musílek, and R. Prokeš. "Depth of Layers in Historical Materials Measurable by X-ray Fluorescence Analysis." In: *Radiation Physics and Chemistry* 155 (Feb. 2019), pp. 239–243. ISSN: 0969806X. DOI: 10.1016/j.radphyschem.2018.06.047.

[71] T. Trojek, R. Prokeš, R. Šefců, H. Bilavčíková, and T. Čechák. "Confocal X-ray Fluorescence Spectrometer for in-Situ Analyses of Paintings." In: *Radiation Physics and Chemistry* 137 (Aug. 2017), pp. 238–242. ISSN: 0969806X. DOI: 10.1016/j.radphyschem.2016.02.031.

[72] T. Trojek, T. Čechák, and L. Musílek. "Recognition of Pigment Layers in Illuminated Manuscripts by Means of Kα/Kβ and Lα/Lβ Ratios of Characteristic X-rays." In: *Applied Radiation and Isotopes* 68.4-5 (Apr. 2010), pp. 871–874. ISSN: 09698043. DOI: 10.1016/j.apradiso.2009.09.054.

[73] K. Tsuji. "Grazing-Exit Electron Probe X-ray Microanalysis (GE-EPMA): Fundamental and Applications." In: *Spectrochimica Acta Part B: Atomic Spectroscopy* 60.11 (Nov. 1, 2005), pp. 1381–1391. ISSN: 0584-8547. DOI: 10.1016/j.sab.2005.08.013.

[74] K. Tsuji, Z. Spolnik, K. Wagatsuma, R. E. Van Grieken, and R. D. Vis. "Grazing-Exit Particle-Induced X-ray Emission Analysis with Extremely Low Background." In: *Analytical Chemistry* 71.22 (Nov. 1, 1999), pp. 5033–5036. ISSN: 0003-2700. DOI: 10.1021/ac990568u.

[75] K. Uhlir et al. "The Mystery of Mercury-Layers on Ancient Coins — A Multianalytical Study on the Sasanian Coins under the Reign of Khusro II." In: *Microchemical Journal* 125 (Mar. 1, 2016), pp. 159–169. ISSN: 0026-265X. DOI: 10.1016/j.microc.2015.10.024.

[76] H. P. Urbach and P. K. de Bokx. "Calculation of Intensities in Grazing-Emission x-Ray Fluorescence." In: *Physical Review B* 53.7 (Feb. 15, 1996), pp. 3752–3763. ISSN: 0163-1829, 1095-3795. DOI: 10.1103/PhysRevB.53.3752.

[77] H. P. Urbach and P. K. de Bokx. "Grazing Emission X-Ray Fluorescence from Multilayers." In: *Physical Review B* 63.8 (Feb. 2, 2001), p. 085408. DOI: 10.1103/PhysRevB.63.085408.

[78] L. Vincze, B. Vekemans, F. E. Brenker, G. Falkenberg, K. Rickers, A. Somogyi, M. Kersten, and F. Adams. "Three-Dimensional Trace Element Analysis by Confocal X-ray Microfluorescence Imaging." In: *Analytical Chemistry* 76.22 (Nov. 1, 2004), pp. 6786–6791. ISSN: 0003-2700. DOI: 10.1021/ac049274l.

[79] S. Waksman, C. Capelli, T. Pradell, and J. Molera. "Chapter 12. The Ways of the Lustre: Looking for the Tunisian Connection." In: *Craft and Science: International Perspectives on Archaeological Ceramics*. Ed. by Martinón-Torres. UCL Qatar Series in Archaeology and Cultural Heritage. Hamad bin Khalifa University Press (HBKU Press), Nov. 1, 2014, pp. 109–116. ISBN: 978-9927-101-75-5. DOI: 10.5339/uclq.2014.cas.ch12.

[80] D. Wegrzynek, R. Mroczka, A. Markowicz, E. Chinea-Cano, and S. Bamford. "Experimental Evaluation of X-ray Optics Applied for Microanalysis." In: *X-Ray Spectrometry* 37.6 (2008), pp. 635–641. ISSN: 1097-4539. DOI: 10.1002/xrs.1113.

[81] D. Wegrzynek, A. Markowicz, S. Bamford, E. Chinea-Cano, and M. Bogovac. "Micro-Beam X-ray Fluorescence and Absorption Imaging Techniques at the IAEA Laboratories." In: *Nuclear Instruments and Methods in Physics Research Section B: Beam Interactions with Materials and Atoms*. Nuclear Microprobe Technology and Applications 231.1 (Apr. 1, 2005), pp. 176–182. ISSN: 0168-583X. DOI: 10.1016/j.nimb.2005.01.053.

[82] J. R. Wolberg. *Data Analysis Using the Method of Least Squares: Extracting the Most Information from Experiments*. Berlin ; New York: Springer, 2006. 250 pp. ISBN: 978-3-540-25674-8.

[83] Šmit, K. Janssens, K. Proost, and I. Langus. "Confocal μ-XRF Depth Analysis of Paint Layers." In: *Nuclear Instruments and Methods in Physics Research Section B: Beam Interactions with Materials and Atoms*. Proceedings of the Sixteenth International Conference on Ion Beam Analysis 219–220 (June 1, 2004), pp. 35–40. ISSN: 0168-583X. DOI: 10.1016/j.nimb.2004.01.024.